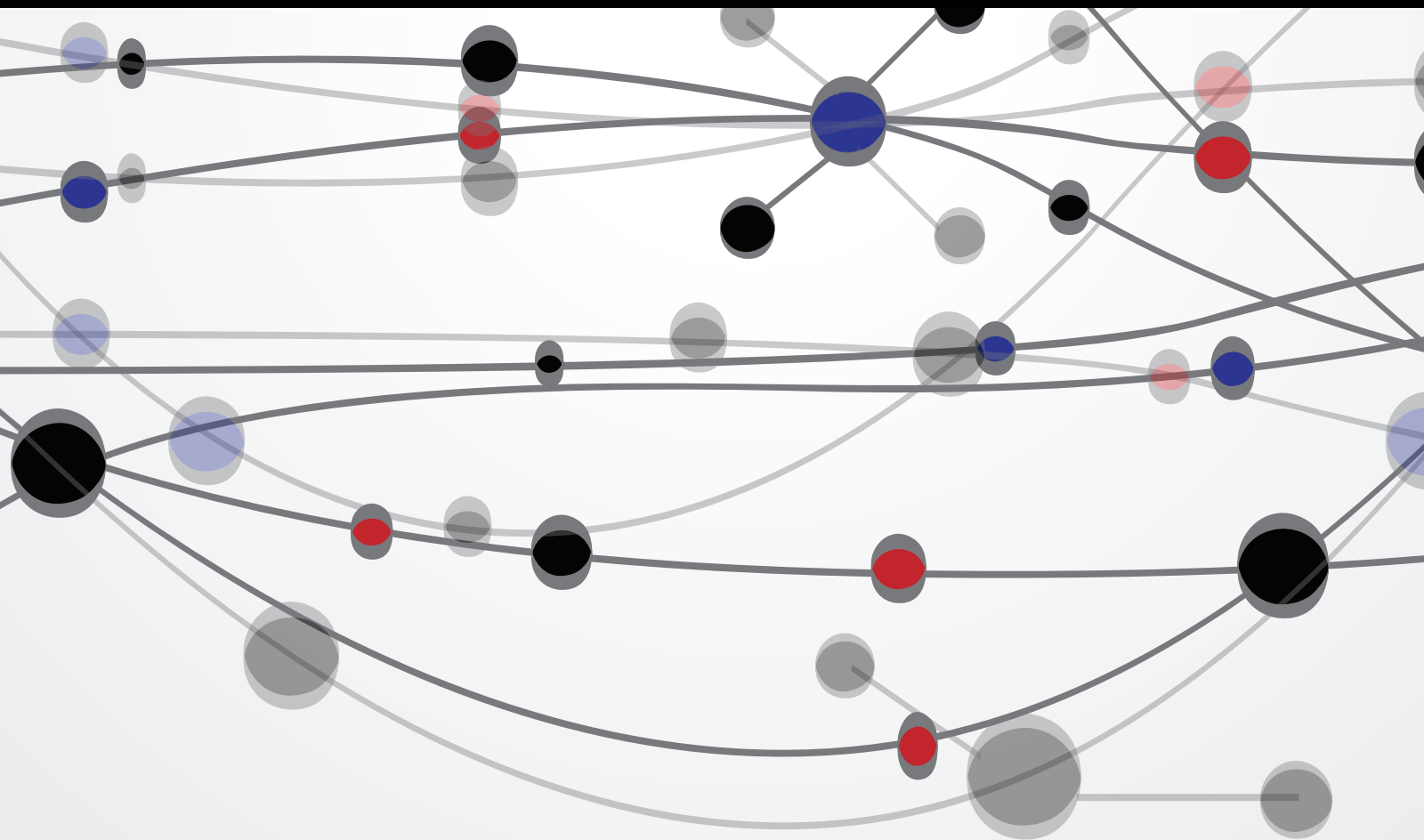


# Computational Heat and Mass Transfer and Fluid Flow through Complex Passages for Emerging Applications

Guest Editors: Mohammad Reza Safaei, Arash Karimipour, Kamel Hooman, Marjan Goodarzi, Goodarz Ahmadi, and Ali Tamayol





---

**Computational Heat and Mass Transfer and Fluid  
Flow through Complex Passages for Emerging  
Applications**

**Computational Heat and Mass Transfer and Fluid Flow through Complex Passages for Emerging Applications**

Guest Editors: Mohammad Reza Safaei, Arash Karimipour, Kamel Hooman, Marjan Goodarzi, Goodarz Ahmadi, and Ali Tamayol



---

Copyright © 2015 Hindawi Publishing Corporation. All rights reserved.

This is a special issue published in "The Scientific World Journal." All articles are open access articles distributed under the Creative Commons Attribution License, which permits unrestricted use, distribution, and reproduction in any medium, provided the original work is properly cited.

## Contents

---

**Indoor Solar Thermal Energy Saving Time with Phase Change Material in a Horizontal Shell and Finned-Tube Heat Exchanger**, S. Paria, A. A. D. Sarhan, M. S. Goodarzi, S. Baradaran, B. Rahmanian, H. Yarmand, M. A. Alavi, S. N. Kazi, and H. S. C. Metselaar  
Volume 2015, Article ID 291657, 7 pages

**CFD Convective Flow Simulation of the Varying Properties of CO<sub>2</sub>-H<sub>2</sub>O Mixtures in Geothermal Systems**, S. Yousefi, A. D. Atrens, E. Sauret, M. Dahari, and K. Hooman  
Volume 2015, Article ID 843068, 8 pages

**Working Characteristics of Variable Intake Valve in Compressed Air Engine**, Qihui Yu, Yan Shi, and Maolin Cai  
Volume 2014, Article ID 498934, 9 pages

**Investigation of Micro- and Nanosized Particle Erosion in a 90° Pipe Bend Using a Two-Phase Discrete Phase Model**, M. R. Safaei, O. Mahian, F. Garoosi, K. Hooman, A. Karimipour, S. N. Kazi, and S. Gharehkhani  
Volume 2014, Article ID 740578, 12 pages

**Modeling Validation and Control Analysis for Controlled Temperature and Humidity of Air Conditioning System**, Jing-Nang Lee, Tsung-Min Lin, and Chien-Chih Chen  
Volume 2014, Article ID 903032, 10 pages

## Research Article

# Indoor Solar Thermal Energy Saving Time with Phase Change Material in a Horizontal Shell and Finned-Tube Heat Exchanger

**S. Paria,<sup>1</sup> A. A. D. Sarhan,<sup>1,2</sup> M. S. Goodarzi,<sup>3</sup> S. Baradaran,<sup>1</sup> B. Rahmanian,<sup>4</sup>  
H. Yarmand,<sup>1</sup> M. A. Alavi,<sup>3</sup> S. N. Kazi,<sup>1</sup> and H. S. C. Metselaar<sup>1</sup>**

<sup>1</sup>Department of Mechanical Engineering, Faculty of Engineering, University of Malaya, 50603 Kuala Lumpur, Malaysia

<sup>2</sup>Department of Mechanical Engineering, Faculty of Engineering, Assiut University, Assiut 71516, Egypt

<sup>3</sup>Department of Mechanical Engineering, Mashhad Branch, Islamic Azad University, Mashhad, Iran

<sup>4</sup>Department of Mechanical Engineering, Jahrom Branch, Payame Noor University, Jahrom, Iran

Correspondence should be addressed to S. Paria; saman.paria@gmail.com and A. A. D. Sarhan; ah\_sarhan@um.edu.my

Received 2 September 2014; Revised 28 December 2014; Accepted 12 January 2015

Academic Editor: Kamel Hooman

Copyright © 2015 S. Paria et al. This is an open access article distributed under the Creative Commons Attribution License, which permits unrestricted use, distribution, and reproduction in any medium, provided the original work is properly cited.

An experimental as well as numerical investigation was conducted on the melting/solidification processes of a stationary phase change material (PCM) in a shell around a finned-tube heat exchanger system. The PCM was stored in the horizontal annular space between a shell and finned-tube where distilled water was employed as the heat transfer fluid (HTF). The focus of this study was on the behavior of PCM for storage (charging or melting) and removal (discharging or solidification), as well as the effect of flow rate on the charged and discharged solar thermal energy. The impact of the Reynolds number was determined and the results were compared with each other to reveal the changes in amount of stored thermal energy with the variation of heat transfer fluid flow rates. The results showed that, by increasing the Reynolds number from 1000 to 2000, the total melting time decreases by 58%. The process of solidification also will speed up with increasing Reynolds number in the discharging process. The results also indicated that the fluctuation of gradient temperature decreased and became smooth with increasing Reynolds number. As a result, by increasing the Reynolds number in the charging process, the theoretical efficiency rises.

## 1. Introduction

The general interest in renewable energy source applications, particularly solar energy, has increased as a result of paying closer attention and extended research on environmental considerations along with effective and rational energy management. Due to disparities between solar heating energy supply and demand, employing devices to store thermal energy is necessary. Thermal energy storage plays a significant role in practical and rational energy usage, since the dominance of energy demand over production is globally recognized. Suitable thermal storage is particularly necessary in cases where intermittent energy is generated, such as waste heat recovery and solar thermal systems. Energy storage can be defined as the storage of a form of energy which can later be utilized in other advantageous operations. Thermal energy storage can refer to technologies through which energy is stored in a thermal reservoir for later purposeful utilization.

It is also possible to maintain the thermal reservoir at a lower (colder) or higher (hotter) temperature than that of the ambient environment.

There are three main ways of storing thermal energy, namely, sensible, latent, and thermochemical heat storage. However, the mismatched energy availability and demand for solar domestic hot water (SDHW) systems as well as limited availability of solar energy at night are problems that need to be addressed [1]. Thermal energy storage (TES) is commonly used in bridging the gap between energy demand and availability. Hot water storage tank systems are required to store sensible energy; however, they need significant space and add weight to structural components. Such requirements inhibit further SDHW deployment in buildings with limited space or structural limitations. Nevertheless, using phase change materials (PCMs) for TES can solve this problem by reducing the weight and space required for energy storage [2]. Thermal storage technology based on using PCM has

attracted increasing attention in recent years. This is mostly attributed to the high density of energy storage occurring in the process of phase change within a very narrow temperature range. They can be used in balancing the night and day-time energy demand. PCMs function as energy storage mediums, whereby energy is stored during the melting process and is released during solidification. PCMs have the advantage of having isothermal operating attributes, such as heat charging and discharging at an almost constant temperature along with high energy storage density during melting and solidification. These benefits make PCMs an appropriate choice for effective thermal system operation [3].

Recently, several works have been carried out to study the thermal characteristics of paraffin during the melting and solidification processes [4–10]. Paraffin wax PCMs were found to have good thermal stability after repeated cycles using a DSC, showing little to no degradation of the latent heat and phase transition temperature ranges [11, 12]. Dodecanoic acid (also called lauric acid) has been shown to have a melting temperature range that is suitable for LHESS used for SDHW energy storage (40 to 50°C for a SDHW system) [13]. It also has stable thermal properties, is safe for use with domestic water, and is readily available and relatively inexpensive [14]. Two methods of using PCM to store thermal energy can be found in the literature. One of the methods involves using PCM as a wax in the shell and tube heat exchanger. In this type of heat storage unit, the PCM is placed in the shell and the HTF flows through the tubes. A number of researches have been conducted on this configuration by Zhang and Faghri [15], Lacroix [16], Cao and Faghri [17], Ismail and Lino [18], Akgün et al. [19], Liu et al. [20, 21], and Bellecci and Conti [22]. The rigid capsule is the second configuration. In this method, PCM is placed in the capsule and HTF flows through a tube surrounding the capsule.

The shell and tube heat exchanger is considered the most promising configuration as a latent heat storage system, because it provides a great digress of effectiveness for a minimum volume [23]. Ismail and Alves [24] made a theoretical model of the shell and tube-type heat exchanger for energy storage. A similar problem was modeled by Cao et al. [25]. In their models, the process of recovery and charging is carried out by the heat charging and recovery processes. The shell wall of the storage unit was considered adiabatic for both of these models. Bellecci and Conti [22] also investigated a model of energy storage in a shell and tube-type heat exchanger and used the enthalpy model to solve the problem. The latent heat energy storage systems were separately examined for counter and annular flows. It was recognized that the counter flow storage system is more effective in absorbing thermal energy [23, 26]. Compared to the vertical tube-in-shell storage geometries, few surveys have been conducted on the horizontal ones. Increasing heat transfer by using finned surfaces is one of the techniques used for increasing the amount of energy storage. A great number of investigations, both experimental and theoretical, have been performed to explore the impact of rectangular cross-sectioned fins on the melting and solidification rate. For example, Bathelt and Viskanta [27] conducted a study of the solidification on tubes with horizontal fins placed at

TABLE 1: Thermophysical properties of the PCM and finned-tube.

Properties	Tube material	Phase change material	
		Solid	Liquid
$\rho$ (kg/m <sup>3</sup> )	8800	0.790	0.916
$C_p$ (j/kg·K)	420	n.a	n.a
$K$ (W/m·K)	52	0.167	0.346
$\alpha$ (m <sup>2</sup> /s)	$1.4 \times 10^{-5}$	n.a	
$L$ (kj/kg)	n.a	160	
$T$ (°C)	n.a	53	57

four various fin spacing distances. Cabeza et al. [28] also conducted different studies on the effect of various types of finned-tubes on frozen layers.

The presented literature survey suggests that compared to the vertical tube-in-shell storage geometries, a few investigations have been conducted on the horizontal ones. In particular, the heat transfer enhancement of PCMs in shell and finned-tube heat exchanger is still not entirely understood. The objective of the present research was to experimentally examine paraffin's melting and solidification attributes in a horizontal finned shell and tube storage geometry to increase solar thermal energy saving time. The storage geometry is on annular space (in which PCM is loaded) between a shell (a finned shell and tube-type of heat exchanger system) and a tube through which HTF (water) flows. In order to investigate the impact of the HTF inlet flow on the amount of charge, several experiments were carried out. In line with the focus of this survey, close attention was particularly paid to understanding the physics of the melting and solidification attributes based on the time records and histories of temperature patterns within the PMC; this served as a foundation for enhanced design and performance.

## 2. Experimental Details

**2.1. Heat Storage Material.** Paraffin ASTM D 87, which is provided from the Sigma-Aldrich, was employed as PCM in this study. Paraffin is widely recognized as a nontoxic, chemically stable, and attractive material which is degradable and possesses a notable capacity of storing latent heat within a narrow temperature range. Table 1 presents a list of thermophysical properties which are employed in this research.

**2.2. Experimental Apparatus and Procedure.** The experimental installation shown in Figure 1 is composed of heating/cooling circuit. The setup consists of a data acquisition unit (Computer and Data logger), connecting pipes, a horizontal test module (PMC storage container), a flow-adjustment valve, an outlet valve, and a constant temperature bath. The constant temperature bath (Wise Circu WCR-P6), which controls the heat transfer fluid's (HTF's) inlet temperature which delivers as much as 15 L/min of water, has an accuracy of  $\pm 0.1^\circ\text{C}$ , and its temperature range is  $-20$  to  $+100^\circ\text{C}$ . The HTF utilized was distilled water. The constant-temperature bath of the circuit is a hot water in a finned-tube

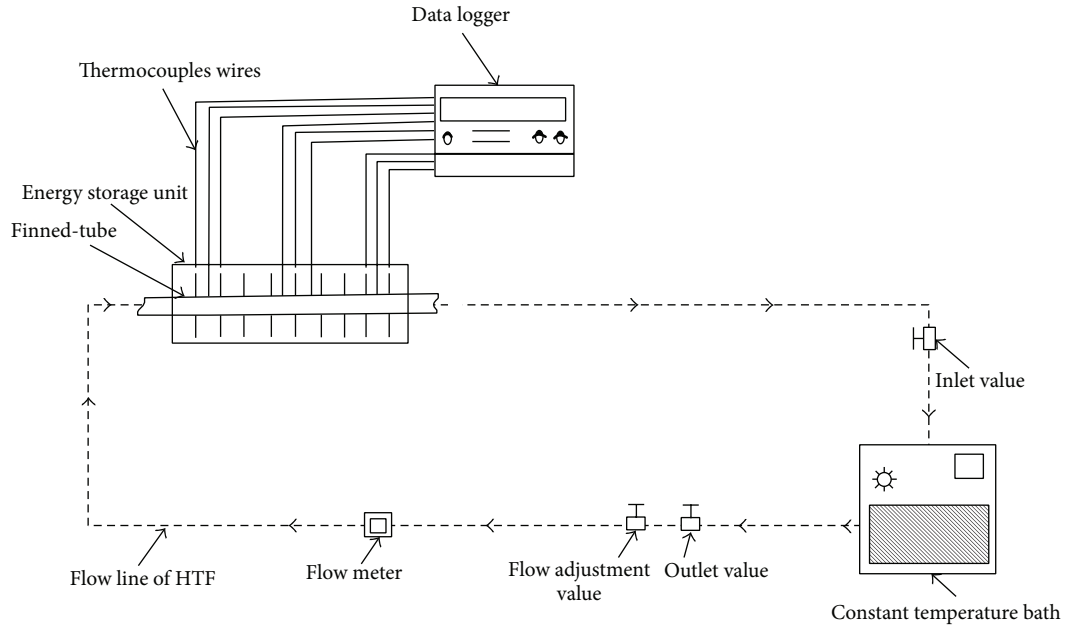


FIGURE 1: Schematic view of the experimental setup.

where the water is heated to the desired working temperature controlled thermally within  $\pm 1^\circ\text{C}$ . This thermal bath served as a heat source replacing solar heat in real application.

In charging process, the heat water withdrawn by the constant-temperature bath passes through the flow meter in the form of a calibrated orifice plate and then flows through the test finned-tube fixed horizontally in the acrylic shell full with PCM (paraffin). This process was deemed to have finished once all temperature recordings of the test module (PCM container) showed higher values than PCM's melting temperature and the entire paraffin melted. This cycle was repeated subsequent to the charging process, and the energy stored was extracted through the discharging process (the circulation of cold water). At solidification process fluid at a much lower temperature than the liquid PCM which passes in the finned-tube heat is withdrawn from the liquid PCM and a layer of solidified PCM is formed over the tube and fins surfaces. The water then flows back to constant-temperature bath where it is further cooled and repumped to the test section. The solidification process stopped when the whole amount of PCM was solidified and the test module temperature was less than PCM's solidification temperature. The test module is composed of a copper tube with 15 mm inner and 20 mm outer diameters, which is surrounded by a shell tube with 60 mm inner and 64 mm outer diameters that provides an annular gap around the tube (tube-in-shell). The shell is made of acrylic with thermal conductivity ( $k = 0.1 \text{ W/m K}$ ). The PCM heads to fill up the test module of the 0.8 kg shell.

The temperature measurement system consists of thermocouples and a data logger. It is essential to measure the temperatures of the finned-tube wall, the fin tip, and base tube to accurately determine the heat transfer to the phase-change material. In this study, *K*-type thermocouples were

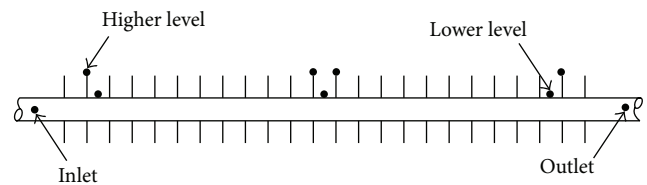


FIGURE 2: Installation of the thermocouples on the finned-tube.

used, whose locations are depicted in Figure 2. During this experiment, the temperatures at 20 different points in the energy storage unit were measured and recorded. To enhance experiment accuracy and collect additional temperature data, many more thermocouples were applied among the fins. The thermocouples were located on three parts of the device. Sixteen thermocouples were used on the finned-tube. Two thermocouples were installed at entry and exit of the finned-tube to measure the temperature of the working fluid and another two thermocouples were utilized to measure the ambient temperatures and PCM container. The output data was recorded by the help of a HP type 34970A data logger with  $\pm 1^\circ\text{C}$  accuracy; this data logger measured the thermocouples' millivolt outputs. The signal output from the data logger was transferred and documented in a personal computer.

For this process, HP-Benchlink software was used. The temperature values were scanned by the data logger every 10 seconds during both melting and solidification. All thermocouples were installed on the finned-tube by brazing. The HTF's volumetric flow rate was controlled by controlling the adjustment valve gate that was situated at the inlet of the loop. All experiments were conducted in a conditional room with ambient temperature of  $30^\circ\text{C}$ . The experiments

were carried at no less than three times, and three different Reynolds number values of heat transfer fluid with similar outcomes were considered, namely, 1000, 1500, and 2000. The entire recorded transient temperatures were repeated in a range of  $\pm 3\%$ . In an attempt to put a stop to loss into the vicinity, the system was covered with fiberglass insulation that was 37 mm thick and had an aluminized outer surface cladding. The average thermal conductivity of this cover layer was 0.038 W/m K. It is important to remember that studies on charging and discharging were both conducted at a constant inlet temperature. The discharging studies were carried out after the charging studies were conducted and were performed at  $T_i = 63$  and  $47^\circ\text{C}$ . In section three, the studies on charging and discharging outcomes are separately presented. All instruments used in the test were calibrated prior to measurements. The measurements and photographs were taken in the region of the all fins where a precision scale is attached.

### 3. Numerical Procedure

The FLUENT commercial code based on finite volume method, which has been used in some previous works [29–31], was applied to solve the Reynolds Averaged Navier-Stokes (RANS) equations. This method is based on a particular type of the residual weighting approach. In this approach, the computational zone is divided into finite control volumes as each node is covered by a control volume. Eventually, the differential equation is integrated on each finite volume [32, 33]. The second-order upwind method [34, 35] was chosen for the discretization of all terms, while the SIMPLE algorithm [36, 37] was employed for pressure-velocity coupling. The solution was converged when the residuals for all the equations dropped below  $10^{-6}$  [38, 39].

### 4. Results and Discussion

**4.1. Charging Process.** Figure 3 shows the temperature gradient of PCM at different times and Reynolds numbers,  $Re = 1000, 1500,$  and  $2000$ . It can be seen that PCM takes a short time to reach the melting temperature with a higher Reynolds number. According to results, the gradient temperature fluctuations began from 470, 276, and 270 seconds for  $Re = 1000, Re = 1500,$  and  $Re = 2000$ , respectively. It is clear that the fluctuation of gradient temperature decreased and became smooth with increasing Reynolds number. As a result, by increasing the Reynolds number in the charging process, the theoretical efficiency rises. As theoretical efficiency approaches unity (e.g., in the melting process), from the definition of efficiency, it can be concluded that the energy required to melt the whole PCM is provided [40].

For a clearer explanation, Figures 4(a)–4(c) depict the results of  $Re = 1000$  as an example of normal behavior of a transition. As witnessed, melting begins peripherally, near the HTF tube’s wall and it continues to spread radially outwards. When the charging process is initiated, the PCMs close to the HTF tube’s wall surface reach the melting point, which is due to the conduction of the finned-tube. The rapid melting of the

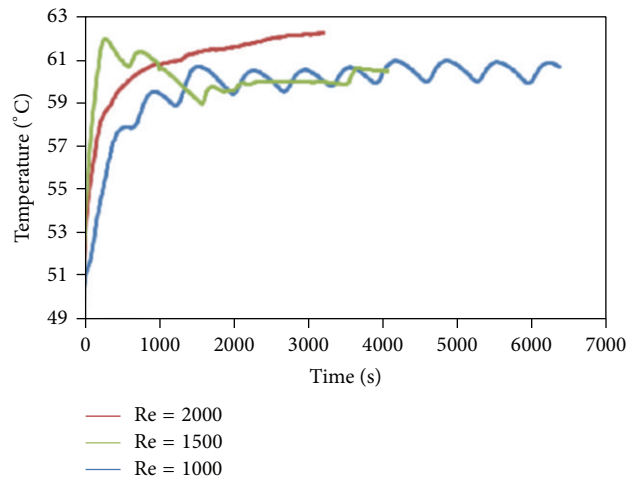


FIGURE 3: Temperature measurement records in the melting process for  $Re = 1000, Re = 1500,$  and  $Re = 2000$ .

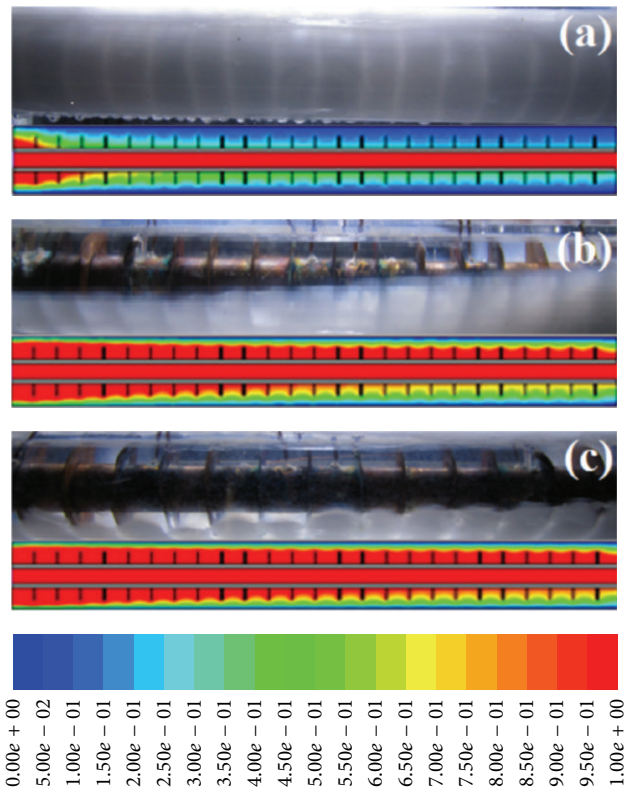


FIGURE 4: Melting process for  $Re = 1000$  at (a) 1000 s, (b) 3500 s, and (c) 6000 s.

PCMs near the walls is mostly because of greater temperature differences of PCM in the surrounding areas of the tube wall. Nevertheless, it is worth noting that the melting behavior of PCMs in the upper areas differs from those in lower regions. The molten PCM moves up towards the storage container’s top areas due to the natural convection. The melting region extends radially upward. As a result, the areas in the upper

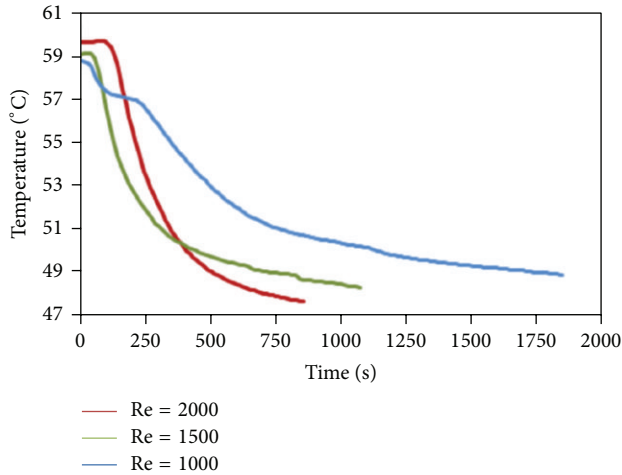


FIGURE 5: Temperature measurement records in the solidification process for Re = 1000, Re = 1500, and Re = 2000.

sections attain melting temperature more rapidly than the lower parts.

The natural convection has a greater effect in the upper regions of the annular storage container. Aydin et al. [41] offered a good, comprehensive description of the physical attributes displayed by PCM in the charging process whereby two areas coexist. These two areas are the solid phase non-melted PCM and liquid phase melted PCM. Due to buoyancy forces produced by the density gradients that resulted from differences in temperature, the melted PCM recirculation is spurred by the heat transfer through convection when the PCM's solid matrix melts. The heating and mixing of the molten PCM are elevated by recirculation inside the test section and the fact is that it takes less time for the areas closer to the upper regions to reach melting temperature than lower regions. However, it is worth noting that PCM has a lower density in the molten phase compared to the solid phase. In cases with larger operation, the PCM molten area spreads to cover larger areas of the PCM container. In line with the assumptions, the melting will increase with rising Reynolds number.

**4.2. Discharging Process.** Experimentations on the discharging process were carried out by reversing the heat transfer direction between HTF and PCM. Hereby, the cold water was circulated through the system. The temperature measurement records for different thermocouples at varying times are presented in Figure 5. The initial temperature of PCM, in the liquid phase, is 63°C. It is then introduced to a sudden temperature change in the circulating system during the discharging process as a result of the high temperature differences between HTF and PCM. Due to the transfer of sensible heat taking place within the solid PCM, volume increases until complete solidification occurs at solidification temperature. In accordance with the expectations, the points closer to the inlet part and HTF wall solidified faster than the other areas. In an attempt to provide a more comprehensive perception of the physics of the process, Figure 5

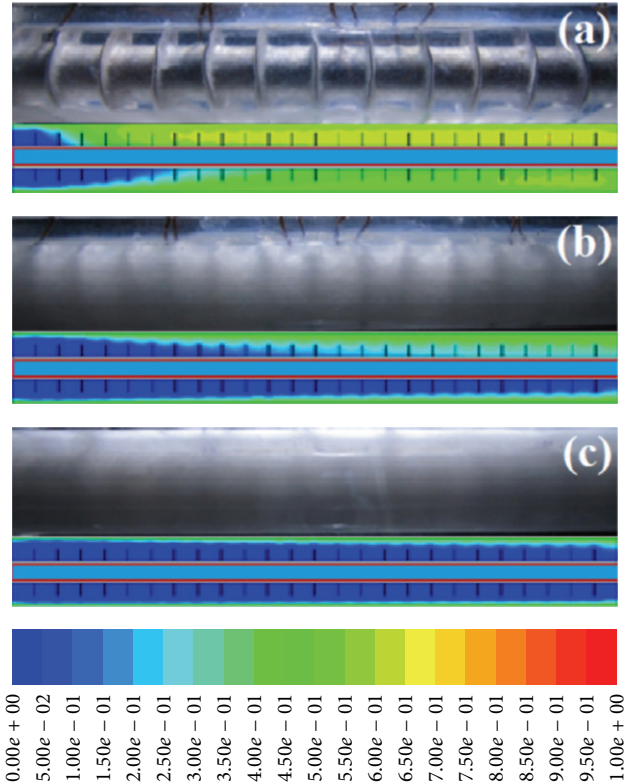


FIGURE 6: Solidification process for Re = 1000 at (a) 200 s, (b) 1000 s, and (c) 1800 s.

presents the temperature distribution's temporal variation at the lengthy points that are similarly distanced from the tube wall of HTF. The PCM temperature at particular positions reduces slowly with time, as demonstrated before; temporal variation becomes almost uniform after some time due to the initial impact and effectiveness of natural convection on heat transfer. After that, conduction becomes the only dominating mechanism in heat transfer, with lower convection impacts in contrast to the melting or charging instances. This happens due to the melted PCM's circulation quantity that is influenced by the decreasing natural convection with the increase in time as a result of the outward HTF tube's solidification. In the same vein, the process of solidification will speed up with increasing Reynolds number in the discharging process. For a clearer explanation, Figures 6(a), 6(b), and 6(c) depict the results for Re = 1000 where the ordinary and normal behavior of a transmission occurs. It is clear that solidification occurred homogeneously with increasing time.

### 5. Conclusion

An experimental investigation of the melting and solidification behavior of paraffin is presented in the current study. A thermal unit of storing energy, which has a horizontal finned-tube heat exchanger, was selected. According to the experimental results, the melting behavior of the points situated in the upper areas is drastically different from those in lower areas; moreover, this behavior repeated from

the inlet points to the exit points around the finned-tube. The experimental results also confirmed that the natural convection currents lead to the upward movement of molten PCM to the storage unit's upper regions. An asymmetric temperature field is created due to the radially upward extension of the melting area. For this reason the points in the upper left areas reach melting temperature faster than the ones in the lower right areas. By examining the solidification behavior, it was identified that the natural convection is initially effectual on heat transfer, which is later surpassed by conduction. As expected, increasing the Reynolds number is believed to improve the process of phase change within the PCM. The heat transfer rate and consequently the time to complete the melting process are directly related to Reynolds number. The present study demonstrated that, by increasing the Reynolds number from 1000 to 2000, the total melting time decreases by 58%. It should be noted that decreasing charging time and increasing discharge time are important subjects that should be investigated more in future work. This perceived asymmetric behavior may lead to the creation of new, innovative designs.

### Conflict of Interests

The authors declare that there is no conflict of interests regarding the publication of this paper.

### Acknowledgment

This work has been supported by the University of Malaya, Grant nos. RP001C-13AET and IPPP-PG066-2014A.

### References

- [1] Z. Liu, Z. Wang, and C. Ma, "An experimental study on the heat transfer characteristics of a heat pipe heat exchanger with latent heat storage. Part II: simultaneous charging/discharging modes," *Energy Conversion and Management*, vol. 47, no. 7-8, pp. 967-991, 2006.
- [2] H. Mehling and L. F. Cabeza, *Heat and Cold Storage with PCM: An Up to Date Introduction Into Basics and Applications*, Springer, 2008.
- [3] A. I. Fernandez, M. Martnez, M. Segarra, I. Martorell, and L. F. Cabeza, "Selection of materials with potential in sensible thermal energy storage," *Solar Energy Materials and Solar Cells*, vol. 94, no. 10, pp. 1723-1729, 2010.
- [4] M. Akgün, O. Aydin, and K. Kaygusuz, "Thermal energy storage performance of paraffin in a novel tube-in-shell system," *Applied Thermal Engineering*, vol. 28, no. 5-6, pp. 405-413, 2008.
- [5] M. Avci and M. Y. Yazici, "Experimental study of thermal energy storage characteristics of a paraffin in a horizontal tube-in-shell storage unit," *Energy Conversion and Management*, vol. 73, pp. 271-277, 2013.
- [6] A. F. Regin, S. C. Solanki, and J. S. Saini, "Heat transfer characteristics of thermal energy storage system using PCM capsules: a review," *Renewable and Sustainable Energy Reviews*, vol. 12, no. 9, pp. 2438-2458, 2008.
- [7] F. Agyenim, N. Hewitt, P. Eames, and M. Smyth, "A review of materials, heat transfer and phase change problem formulation for latent heat thermal energy storage systems (LHTESS)," *Renewable and Sustainable Energy Reviews*, vol. 14, no. 2, pp. 615-628, 2010.
- [8] J. Banaszek, R. Domański, M. Rebow, and F. El-Sagier, "Numerical analysis of the paraffin wax-air spiral thermal energy storage unit," *Applied Thermal Engineering*, vol. 20, no. 4, pp. 323-354, 2000.
- [9] A. Sari, "Form-stable paraffin/high density polyethylene composites as solid-liquid phase change material for thermal energy storage: preparation and thermal properties," *Energy Conversion and Management*, vol. 45, no. 13-14, pp. 2033-2042, 2004.
- [10] S. P. Jesumathy, M. Udayakumar, and S. Suresh, "Heat transfer characteristics in latent heat storage system using paraffin wax," *Journal of Mechanical Science and Technology*, vol. 26, no. 3, pp. 959-965, 2012.
- [11] B. Zalba, J. M. Marín, L. F. Cabeza, and H. Mehling, "Review on thermal energy storage with phase change: materials, heat transfer analysis and applications," *Applied Thermal Engineering*, vol. 23, no. 3, pp. 251-283, 2003.
- [12] S. Mondal, "Phase change materials for smart textiles—an overview," *Applied Thermal Engineering*, vol. 28, no. 11-12, pp. 1536-1550, 2008.
- [13] R. Murray, L. Desgrosseilliers, J. Stewart et al., "Design of a latent heat energy storage system coupled with a domestic hot water solar thermal system," in *Proceedings of the World Renewable Energy Congress (WREC '11)*, Linköping, Sweden, May 2011.
- [14] L. R. J. Desgrosseilliers, *Heat transfer enhancements using laminate film encapsulation for phase change heat storage materials [M.S. thesis]*, Dalhousie University, 2012.
- [15] Y. Zhang and A. Faghri, "Semi-analytical solution of thermal energy storage system with conjugate laminar forced convection," *International Journal of Heat and Mass Transfer*, vol. 39, no. 4, pp. 717-724, 1996.
- [16] M. Lacroix, "Study of the heat transfer behavior of a latent heat thermal energy storage unit with a finned tube," *International Journal of Heat and Mass Transfer*, vol. 36, no. 8, pp. 2083-2092, 1993.
- [17] Y. Cao and A. Faghri, "Performance characteristics of a thermal energy storage module: a transient PCM/forced convection conjugate analysis," *International Journal of Heat and Mass Transfer*, vol. 34, no. 1, pp. 93-101, 1991.
- [18] K. A. R. Ismail and F. A. M. Lino, "Fins and turbulence promoters for heat transfer enhancement in latent heat storage systems," *Experimental Thermal and Fluid Science*, vol. 35, no. 6, pp. 1010-1018, 2011.
- [19] M. Akgün, O. Aydin, and K. Kaygusuz, "Experimental study on melting/solidification characteristics of a paraffin as PCM," *Energy Conversion and Management*, vol. 48, no. 2, pp. 669-678, 2007.
- [20] Z. Liu, X. Sun, and C. Ma, "Experimental study of the characteristics of solidification of stearic acid in an annulus and its thermal conductivity enhancement," *Energy Conversion and Management*, vol. 46, no. 6, pp. 971-984, 2005.
- [21] Z. Liu, X. Sun, and C. Ma, "Experimental investigations on the characteristics of melting processes of stearic acid in an annulus and its thermal conductivity enhancement by fins," *Energy Conversion and Management*, vol. 46, no. 6, pp. 959-969, 2005.
- [22] C. Bellecci and M. Conti, "Phase change thermal storage: transient behaviour analysis of a solar receiver/storage module using the enthalpy method," *International Journal of Heat and Mass Transfer*, vol. 36, no. 8, pp. 2157-2163, 1993.

- [23] A. A. Al-Abidi, S. Mat, K. Sopian, M. Y. Sulaiman, and A. T. Mohammad, "Internal and external fin heat transfer enhancement technique for latent heat thermal energy storage in triplex tube heat exchangers," *Applied Thermal Engineering*, vol. 53, no. 1, pp. 147–156, 2013.
- [24] K. Ismail and C. Alves, "Phase change thermal energy storage in shell and circular-tube annulus configuration," in *Alternative Energy Sources*, T. Nejat and B. Veziroglu, Eds., Hemisphere Publishing Corporation, Miami, Fla, USA, 1987.
- [25] Y. Cao, A. Faghri, and A. Juhasz, "A PCM/forced convection conjugate transient analysis of energy storage systems with annular and countercurrent flows," *The ASME Transactions Journal of Heat Transfer*, vol. 113, no. 1, pp. 37–42, 1991.
- [26] X. Chen, M. Worall, S. Omer, Y. Su, and S. Riffat, "Experimental investigation on PCM cold storage integrated with ejector cooling system," *Applied Thermal Engineering*, vol. 63, no. 1, pp. 419–427, 2014.
- [27] A. G. Bathelt and R. Viskanta, "Heat transfer and interface motion during melting and solidification around a finned heat source/sink," *Journal of Heat Transfer*, vol. 103, no. 4, pp. 720–726, 1981.
- [28] L. F. Cabeza, H. Mehling, S. Hiebler, and F. Ziegler, "Heat transfer enhancement in water when used as PCM in thermal energy storage," *Applied Thermal Engineering*, vol. 22, no. 10, pp. 1141–1151, 2002.
- [29] C. S. Oon, A. Al-Shammaa, S. N. Kazi, B. T. Chew, A. Badarudin, and E. Sadeghinezhad, "Simulation of heat transfer to separation air flow in a concentric pipe," *International Communications in Heat and Mass Transfer*, vol. 57, pp. 48–52, 2014.
- [30] M. R. Safaei, H. R. Goshayeshi, B. S. Razavi, and M. Goodarzi, "Numerical investigation of laminar and turbulent mixed convection in a shallow water-filled enclosure by various turbulence methods," *Scientific Research and Essays*, vol. 6, no. 22, pp. 4826–4838, 2011.
- [31] H. Yarmand, S. Gharekhani, S. N. Kazi, E. Sadeghinezhad, and M. R. Safaei, "Numerical investigation of heat transfer enhancement in a rectangular heated pipe for turbulent nanofluid," *The Scientific World Journal*, vol. 2014, Article ID 369593, 9 pages, 2014.
- [32] M. R. Safaei, B. Rahmanian, and M. Goodarzi, "Numerical study of laminar mixed convection heat transfer of power-law non-Newtonian fluids in square enclosures by finite volume method," *International Journal of Physical Sciences*, vol. 6, no. 33, pp. 7456–7470, 2011.
- [33] S. V. Patankar, *Numerical Heat Transfer and Fluid Flow*, Taylor & Francis, 1980.
- [34] E. Sadeghinezhad, H. Togun, M. Mehrli et al., "An experimental and numerical investigation of heat transfer enhancement for graphene nanoplatelets nanofluids in turbulent flow conditions," *International Journal of Heat and Mass Transfer*, vol. 81, pp. 41–51, 2015.
- [35] H. R. Goshayeshi, M. R. Safaei, and Y. Maghmoumi, "Numerical simulation of unsteady turbulent and laminar mixed convection in rectangular enclosure with hot upper moving wall by finite volume method," in *Proceedings of the 6th International Chemical Engineering Congress and Exhibition (ICChE '09)*, Kish Island, Iran, 2009.
- [36] M. Odabae and K. Hooman, "Metal foam heat exchangers for heat transfer augmentation from a tube bank," *Applied Thermal Engineering*, vol. 36, no. 1, pp. 456–463, 2012.
- [37] G. Ji, G. Wang, K. Hooman, S. Bhatia, and J. C. Diniz da Costa, "The fluid dynamic effect on the driving force for a cobalt oxide silica membrane module at high temperatures," *Chemical Engineering Science*, vol. 111, pp. 142–152, 2014.
- [38] A. Karimipour, M. Afrand, M. Akbari, and M. R. Safaei, "Simulation of fluid flow and heat transfer in the inclined enclosure," *International Journal of Mechanical and Aerospace Engineering*, vol. 6, pp. 86–91, 2012.
- [39] M. R. Safaei, M. Goodarzi, and M. Mohammadi, "Numerical modeling of turbulence mixed convection heat transfer in air filled enclosures by finite volume method," *International Journal of Multiphysics*, vol. 5, no. 4, pp. 307–324, 2011.
- [40] M. J. Hosseini, M. Rahimi, and R. Bahrapoury, "Experimental and computational evolution of a shell and tube heat exchanger as a PCM thermal storage system," *International Communications in Heat and Mass Transfer*, vol. 50, pp. 128–136, 2014.
- [41] O. Aydin, M. Akgün, and K. Kaygusuz, "An experimental optimization study on a tube-in-shell latent heat storage," *International Journal of Energy Research*, vol. 31, no. 3, pp. 274–287, 2007.

## Research Article

# CFD Convective Flow Simulation of the Varying Properties of CO<sub>2</sub>-H<sub>2</sub>O Mixtures in Geothermal Systems

S. Yousefi,<sup>1</sup> A. D. Atrens,<sup>2</sup> E. Sauret,<sup>3</sup> M. Dahari,<sup>4</sup> and K. Hooman<sup>2</sup>

<sup>1</sup>Mechanical Engineering Department, Islamic Azad University, Gachsaran Branch, Gachsaran, Iran

<sup>2</sup>School of Mechanical and Mining Engineering, The University of Queensland, Brisbane, QLD 4072, Australia

<sup>3</sup>School of Chemistry, Physics and Mechanical Engineering, Queensland University of Technology, Brisbane, QLD 4000, Australia

<sup>4</sup>Department of Mechanical Engineering, Faculty of Engineering, University of Malaya, 50603 Kuala Lumpur, Malaysia

Correspondence should be addressed to K. Hooman; k.hooman@uq.edu.au

Received 14 July 2014; Accepted 23 July 2014

Academic Editor: M. R. Safaei

Copyright © 2015 S. Yousefi et al. This is an open access article distributed under the Creative Commons Attribution License, which permits unrestricted use, distribution, and reproduction in any medium, provided the original work is properly cited.

Numerical simulation of a geothermal reservoir, modelled as a bottom-heated square box, filled with water-CO<sub>2</sub> mixture is presented in this work. Furthermore, results for two limiting cases of a reservoir filled with either pure water or CO<sub>2</sub> are presented. Effects of different parameters including CO<sub>2</sub> concentration as well as reservoir pressure and temperature on the overall performance of the system are investigated. It has been noted that, with a fixed reservoir pressure and temperature, any increase in CO<sub>2</sub> concentration leads to better performance, that is, stronger convection and higher heat transfer rates. With a fixed CO<sub>2</sub> concentration, however, the reservoir pressure and temperature can significantly affect the overall heat transfer and flow rate from the reservoir. Details of such variations are documented and discussed in the present paper.

## 1. Introduction

Simultaneous power generation and geosequestration make CO<sub>2</sub> a very attractive choice for geothermal power plants. As such, carbon-dioxide-based engineered geothermal systems (CO<sub>2</sub>-EGS) have been previously proposed as an alternative to water-based EGS systems [1]. Subsequent studies added further details and reported possibility of improved energy extraction [2–7]. Interestingly, the “dry-out period,” or transition from an initially water-filled EGS system to a CO<sub>2</sub>-rich one [8–11] has received a lot of attention mainly because of possible mineral dissolution and precipitation as a result of changes in the reservoir fluid composition and reservoir permeability alteration [12–14]. Additionally, [15] investigated the effects of CO<sub>2</sub>-rich phase compositions on the production flow rate and the heat extraction from the reservoir. What is yet to be reported in the literature is a detailed numerical simulation of a water-CO<sub>2</sub> mixture filling a reservoir. Simple thermodynamic analysis of a reservoir shows that more heat can be extracted (compared to a water-saturated reservoir) mainly because a CO<sub>2</sub>-water mixture

is more buoyant than pure water. This could significantly affect the energy extraction from a water-saturated reservoir. Most of these reservoirs suffer from permeability drops with depths. As such, having a more buoyant fluid which could move up against gravity, at least partially, not only is desirable but also is going to significantly affect the drilling cost which is expected to grow exponentially with the well depth [16–18].

The role of fluid migration in the build-up of heat in underground geothermal systems is not well understood. It is known that degassing of CO<sub>2</sub> with isotopic composition indicating mantle-sources in regions of tectonic activity is associated with locally elevated geothermal temperatures [19–21]. Convective fluid plumes may play a role in enhancing heat flows from the mantle to geothermal reservoirs and within the reservoirs themselves. Additionally, convection within a geothermal reservoir may enhance the productive life-time of geothermal reservoir systems by enhancing heat supply from underlying strata and by ensuring a more even distribution of thermal energy throughout the reservoir, that is, by off-setting localized cooling along major flow paths.

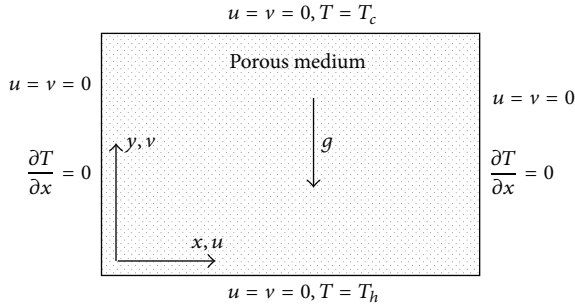


FIGURE 1: Schematic view of the computational domain.

This could also imply that for a water-saturated reservoir which is classified as nonproductive, mainly due to lack of convection currents, injection of  $\text{CO}_2$  can lead to formation of convection cells and thus facilitate heat extraction. In what follows, a numerical analysis of this problem is presented to quantitatively measure the improved convective flow patterns and enhanced heat transfer from the reservoir. This is intended to provide insight as to the possible mechanisms by which  $\text{CO}_2$  presence in or addition to underground reservoirs could lead to enhancement of convective heat transfer.

## 2. Modelling

The reservoir is modelled as a bottom-heated square box with adiabatic lateral boundaries and a cold top wall as Figure 1 shows. The cold and hot temperatures are varied from 331 to 431 K and 416 to 516 K, respectively, in a way that the hot-cold temperature difference remains at 85 K for each case. For constant properties, and of course with the same reservoir size, porosity, and permeability, one would expect the results to be the same as long as the temperature difference is not altered. It will, however, be shown in the forthcoming sections that this is not the case in our problem as properties significantly vary with both temperature and pressure. The reservoir porosity is fixed at 0.05 and the permeability-length product is kept constant at  $10^{-11} \text{ m}^3$  similar to Haghshenas Fard et al. [7] with no through-flow. The reservoir pressure is varied from 20 to 60 MPa (equivalent to the hydrostatic pressure of approximately 2 to 6 km of water) to cover a wide range of practical applications for geothermal development. The flow is modelled using Darcy flow model with the single-phase fluid properties obtained as linear superposition of those of individual fluids weighted with their respective fraction; that is,

$$\begin{aligned} \rho_g &= \omega_\gamma \rho_\gamma + \omega_\epsilon \rho_\epsilon, \\ \beta_g &= \omega_\gamma \beta_\gamma + \omega_\epsilon \beta_\epsilon, \\ c_{pg} &= \omega_\gamma c_{p\gamma} + \omega_\epsilon c_{p\epsilon}, \\ \mu_g &= \omega_\gamma \mu_\gamma + \omega_\epsilon \mu_\epsilon. \end{aligned} \quad (1)$$

The real (i.e., nonideal) properties are determined for pure  $\text{CO}_2$  using a Helmholtz-free-energy based equation of state [22] and for pure  $\text{H}_2\text{O}$  using the International Association

for the Properties of Water and Steam equation of state [23]. The use of a single-phase basis for modelling is to enable examination of the effect of changing properties without additional complexities of two-phase flow separation behaviour. Further comment is provided in the discussion. The reservoir properties are then obtained similarly using the porosity and solidity as the weight-functions as follows:

$$\lambda_R = \phi (\omega_\gamma \lambda_\gamma + \omega_\epsilon \lambda_\epsilon) + (1 - \phi) \lambda_m. \quad (2)$$

One notes that in the above formulation changes in the reservoir porosity and permeability are not taken into account while fluid properties are updated in each iteration.

An in-house code, used by Hooman and Gurgenci [24], was cross-validated with the commercially available software ANSYS-FLUENT and used to create and mesh the geometry and finally solve the governing equations. The governing equations were derived as for standard two-dimensional heat transfer conditions, based on the assumptions of adiabatic lateral walls and constant temperature for the top and bottom boundaries, and are as follows:

$$\begin{aligned} \frac{\partial u}{\partial x} + \frac{\partial v}{\partial y} &= 0, \\ \frac{\partial u}{\partial y} - \frac{\partial v}{\partial x} &= -\frac{\rho g \beta K}{\mu} \frac{\partial T}{\partial x}, \\ u \frac{\partial T}{\partial x} + v \frac{\partial T}{\partial y} &= \alpha \left( \frac{\partial^2 T}{\partial x^2} + \frac{\partial^2 T}{\partial y^2} \right), \end{aligned} \quad (3)$$

subject to the boundary conditions illustrated in Figure 1.

## 3. Numerical Details

Grid independence was verified by running the software on different combination of grid sizes. It was observed that the results changed less than 2% when a  $100 \times 100$  mesh system is used instead of a finer mesh with  $200 \times 200$  grid points. Results are also verified for constant property free convection of water in a porous cavity, that is, the Darcy-Benard problem. It was noted that the correlation between Nusselt number (Nu) and Rayleigh number (Ra)  $\text{Nu} = \text{Ra}/40$  best fits out numerical data, as Figure 2 shows. Ra in this instance is determined as per

$$\text{Ra} = \frac{g \beta \rho}{\mu \alpha} (T_h - T_c) KH. \quad (4)$$

As a further check on the accuracy of our results, variable property Darcy-Benard free convection of pure water in a porous cavity was investigated to observe that using the reference temperature approach of Hooman and Gurgenci [24] the above correlation can still be used within 5%.

## 4. Results and Discussion

In what follows we focus on free convection heat and fluid flow of a water- $\text{CO}_2$  mixture in a porous cavity. We use Nu and maximum flow rate as our metrics to evaluate the

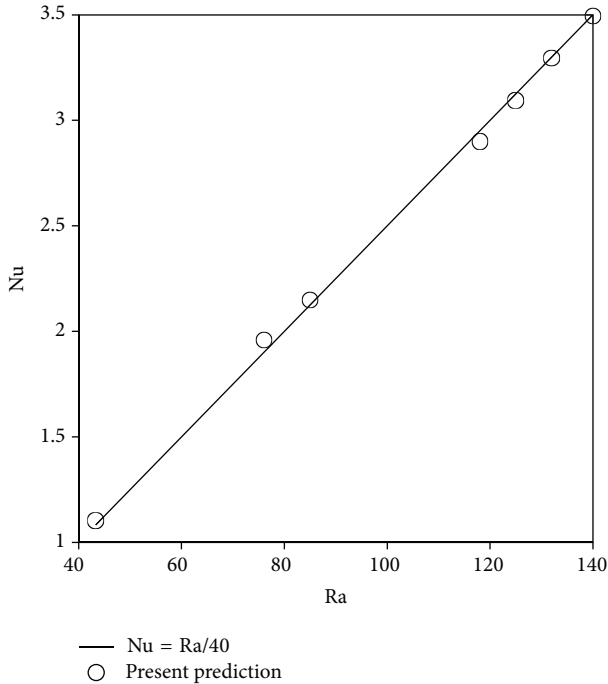


FIGURE 2: Validation of present CFD results against existing correlation for pure water.

strength of convective flow patterns. Nu is the total heat transfer divided by that of pure conduction through the same cavity (no convective flow patterns). As such, any Nu value in excess of unity shows some degree of convection. Obviously, higher Nu values mark stronger convective cells. The flow rate reported here is the one induced by free convection only, that is, without a well-head pump or any other suction/injection mechanisms. We systematically change the CO<sub>2</sub> mass fraction from zero (pure water) to unity (pure CO<sub>2</sub>) over a range of reservoir pressure and temperature in a way that the hot-cold temperature difference remains the same. For a constant property subcritical fluid flow, one would expect that, with the same temperature difference and, hence, the same Rayleigh number (Ra), the overall heat transfer and fluid flow will not alter. However, as CO<sub>2</sub> is supercritical within the range of conditions of underground reservoir systems, that is not the case for mixtures of CO<sub>2</sub> and H<sub>2</sub>O, as demonstrated by Figure 3. This figure shows Nu versus CO<sub>2</sub> mass fraction at 20 MPa with the same hot-cold temperature difference but with different hot and cold temperatures as denoted on the plots. As seen, the heat transfer increases with CO<sub>2</sub> mass fraction for any given T<sub>h</sub> and T<sub>c</sub> combination. Furthermore, moving from pure water to pure CO<sub>2</sub>, the increase in heat transfer is significant; about one order of magnitude is the minimal heat transfer augmentation. More interestingly, however, is the fact that Nu is the highest with the lowest T<sub>c</sub> (and obviously lowest T<sub>h</sub> to maintain the same ΔT of 85 K) mainly because the lower temperatures are closer to those of pseudocritical conditions where Ra is expected to reach a maximum value; see also Forooghi et al. [25–28]. This is obviously in favour of low temperature geothermal

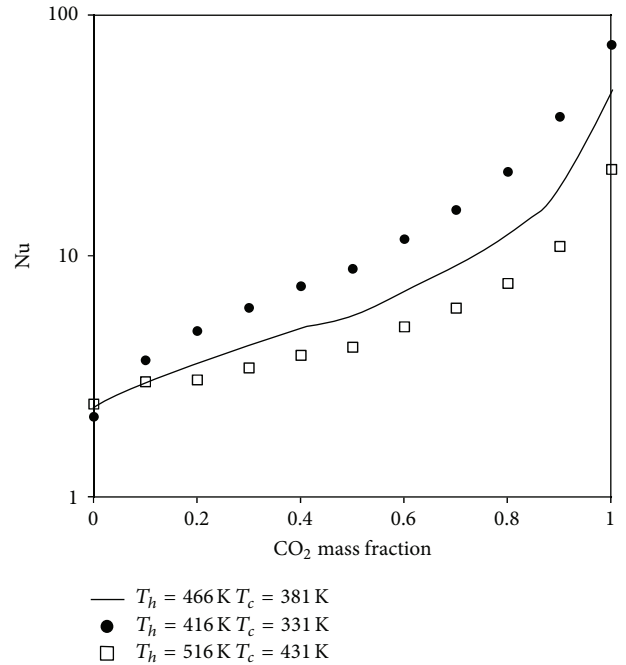


FIGURE 3: Nusselt number versus CO<sub>2</sub> mass fraction for different T<sub>h</sub> and T<sub>c</sub> combinations with ΔT = 85 K.

reservoirs which may not be productive when pure water is the working fluid.

Figures 4(a)–4(c) are presented to demonstrate Nu versus CO<sub>2</sub> mass fraction for different reservoir pressures and hot-cold temperature combinations. Nu increases with mass fraction for a fixed pressure and hot-cold temperature combination. Comparing the relationship between any of Figures 4(a)–4(c) for a fixed pressure will result in conclusions similar to what were drawn based on close examination of Figure 3. That is, heat transfer increases for temperatures close to pseudocritical conditions. Moreover, based on plots in the same chart, increasing the pressure leads to lower heat transfer rates for a fixed CO<sub>2</sub> mass fraction and temperature. This could be explained as the obvious decrease in compressibility and increase in the fluid density with higher pressures, with a fixed fluid temperature, which will lead to lower thermal expansion coefficients. As a result, at the same temperature, either of the two fluids will be less buoyant at higher pressures when compared to lower ones, so will be the mixture in the absence of any phase transitions.

The convective flow rates also reflect a dependence on compressibility, as demonstrated by Figure 5. The dimensionless flow rate (normalized stream function on the vertical axis) is obtained by normalizing the actual flow rate with appropriate scales for velocity, area, and density:

$$\xi = \frac{\dot{m}}{(\rho u A)} \tag{5}$$

Mathematically, it means that we used the group  $\rho Au$  to nondimensionalize the flow rate. It needs to be mentioned that the choice of these parameters is optional but we tried to use constant values for density and length to make it easy

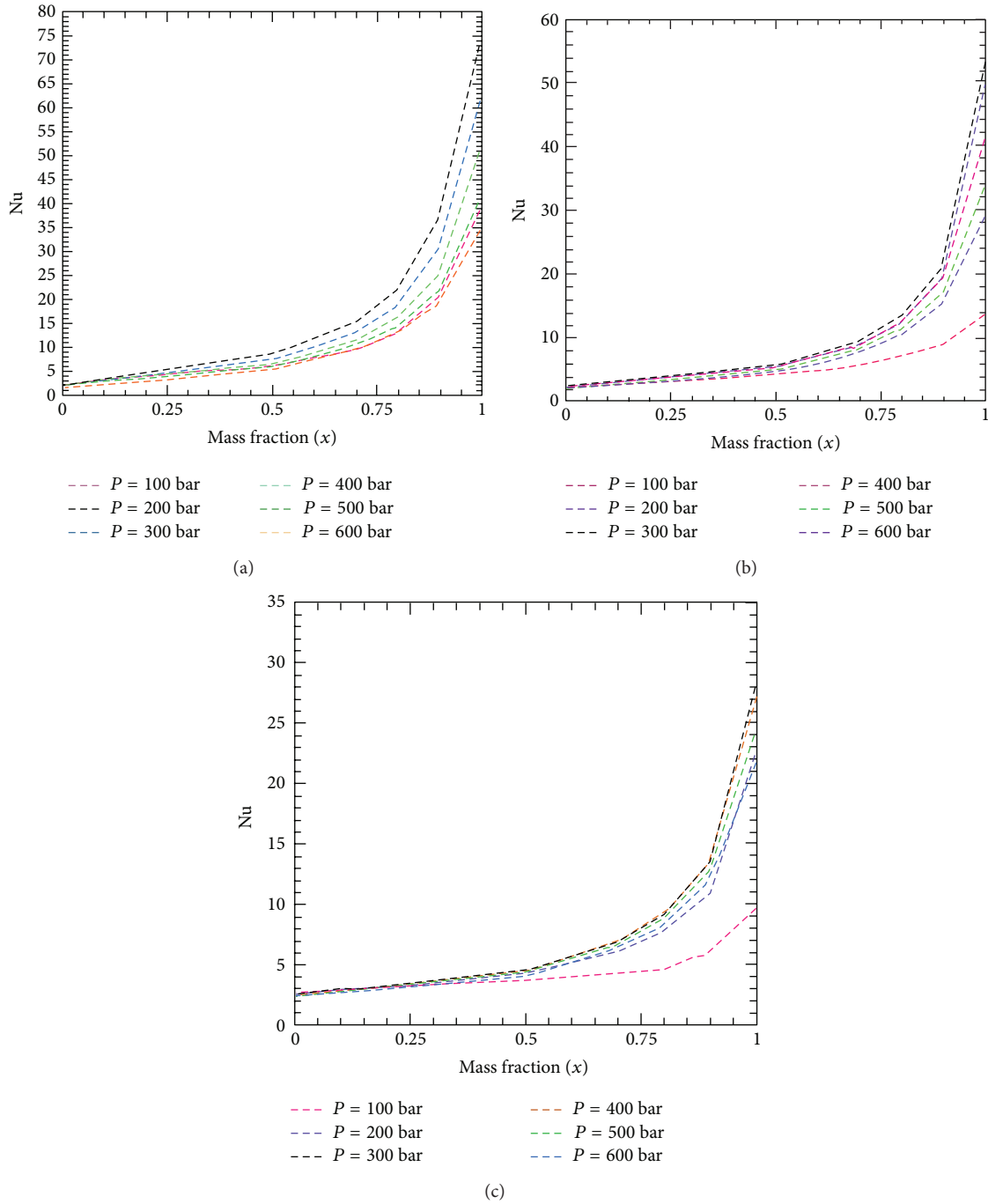


FIGURE 4: Nusselt number versus CO<sub>2</sub> mass fraction for different reservoir pressures and temperature combinations: (a)  $T_h = 416\text{ K}; T_c = 331\text{ K}$ , (b)  $T_h = 466\text{ K}; T_c = 381\text{ K}$ , and (c)  $T_h = 516\text{ K}; T_c = 431\text{ K}$ .

for the reader to generate estimates, based on our calculation, for expected flow rates through a given reservoir. Moreover, what we are more interested in is the trend of the flow rate plot against the mass fraction than the actual flow rate values. In doing so, the (constant) density of water at atmospheric condition is used where the unit area is used defined as the length of the cavity multiplied by unity (1 m). The flow velocity, for single-phase constant property case, is assumed to be linearly proportional to the product of the thermal

diffusivity and  $Ra^{1/2}$  and inverse linearly proportional to the cavity length; for example,

$$u \sim \frac{\alpha}{H} \sqrt{Ra}. \tag{6}$$

The flow rate is given by

$$\dot{m} = \rho H u \sim \rho \alpha \sqrt{Ra}. \tag{7}$$

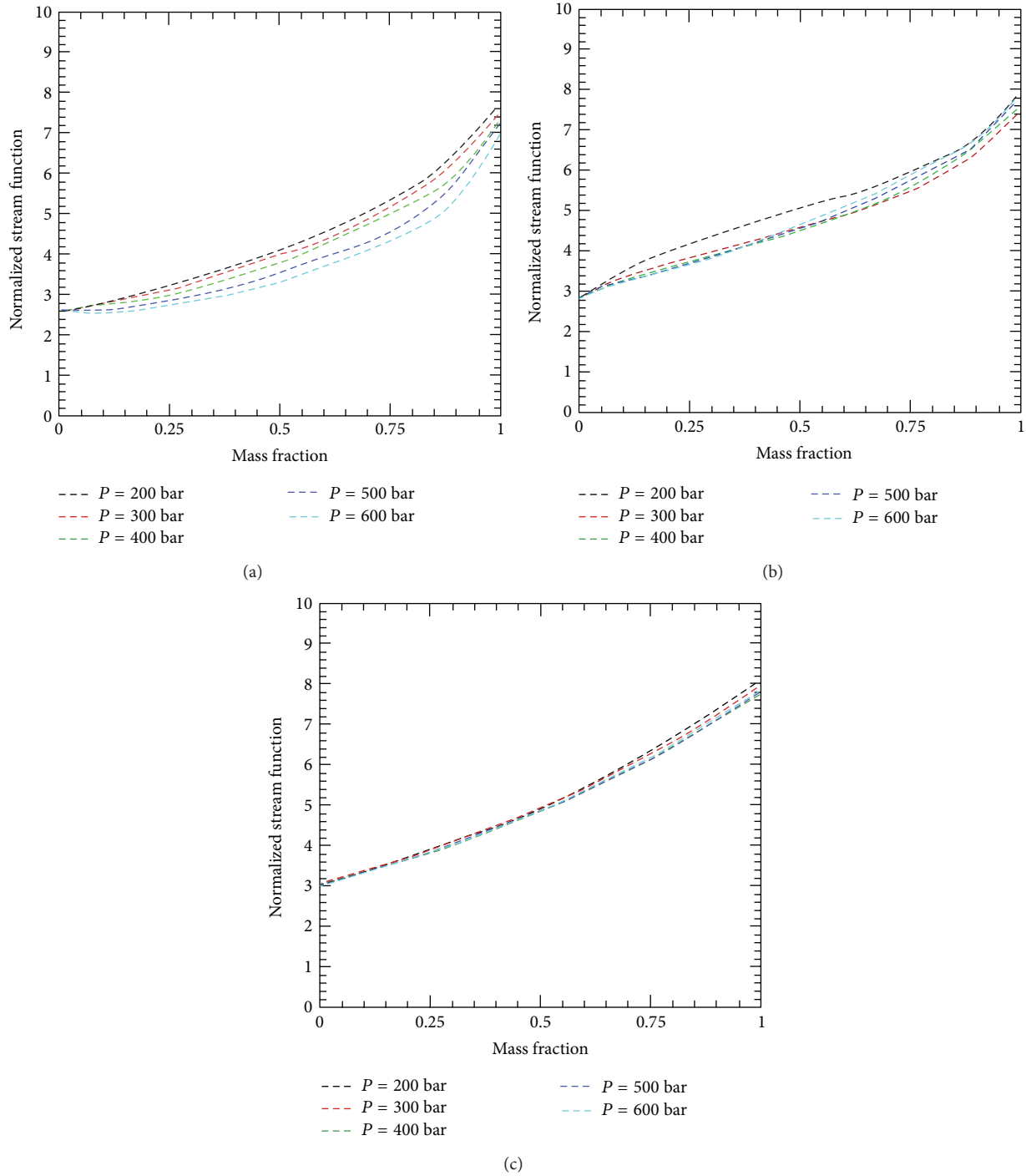


FIGURE 5: Dimensionless mass flow rate versus CO<sub>2</sub> mass fraction for different pressures and temperature combinations: (a)  $T_h = 416$  K;  $T_c = 331$  K, (b)  $T_h = 466$  K;  $T_c = 381$  K, and (c)  $T_h = 516$  K;  $T_c = 431$  K.

The product of thermal diffusivity and density is independent of density and leaves us with a group  $\lambda/c_p$ . Consequently the mass flow rate scale is represented as

$$\dot{m} = \rho H u \sim \frac{k}{c_p} \sqrt{Ra}. \tag{8}$$

While  $\lambda$  and  $c_p$  are calculated under standard atmospheric conditions, Ra is affected by fluid property variation and following the use of (1)-(2). This flow rate here is the buoyancy-induced flow rate due to changes in fluid density. The buoyancy-induced flow leads to an upward movement of hot fluid toward the top wall, where it is cooled and then displaced by other rising hot fluid. Results of mass flow rate

normalized by using (8) above are presented in Figure 5 for different mass fractions, pressure, and temperature combinations. Similar to Nu plots, one notes that the mass flow rate is sensitive not only to the temperature difference but also to the actual wall temperature values. Furthermore, higher CO<sub>2</sub> mass fraction leads to higher flow rates. It can be noted, moving from Figures 5(a) to 5(c), that flow rates are less sensitive to pressure as  $T_h$  is increased. With a fixed  $T_h$  and  $T_c$ , one notes different trends in flow rate when pressure changes. Depending on the temperature values, an increase in pressure can either increase (Figure 5(a)) or decrease the flow rate (Figure 5(b)).

This work is an initial analysis of the role of CO<sub>2</sub> enhancement of convective heat transfer within geothermal reservoirs. It deliberately assesses the behaviour of a single-phase mixture of the two components. Further work is necessary to extend this to account for multiple phases. There are three particular qualitative effects through which multiphase flow is expected to alter the results presented here.

- (1) Transient exsolution of dissolved CO<sub>2</sub> as bubbles within the two-phase region should lead to local enhancement of convective flow around the bubble due to its upwards buoyancy-driven motion. One expectation of this would be an increase in the gradient of convective heat flux with mass fraction (i.e.,  $d\xi/dx$ ) at the bubble line, where CO<sub>2</sub> begins to exsolve from the H<sub>2</sub>O phase.
- (2) Relative permeability within the two-phase region would act to reduce enhancement of flows, as the reservoir permeability to the minor phase within a two-phase flow is typically substantially reduced.
- (3) Under steady-state conditions, there would be an expectation of phase separation into two horizontal phases based on relative density, that is, an upper CO<sub>2</sub>-rich phase and a lower H<sub>2</sub>O-rich phase. The upper phase would experience significantly enhanced convective heat transfer rates, as it would have internal heat transfer characteristics similar to the right sides of Figures 4 and 5. Additionally, the heat transfer would be further enhanced by the temperature-dependent solubility of H<sub>2</sub>O in the CO<sub>2</sub>-rich phase, leading to additional H<sub>2</sub>O evaporating into the CO<sub>2</sub> phase at the boundary between the two phases and condensing at the upper surface of the reservoir. The H<sub>2</sub>O-rich phase would experience the converse effect, depressing the rate of heat transfer, although CO<sub>2</sub> solubility in H<sub>2</sub>O is far less dependent on temperature than that of H<sub>2</sub>O in CO<sub>2</sub> [11].

These expected qualitative behaviours require further analysis accounting for multiphase flow behaviour to determine their relative contribution to overall convective heat flow enhancement.

However, the sum of these changes is not expected to reverse the overall trend demonstrated here, of increased convective heat flux as CO<sub>2</sub> is added to the reservoir system. Considering that the results presented here indicate that CO<sub>2</sub> may enhance flow rates by up to a factor of 2.67, we conclude

that this is a potentially important mode of heat transport within geothermal reservoirs and warrants further study. We anticipate the next steps to be consideration of the additional flow behaviours when multiple phases are present.

## 5. Conclusion

The effect on convective heat transport within a closed reservoir system of varying fluid composition was analysed by CFD modelling of a single-phase fluid with properties derived from a composition-dependent average of pure CO<sub>2</sub> and pure H<sub>2</sub>O. As compositional properties were varied from H<sub>2</sub>O toward that of CO<sub>2</sub>, substantial increases were observed in Nusselt number (by a factor of up to 10) and normalised stream function (by a factor of up to 2.67). We conclude that this indicates substantial increase in convective heat transport.

Convective heat transport may be further modified by multiphase flow behaviours, and we conclude that, due to the potential magnitude of heat flow enhancement by the addition of CO<sub>2</sub>, further research exploring the effect of these behaviours on heat transport is warranted.

We anticipate this finding to have implications for the study of natural geothermal reservoirs, where the role of dissolved gas exsolution on heat transfer enhancement remains unquantified. Additionally, these findings may be of potential interest with regard to CO<sub>2</sub> injection into geothermal reservoirs, as it may lead to improved productivity through the mechanisms elucidated in this work.

The magnitude of this effect on the thermal productivity of geothermal power plants is difficult at this stage to quantify and probably not meaningful to speculate on due to the limitation of assessing only single-phase flow behaviours within the reservoir. These findings do demonstrate, however, that reservoirs with elevated CO<sub>2</sub> content will experience greater convective heat transfer and therefore be of comparatively higher temperature (and therefore of greater resource value). Additionally, it can be concluded that any increase in CO<sub>2</sub> content of an existing reservoir will enhance convective flow behaviours (although the true magnitude of this effect will depend on two-phase flow behaviour as well as the particulars of the reservoir) and consequently will enhance the productivity and/or the longevity of geothermal energy extraction.

## Glossary

- $\rho$ : Density, kg m<sup>-3</sup>
- $\omega$ : Mass fraction, dimensionless
- $\beta$ : Thermal expansion coefficient, K<sup>-1</sup>
- $\mu$ : Dynamic viscosity, Pa s
- $\lambda$ : Thermal conductivity W m<sup>-1</sup> K<sup>-1</sup>
- $\phi$ : Reservoir porosity, dimensionless
- $c_p$ : constant-pressure heat capacity, kJ kg<sup>-1</sup> K<sup>-1</sup>
- $g$ : Gravitational acceleration, 9.81 m s<sup>-2</sup>
- $u$ : Horizontal component of fluid velocity, m s<sup>-1</sup>
- $v$ : Vertical component of fluid velocity, m s<sup>-1</sup>
- Nu: Nusselt number, dimensionless
- Ra: Rayleigh number, dimensionless

$T$ : Temperature, K  
 $\xi$ : Normalised flow rate, dimensionless  
 $m$ : Mass flow rate,  $\text{kg s}^{-1}$   
 $A$ : Area,  $\text{m}^2$   
 $H$ : Reservoir height, m  
 $K$ : Reservoir permeability,  $\text{m}^2$   
 $\alpha$ : Thermal diffusivity,  $\text{m}^2 \text{s}^{-1}$ .

### Subscripts

$\gamma$ : Carbon dioxide  
 $\varepsilon$ : Water  
 $g$ : Fluid mixture  
 $R$ : Reservoir  
 $m$ : Rock  
 $h$ : Highest system temperature, at bottom boundary  
 $c$ : Lowest system temperature, at top boundary.

### Conflict of Interests

The authors declare that they have no conflict of interests regarding the publication of this paper.

### Acknowledgments

Support from High Impact Research Grant UM.C/HIR/MOHE/ENG/23 and the University of Malaya, Malaysia, is acknowledged.

### References

- [1] D. W. Brown, "A hot dry rock geothermal energy concept utilizing supercritical  $\text{CO}_2$  instead of water," in *Proceedings of the 25th Workshop on Geothermal Reservoir Engineering*, Stanford University, Stanford, Calif, USA, 2000.
- [2] K. Pruess, "Enhanced geothermal systems (EGS) using  $\text{CO}_2$  as working fluid—a novel approach for generating renewable energy with simultaneous sequestration of carbon," *Geothermics*, vol. 35, no. 4, pp. 351–367, 2006.
- [3] H. Guoqiang and W. Jiong, "Extrapolation of Nystrom solution for two dimensional nonlinear Fredholm integral equations," *Journal of Computational and Applied Mathematics*, vol. 134, no. 1-2, pp. 259–268, 2001.
- [4] A. D. Atrens, H. Gurgenci, and V. Rudolph, " $\text{CO}_2$  Thermosiphon for competitive geothermal power generation," *Energy and Fuels*, vol. 23, no. 1, pp. 553–557, 2009.
- [5] A. Nago and A. Nieto, "Natural gas production from methane hydrate deposits using  $\text{CO}_2$  clathrate sequestration: state-of-the-art review and new technical approaches," *Journal of Geological Research*, vol. 2011, Article ID 239397, 6 pages, 2011.
- [6] K. Hooman, A. Tamayol, M. Dahari, M. R. Safaei, H. Togun, and R. Sadri, "A theoretical model to predict gas permeability for slip flow through a porous medium," *Applied Thermal Engineering*, vol. 70, no. 1, pp. 71–76, 2014.
- [7] M. Haghshenas Fard, K. Hooman, and H. T. Chua, "Numerical simulation of a supercritical  $\text{CO}_2$  geothermosiphon," *International Communications in Heat and Mass Transfer*, vol. 37, no. 10, pp. 1447–1451, 2010.
- [8] A. D. Atrens, H. Gurgenci, and V. Rudolph, "Economic optimization of a  $\text{CO}_2$ -based EGS power plant," *Energy and Fuels*, vol. 25, no. 8, pp. 3765–3775, 2011.
- [9] A. D. Atrens, H. Gurgenci, and V. Rudolph, "Removal of water for carbon dioxide-based EGS operation," in *Proceedings of the 36th Workshop on Geothermal Reservoir Engineering*, Stanford University, Stanford, Calif, USA, 2011.
- [10] A. Borgia, K. Pruess, J. T. Kneafsey, C. M. Oldenburg, and L. Pan, "Simulation of  $\text{CO}_2$ -EGS in a fractured reservoir with salt precipitation," in *Proceedings of the 37th Workshop on Geothermal Reservoir Engineering*, Stanford, Calif, USA, 2012.
- [11] A. D. Atrens, H. Gurgenci, and V. Rudolph, "Water condensation in carbon-dioxide-based engineered geothermal power generation," *Geothermics*, vol. 51, pp. 397–405, 2014.
- [12] T. J. Kneafsey and K. Pruess, "Laboratory flow experiments for visualizing carbon dioxide-induced, density-driven brine convection," *Transport in Porous Media*, vol. 82, no. 1, pp. 123–139, 2010.
- [13] N. Spycher and K. Pruess, "A Phase-partitioning model for  $\text{CO}_2$ -brine mixtures at elevated temperatures and pressures: application to  $\text{CO}_2$ -enhanced geothermal systems," *Transport in Porous Media*, vol. 82, no. 1, pp. 173–196, 2010.
- [14] N. Spycher and K. Pruess, "A model for thermophysical properties of  $\text{CO}_2$ -brine mixtures at elevated temperatures and pressures," in *Proceedings of the 36th Workshop on Geothermal Reservoir Engineering*, Stanford, Calif, USA, 2011.
- [15] A. D. Atrens and H. Gurgenci, "Design of  $\text{CO}_2$ -based geothermal power plant for transient reservoir dry-out—or 'enhanced water recovery,'" in *Proceedings of the 38th Workshop on Geothermal Reservoir Engineering*, Stanford University, Stanford, Calif, USA, 2013.
- [16] A. D. Atrens, H. Gurgenci, and V. Rudolph, "Economic analysis of a  $\text{CO}_2$  thermosiphon," in *Proceedings of the World Geothermal Congress*, Bali, Indonesia, 2010.
- [17] A. D. Atrens, H. Gurgenci, and V. Rudolph, "Electricity generation using a carbon-dioxide thermosiphon," *Geothermics*, vol. 39, no. 2, pp. 161–169, 2010.
- [18] C. Augustine, J. W. Tester, B. Anderson, S. Petty, and B. Livesay, "A comparison of geothermal with oil and gas well drilling costs," in *Proceedings of the 31st Workshop on Geothermal Reservoir Engineering*, Stanford University, Stanford, Calif, USA, 2006.
- [19] F. Italiano, G. Yuce, I. T. Uysal, and M. Gasparon, "Noble gas isotopic studies of  $\text{CO}_2$ -rich waters in Australian sedimentary basins with geothermal energy potential," in *Proceedings of the International Conference on Gas Geochemistry (ICGG'11)*, La Jolla, Calif, USA, 2011.
- [20] I. T. Uysal, Y.-X. Feng, J.-X. Zhao, V. Isik, P. Nuriel, and S. D. Golding, "Hydrothermal  $\text{CO}_2$  degassing in seismically active zones during the late Quaternary," *Chemical Geology*, vol. 265, no. 3-4, pp. 442–454, 2009.
- [21] I. T. Uysal, S. D. Golding, R. Bolhar et al., " $\text{CO}_2$  degassing and trapping during hydrothermal cycles related to Gondwana rifting in eastern Australia," *Geochimica et Cosmochimica Acta*, vol. 75, no. 19, pp. 5444–5466, 2011.
- [22] R. Span and W. Wagner, "A new equation of state for carbon dioxide covering the fluid region from the triple-point temperature to 1100 K at pressures up to 800 MPa," *Journal of Physical and Chemical Reference Data*, vol. 25, no. 6, pp. 1509–1596, 1996.
- [23] W. Wagner, J. R. Cooper, A. Dittmann et al., "The IAPWS industrial formulation 1997 for the thermodynamic properties

- of water and steam,” *Journal of Engineering for Gas Turbines and Power*, vol. 122, no. 1, pp. 150–185, 2000.
- [24] K. Hooman and H. Gurgenci, “Effects of temperature-dependent viscosity on Bénard convection in a porous medium using a non-Darcy model,” *International Journal of Heat and Mass Transfer*, vol. 51, no. 5-6, pp. 1139–1149, 2008.
- [25] P. Forooghi, R. Xu, P. X. Jiang, and K. Hooman, “Numerical simulation of convective heat transfer for supercritical CO<sub>2</sub> in vertical pipes using V2F turbulence model,” in *Proceedings of the 18th Australasian Fluid Mechanics Conference (AFMC '12)*, P. A. Brandner and B. W. Pearce, Eds., Launceston, Australia, December 2012.
- [26] P. Forooghi and K. Hooman, “Effect of buoyancy on turbulent convection heat transfer in corrugated channels—a numerical study,” *International Journal of Heat and Mass Transfer*, vol. 64, pp. 850–862, 2013.
- [27] P. Forooghi and K. Hooman, “Numerical study of turbulent convection in inclined pipes with significant buoyancy influence,” *International Journal of Heat and Mass Transfer*, vol. 61, no. 1, pp. 310–322, 2013.
- [28] P. Forooghi and K. Hooman, “Experimental analysis of heat transfer of supercritical fluids in plate heat exchangers,” *International Journal of Heat and Mass Transfer*, vol. 74, pp. 448–459, 2014.

## Research Article

# Working Characteristics of Variable Intake Valve in Compressed Air Engine

**Qihui Yu, Yan Shi, and Maolin Cai**

*School of Automation Science and Electrical Engineering, Beihang University, Beijing 100191, China*

Correspondence should be addressed to Yan Shi; [yesoyou@gmail.com](mailto:yesoyou@gmail.com)

Received 25 July 2014; Revised 28 August 2014; Accepted 31 August 2014; Published 14 October 2014

Academic Editor: Arash Karimipour

Copyright © 2014 Qihui Yu et al. This is an open access article distributed under the Creative Commons Attribution License, which permits unrestricted use, distribution, and reproduction in any medium, provided the original work is properly cited.

A new camless compressed air engine is proposed, which can make the compressed air energy reasonably distributed. Through analysis of the camless compressed air engine, a mathematical model of the working processes was set up. Using the software MATLAB/Simulink for simulation, the pressure, temperature, and air mass of the cylinder were obtained. In order to verify the accuracy of the mathematical model, the experiments were conducted. Moreover, performance analysis was introduced to design compressed air engine. Results show that, firstly, the simulation results have good consistency with the experimental results. Secondly, under different intake pressures, the highest output power is obtained when the crank speed reaches 500 rpm, which also provides the maximum output torque. Finally, higher energy utilization efficiency can be obtained at the lower speed, intake pressure, and valve duration angle. This research can refer to the design of the camless valve of compressed air engine.

## 1. Introduction

Environmental issues such as fog, haze, greenhouse effect, and acid rains have been widely concerning. Burning of fossil fuels in internal combustion engines (ICE) for transportation is the major source of environmental issues [1–3]. New energy sources such as wind, solar energy, compressed air which can replace the fossil fuel are an obvious solution to solve environment issues [4]. With respect to environmental protection, the issue of energy expenditure has been emphasized [5]. Some scholars believe traditional automobiles will be replaced by new energy vehicles in the future. So far, there are some new energy vehicles, namely, electric vehicles, hybrid electric vehicles, compressed air engines (CAE), and so on. The CAE is the typical product of zero-pollution vehicles, which has been studied by many scholars and institutions [6].

To ensure smooth running and fast response, the flow of air is controlled by a simple cam mechanism in many CAE systems [7–9]. Conventional mechanical valve trains generally use valve timings and lifts which are fixed depending upon cam mechanism design. The lack of flexibility of camshaft based valve trains to vary timing, duration, and lift

of intake valves is one of the disadvantages [10]. Because the CAE does mechanical work by expanding compressed air, the flow of compressed air must be controlled to improve energy efficiency. It is obvious that the cam mechanism is difficult to meet the demand. In order to optimize energy efficiency, the variable intake valve techniques have been used in the CAE [11].

The variable intake valve techniques have the potential to be widely used in internal combustion engines to reduce energy losses and fuel consumption [12–17]. Previous studies have mainly focused on simulations and system integrations based on cam mechanism valve. Few studies have been reported about the variable intake valve investigations in CAE.

This paper focuses on the influences on the performance of the CAE by the variable intake valve lift and duration. Thus, detailed mathematical models to describe the working process are built and verified by experiments. This paper is organized as follows. In Section 2, detailed mathematical models are discussed. In Section 3, simulation and real experiments results are obtained and compared to verify the accuracy of the theoretical models. In Section 4,

the influences on the performance of the CAE by the lift and duration of the variable intake valve are analyzed. Finally, conclusions are presented in Section 5.

## 2. Theoretical Analysis

To understand the working process of the CAE, we need to study the in-cylinder process, which is illustrated in Figure 1. The gas tank provides energy source. The intake pressure is regulated by pressure control unit. Air flow is controlled by solenoid valve. There are mainly three components: the cylinder, the valves, and the tank. In the following, we build these models based on thermodynamics and piston kinematics. For a single-stage piston-type CAE, compressed air enters the cylinder through the intake valve and the piston is pushed by compressed air. Then the intake valve closed after a specific crank angle, while the compressed air continues to push the piston down and output work. When the piston reaches the bottom dead center (BDC), the exhaust valve opens so that the air with residual pressure discharges. The piston moves from the BDC to the top dead center (TDC); the CAE completes a work cycle.

**2.1. Valve Flow.** Because the throttling effect from the intake or exhaust valve accounts for energy losses, valve flow is critical to the CAE. Valve flow is considered as one-dimensional isentropic flow [18, 19].

If  $p_d/p_u > b$ , the mass flow rate is given by

$$G = Ap_u \sqrt{\frac{2k}{(k-1)R\theta_u} \left[ \left( \frac{p_d}{p_u} \right)^{2/k} - \left( \frac{p_d}{p_u} \right)^{(k+1)/k} \right]}. \quad (1)$$

If  $p_d/p_u \leq b$ , the flow is choked, and the mass flow rate is given by

$$G = Ap_u \sqrt{\frac{k}{R\theta_u} \left( \frac{2}{k+1} \right)^{(k+1)/(k-1)}}, \quad (2)$$

where  $b = (2/k + 1)^{k/k-1}$  is upstream stagnation sound speed.

The valve flow area is represented by  $A$ , which can be expressed by the following equation:

$$A = C_d A_v. \quad (3)$$

The relationship between the valve flow area and the valve lift is defined by the following equation:

$$A_v = a L_v. \quad (4)$$

The scale factor “ $a$ ” is defined by

$$a = \frac{A_{vm}}{IVL}, \quad (5)$$

where  $A_{vm}$  is the maximum valve flow area.

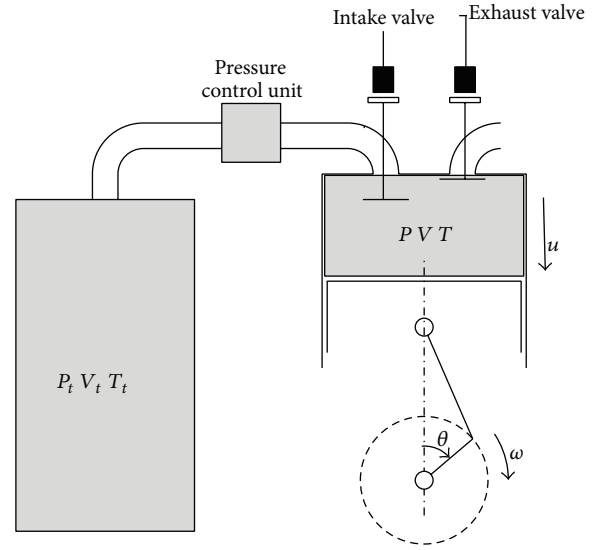


FIGURE 1: Cylinder-tank model.

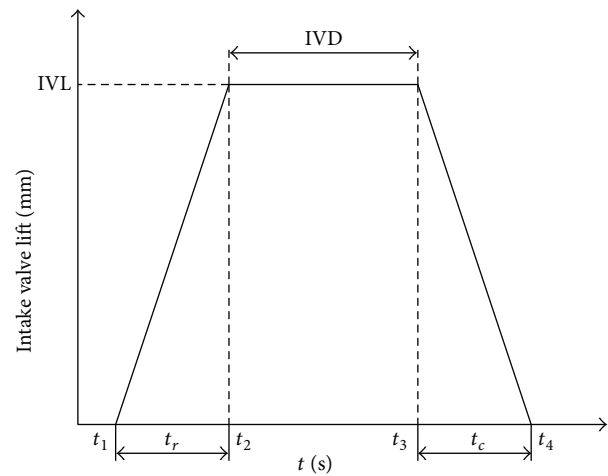


FIGURE 2: Valve lift profile.

We can characterize the camless valve motion by angle (or opening) IVO, maximum lift IVL, and duration IVD of each intake valve. For simplicity, the camless intake and exhaust valve lift profile model is presented by the following equations:

$$L_v = \begin{cases} s_r (t - t_1) & t \geq t_1, t < t_2 \\ IVL & t \geq t_2, t < t_3 \\ IVL - s_c (t - t_3) & t \geq t_3, t < t_4 \\ 0 & \text{otherwise,} \end{cases} \quad (6)$$

where

$$\begin{aligned} t_1 &= t_{IVO}, & t_2 &= t_1 + t_r, \\ t_3 &= t_2 + t_{IVD}, & t_4 &= t_3 + t_c. \end{aligned} \quad (7)$$

$s_r$  and  $s_c$  are fixed in the time domain. A coordinate transformation to crank angle domain results in different valve profiles at different engine speeds. The valve lift profile is shown in Figure 2.

**2.2. In-Cylinder Process.** The cylinder content is energy exchange process. The pressure and temperature of compressed air inside the cylinder are calculated by a global energy balance:

$$\frac{dU}{dt} = \frac{dq}{dt} + \frac{dm_i}{dt}h_i - \frac{dW}{dt} - \frac{dm_e}{dt}h_e, \quad (8)$$

where  $dU/dt$  is the rate of the internal energy of the air inside the cylinder,  $dq/dt$  is the rate of heat transferred from the cylinder wall to the cylinder contents, and  $dW/dt$  is the rate of work done by the open system (which is equal to  $pdV/dt$ ).

The internal energy of the air can be expressed as

$$\frac{dU}{dt} = \frac{d(mu)}{dt} = m \frac{du}{dt} + u \frac{dm}{dt}, \quad (9)$$

where  $u = C_v\theta$ ,  $m = m_i - m_e$ .

Substituting (9) into (8) yields

$$\frac{d\theta}{dt} = \frac{1}{mC_v} \left[ \frac{dq}{dt} + h_iG_i - h_eG_e - p \frac{dV}{dt} - uG \right], \quad (10)$$

where  $G_i = dm_i/dt$ ,  $G_e = dm_e/dt$ ,  $G = dm/dt$ .

The rate of the pressure change inside the cylinder is obtained by the ideal gas law:

$$p \frac{dV}{dt} + V \frac{dp}{dt} = mR \frac{d\theta}{dt} + R\theta \frac{dm}{dt}. \quad (11)$$

**2.3. Heat Transfer.** In order to evaluate the instantaneous heat interaction between the cylinder content, the heat transfer coefficient  $K_w$  must be defined. According to literature [20], assuming that the gas velocity is proportional to the average piston speed  $U_p$ , the heat transfer coefficient  $K_w$  can be expressed with the following equation:

$$K_w = (0.1129) d^{-0.2} p^{0.8} U_p^{0.8} \theta^{-0.594}. \quad (12)$$

The average piston speed can be expressed by the following equation:

$$U_p = \frac{S \cdot n}{30}. \quad (13)$$

The corresponding heat transfer is

$$\frac{dq}{dt} = K_w A_w (\theta_w - \theta), \quad (14)$$

where the total surface area  $A_w$  can be expressed with crank angle as follows:

$$A_w(\varphi) = \frac{\pi}{2} D^2 + \frac{\pi}{2} DS \times \left[ 1 - \cos \varphi + \frac{1}{\lambda} \left( 1 - \sqrt{1 - \lambda^2 \sin^2(\varphi)} \right) \right]. \quad (15)$$

TABLE 1: Initial value of the parameters.

Parameter	value
$D$ (m)	0.05
$S$ (m)	0.052
IVO (deg)	0
IVD (deg)	130
EVO (deg)	180
EVC (deg)	360
$p_s$ (bar)	2.5
$b$	0.41
$C_m$	2.3
$\lambda$	0.263
$n$ (rpm)	500
$t_r$ (s)	0.02
$C_d$	0.8

**2.4. Piston Ring Friction.** The differential element of friction work  $\delta W_f$  for the compression ring can be expressed as

$$\delta W_f = \mu_r p \pi D d_r \delta S, \quad (16)$$

where  $\delta S$  is piston stroke through which this force acts.

This expression is integrated over a complete engine cycle to account for the work lost to friction, which is then subtracted from the net cycle work.

### 3. Simulation and Experimental Validation

**3.1. Simulation of the CAE.** The working characteristics of the CAE are determined by the theoretical analysis mentioned in Section 2. The nonlinear and coupled differential equations are modelling in MATLAB/Simulink. Table 1 shows the initial values of the parameters.

Figures 3(a), 3(b), and 3(c) show the simulation results. The air pressure of the cylinder is shown in Figure 3(a), the air temperature of the cylinder is plotted against the crank angle in Figure 3(b), and Figure 3(c) depicts the air mass flow of the cylinder curve.

As shown in Figure 3, the pressure, temperature, and the mass inside the cylinder of the CAE change periodically. The intake valve opens when the piston reaches the TDC; compressed air from high pressure tank rapidly flows into the cylinder. The pressure inside the cylinder rapidly increases to the intake pressure. Meanwhile, the mass and temperature inside the cylinder increase. When the mass flow rate is less than the rate of cylinder volume, the pressure of the cylinder drops dramatically. Meanwhile, the compressed air inside the cylinder expands and leads to the temperature of the cylinder drop from its peak.

Compressed air no longer flows into the cylinder, when the intake valve is closed. At this time, the mass flow of air drops to zero. The piston is pushed to the BDC depending on compressed air inside the cylinder expansion. The temperature and pressure inside the cylinder drop dramatically.

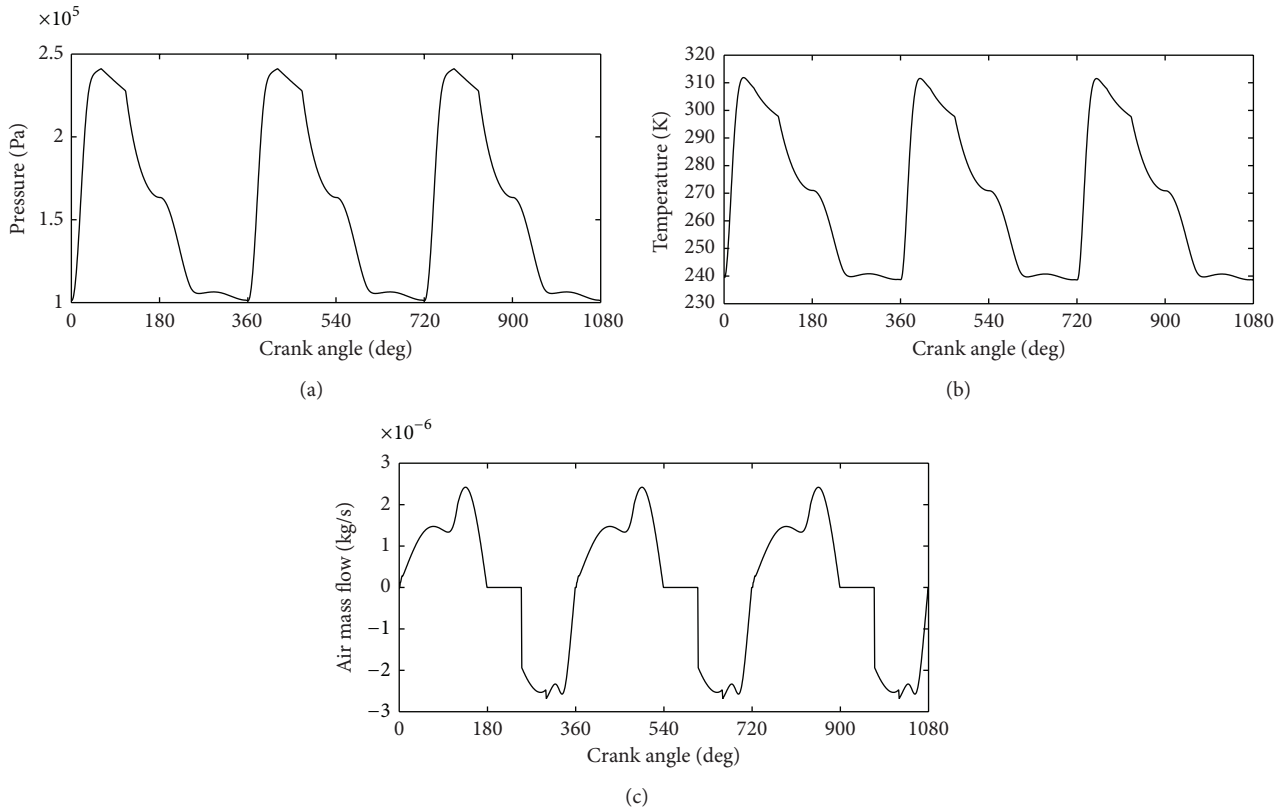


FIGURE 3: Pressure curve, temperature curve, and mass curve of the cylinder.

The exhaust valve opens when the piston reaches the BDC. The residual compressed inside the cylinder is discharged, and the mass inside the cylinder decreases from its top. Meanwhile, the temperature and pressure inside the cylinder drop to their bottoms.

The above process is repeated and mechanical power can be output continuously.

According to Figure 3(b), the temperature of the cylinder reaches 240 K which may experience icing, so heat exchange must be used.

**3.2. Experimental Verification.** The experiments were conducted to verify the accuracy of the mathematical model. The experimental apparatus is shown in Figure 4, which consists of a high pressure tank, a regulator (IR3020-03BC), a low pressure tank, a throttle valve (AS3001F), two port solenoid valves, a refit engine with basic parameters shown in Table 2, a data acquisition card (PCI1711) by Advantech, an absolute angular displacement sensor, and program logic controller (PLC) by Siemens. In the experiment, a 4-stroke gasoline engine was reformed to a compressed air engine by the intake port and exhaust port solenoid valve. The engine specifications are shown in Table 2.

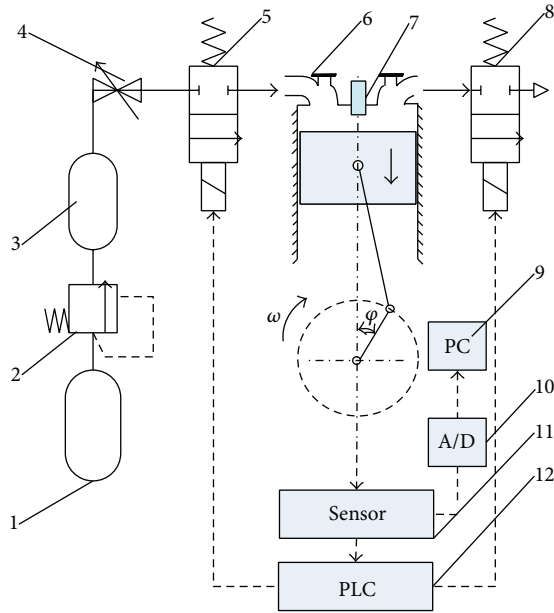
In this experiment, firstly, the compressed air source worked and the outlet pressure of the regulator was set to the fixed value. Secondly, the low pressure tank maintained the pressure after a period of time, then adjust throttle valve which can let compressed air exhausted steadily from the

TABLE 2: Engine specifications.

Engine model	DJ139FMA
Engine type	Single cylinder, 4-stroke, spark-ignited, air-cooled engine
Cylinder stroke/bore	50/52 mm
Displacement volume	100 cm <sup>3</sup>

tank. The intake port and the exhaust port solenoid valves were controlled by PLC with shaft angle which was detected by absolute value of the angular sensor. The intake port solenoid valve opened when the piston reached the TDC and closed completely at a crank angle. Then, compressed air inside the cylinder expands. During this process, the exhaust port solenoid stayed closed, and the piston was pushed from the TDC toward the BDC by the incoming compressed air, producing the power stroke. The exhaust solenoid valve opened when the piston reaches the BDC. During the process, the intake solenoid valve remained closed. The compressed air inside the cylinder was discharged from the cylinder, and the piston moved from the BDC towards the TDC. The crank angle was measured by absolute value of the angular displacement sensor. The last stage was data acquisition and storage.

The testing rig is built as shown in Figure 5. The main parameters of the cylinder are presented in Table 2.



- |                      |                            |
|----------------------|----------------------------|
| (1) Tank             | (7) Pressure sensor        |
| (2) Regulator        | (8) Solenoid valve         |
| (3) Tank             | (9) Computer               |
| (4) Throttle valve   | (10) Data acquisition card |
| (5) Solenoid valve   | (11) Angle sensor          |
| (6) Air power engine | (12) PLC                   |

FIGURE 4: Configuration of experimental apparatus.



FIGURE 5: The experiment of air powered engine.

As shown in Figure 6, the simulation curve trend is consistent with the experimental curve trend, and the mathematical model above can be verified. However, there are three differences between the simulation results and the experimental results: (1) the maximum pressure is different; (2) the experimental curve is backward offset to simulation curve; (3) the experiment exhaust pressure value is greater than the simulation exhaust pressure value.

The main reasons for the differences are summarized as follows. Considering the small effective flowing area in the intake solenoid, the throttling effect will be quite evident. Meanwhile, each solenoid valve experiences delay in motion, but the delay time is different under different situation.

In this paper, the simulation is based on the assumption that the delay time is constant for simplicity. Therefore, the experiment pressure curve is backward offset to simulation curve. And when the exhaust air mass flow is less than the rate of cylinder volume, the pressure inside the cylinder will increase during exhaust process.

Experiment and simulation curves of output torque are shown in Figure 7. It is obvious that the experimental and simulation curves have similar trends. Both output torque curves decrease when the rotate speed increased. But throttling loss is not considered in the simulation process, so the output torque in the simulation is greater than the experiment value at different crank speeds. It is obvious that the differences between experimental and numerical results are increased with the crank speed increasing. That is because the bearings friction torque, auxiliaries, and gears torque losses are not considered in the numerical calculated. These torques will increase along with the increase of the crank speed.

#### 4. Performance Analysis

Energy efficiency evaluation criterion to ICE is not suitable but not for the CAE. In this section, a new energy efficiency evaluation, namely, the air power, is briefly introduced to evaluate the energy efficiency of the CAE.

The air power is expressed using the available energy [21], which is expressed as

$$P = p_a Q_a \left[ \ln \frac{p_s}{p_a} + \frac{k}{k-1} \left( \frac{\theta_s - \theta_a}{\theta_a} - \ln \frac{\theta_s}{\theta_a} \right) \right], \quad (17)$$

where  $Q_a$  is the volume of air at the standard state.

The energy efficiency can be expressed by

$$\eta = \frac{P}{P_m}, \quad (18)$$

where

$$P_m = \frac{IT \cdot n}{9550}, \quad (19)$$

where IT indicates torque.

The indicated torque can be expressed by

$$IT = \frac{\int p dV}{2\pi}. \quad (20)$$

From the previous discussion, the performance of CAE can be obtained in different intake pressure, IVD, and IVL. The initial values of the parameters are shown in Table 1. Intake pressure, IVD, and IVL can be changed for comparison while all the other parameters are kept constant.

Figures 8(a) and 8(b) show the power and torque output from the CAE at various supplied pressures. The highest power output of 0.3345 kW is obtained at 7 bar and 500 rpm. The highest torque output of 8.4727 Nm is obtained at 7 bar and 300 rpm. The highest supplied pressure will obtain the highest torque and power output.

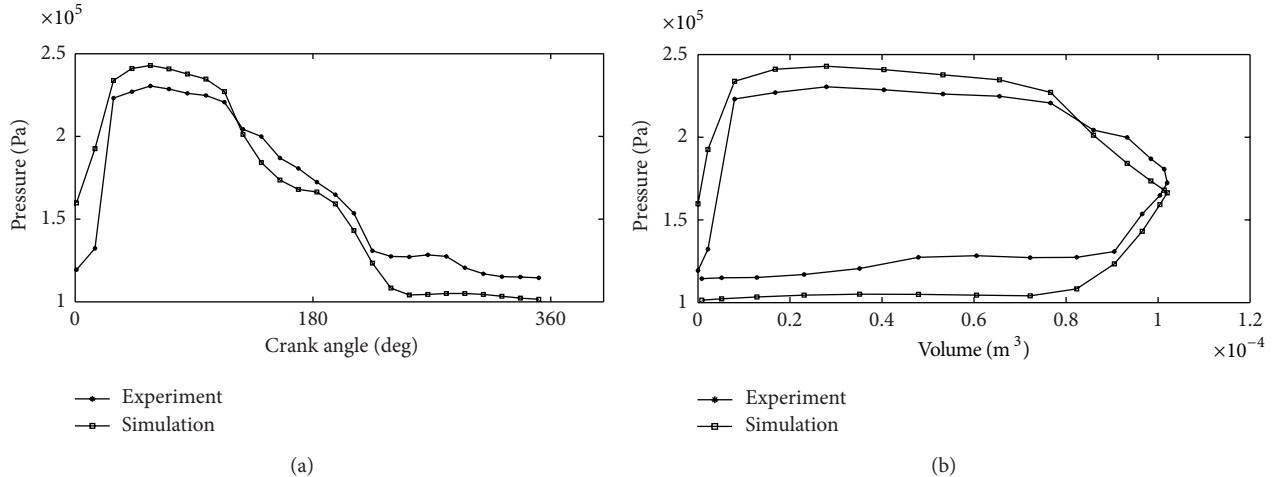


FIGURE 6: Experimental and simulation curves of cylinder pressure.

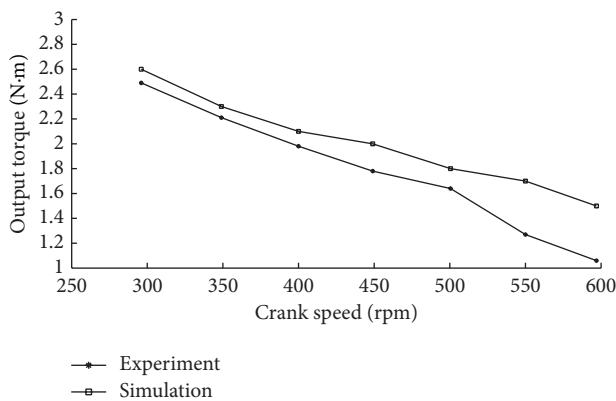


FIGURE 7: Experiment and simulation curves of output torque.

The energy efficiencies under various intake pressures and crank speeds are shown in Figure 8(c). The lowest crank speed leads to the highest energy efficiency. And the lowest air pressure provides the highest efficiency.

It is clear that increasing supply pressure is beneficial to output more power and torque. However, the method will reduce energy efficiency.

Figure 9 shows the performance of the CAE in various IVD angles at 5 bar intake pressure.

The power and torque output from the CAE are obtained by simulation at various IVD angles, as shown in Figures 9(a) and 9(b). The highest power output is obtained at 500 rpm in any IVD angle. The output torque increases with the IVD. The output power and torque are equal in different IVD angle at 500 rpm. The energy efficiency would decrease with the IVD and can be expressed in Figure 9(c). But when IVD is equal to 20 deg, the efficiency will drop at crank speed of 100 rpm. That is because the more the compressed air enters into CAE at the lowest crank speed, the higher the pressure exhausts are.

Figure 10 shows the performance of the CAE in various IVD at 5 bar intake pressure.

The power and torque output from the CAE are obtained by simulation at various IVD, as shown in Figures 10(a) and 10(b). The output power increases with the crank speed. But when crank speed is lower than 400 rpm, the output power has little change at various IVD. That is because in low crank speed the air flow mass is almost stable with different IVD. Meanwhile, at the beginning, the output torque increases with the increase of the crank speed and reaches its peaks at different crank speeds and IVD. The energy efficiency would decrease with the crank speed and large IVD is beneficial to improve the energy efficiency which can be expressed in Figure 10(c). Throttling effect will decrease in large IVD.

## 5. Conclusions

In this paper, the mathematical model was built. Simulation and experimental studies on the CAE were done, and the conclusions are summarized as follows.

- (1) Compressed air pressure inside the cylinder and output torque have the same changing tendency in both simulation curve and experimental curve.
- (2) The highest power output is obtained at 500 rpm, and the highest torque output is obtained at 300 rpm at different intake pressures and different IVD angles.
- (3) When crank speed is higher than 200 rpm, higher energy utilization efficiency can be obtained at the lower speed, intake pressure, and IVD.
- (4) The output torque increases with the increase of the crank speed and reaches its peaks at different crank speeds and IVD. And large IVD is beneficial to improve the energy efficiency.

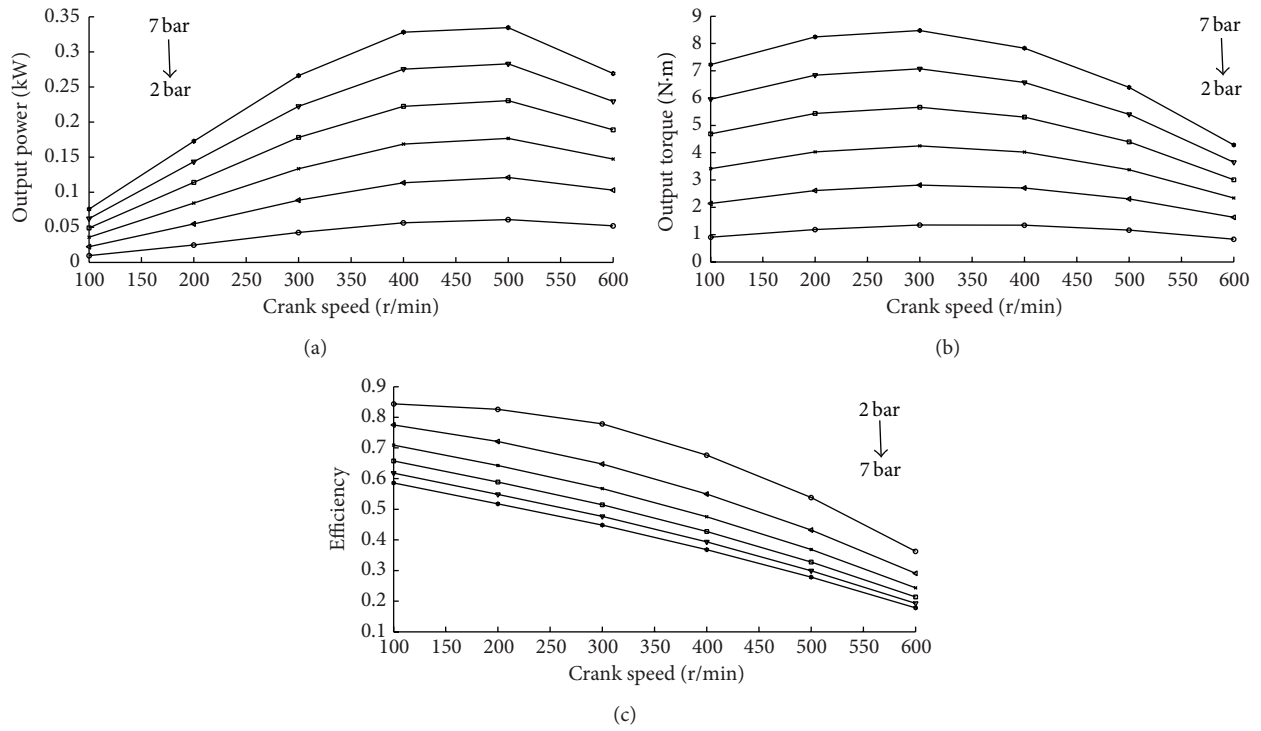


FIGURE 8: The relationship of intake pressure and performance of CAE.

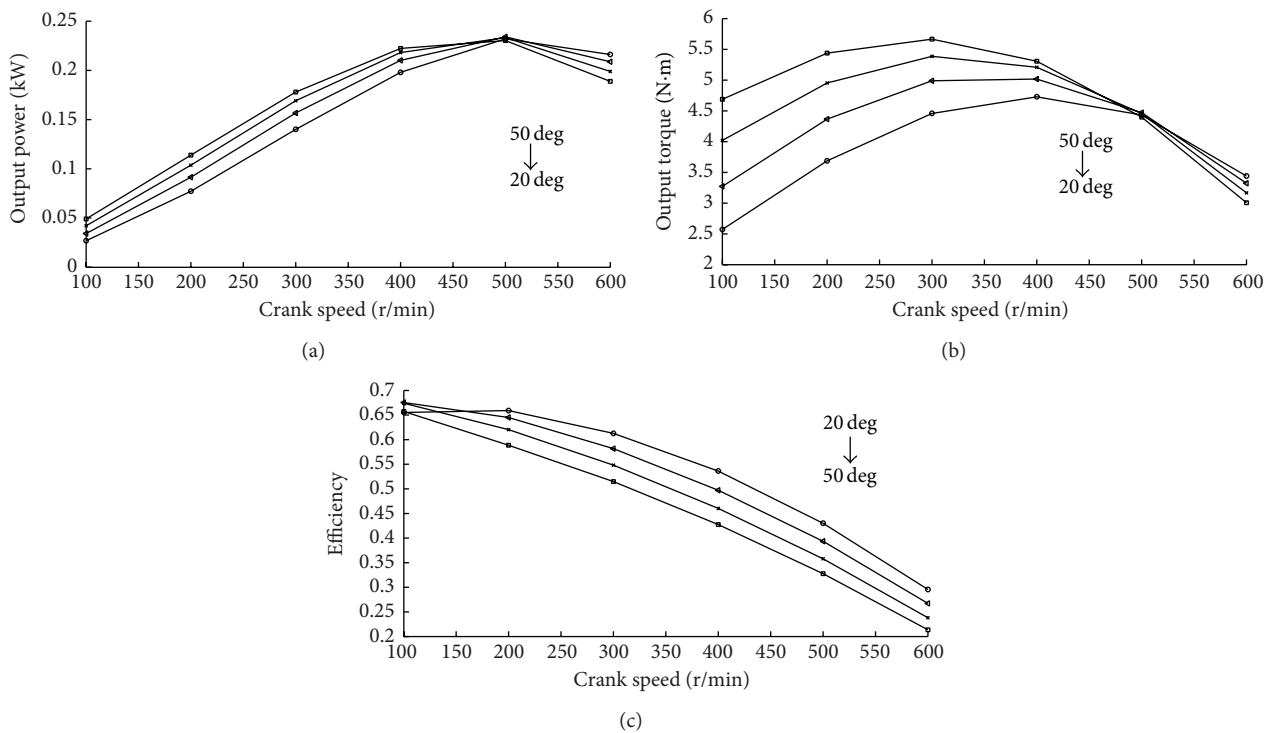


FIGURE 9: The relationship of IVD and performance of CAE.

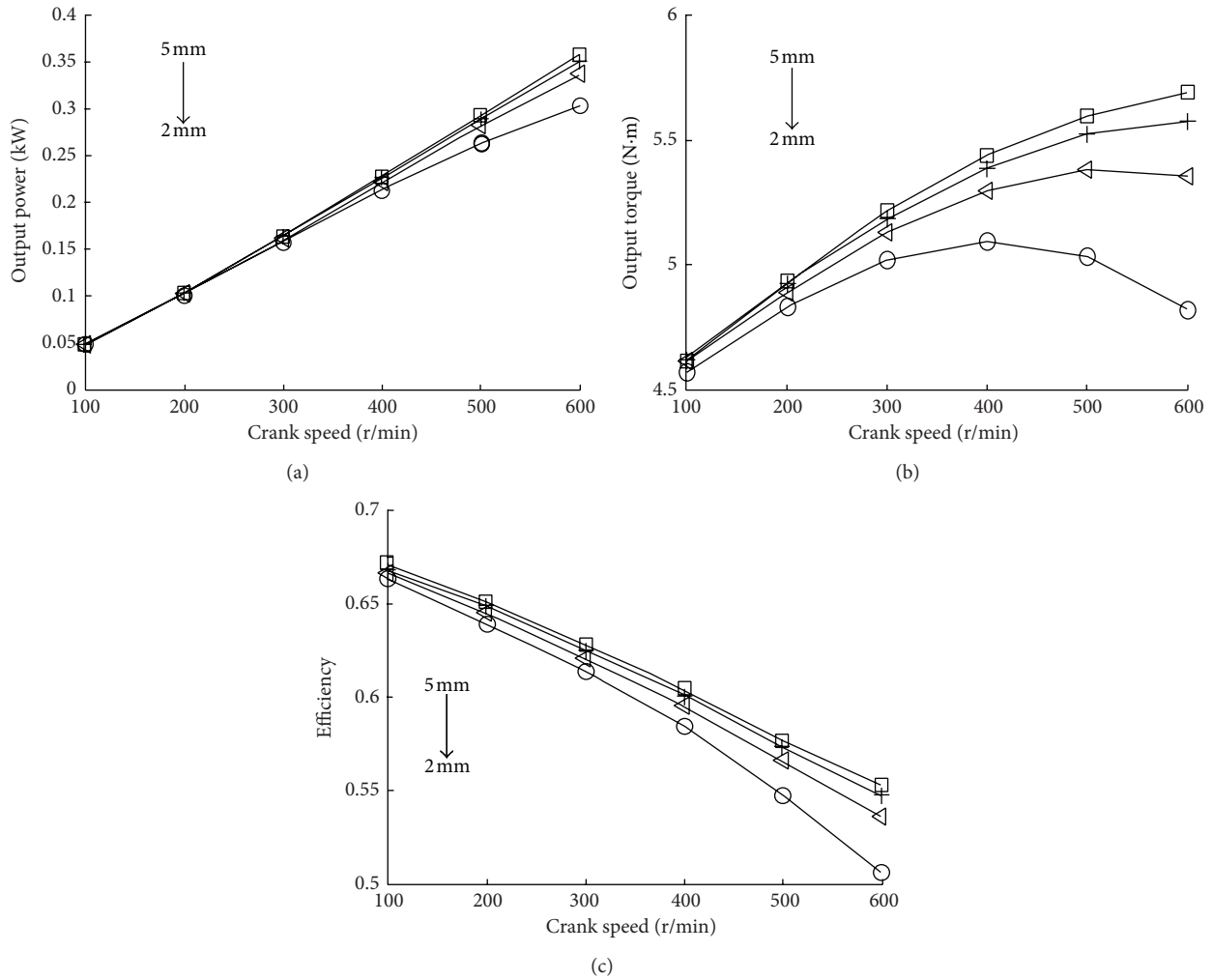


FIGURE 10: The relationship of IVL and performance of CAE.

## Nomenclature

$A$ : Area ( $\text{m}^2$ )  
 $b$ : Critical pressure ratio  
 $C_v$ : Specific heat at constant volume ( $\text{J}/(\text{kg}\cdot\text{K})$ )  
 $C_p$ : Specific heat at constant pressure ( $\text{J}/(\text{kg}\cdot\text{K})$ )  
 $C_d$ : The valve discharge coefficient  
 $D$ : Piston diameter (m)  
 $E$ : Thermodynamic internal energy (J)  
 $G$ : Air mass flow ( $\text{kg}/\text{s}$ )  
 $h$ : The enthalpies of air ( $\text{W}/(\text{m}^2\cdot\text{K})$ )  
 $\text{IVO}$ : Valve lift opening angle ( $^\circ\text{CA}$ )  
 $\text{IVL}$ : Valve maximum lift (m)  
 $\text{IVD}$ : Valve duration angle ( $^\circ\text{CA}$ )  
 $K_w$ : Heat transfer coefficient  
 $k$ : Specific heat ratio  
 $L$ : Valve lift (m)  
 $m$ : Air mass (kg)  
 $n$ : Engine speed (rpm)  
 $p$ : Pressure (Pa)

$q$ : Heat exchange (J)  
 $Q$ : The volume of air ( $\text{m}^3/\text{s}$ )  
 $R$ : Gas constant ( $\text{J}/(\text{kg}\cdot\text{K})$ )  
 $S$ : Piston stroke (m)  
 $s_r$ : Intake valve opening inclination  
 $s_c$ : Intake valve closing inclination  
 $t$ : Time (s)  
 $t_r$ : The time for intake valve to reach maximum lift (s)  
 $t_s$ : The time for intake valve from maximum lift to closing (s)  
 $U$ : The internal energy of the air (J)  
 $u$ : Velocity (m/s)  
 $V$ : Volume ( $\text{m}^3$ )  
 $W$ : Energy (J)  
 $\varphi$ : Crank angle (rad)  
 $\mu_r$ : The sliding friction coefficient  
 $\eta$ : Efficiency  
 $\omega$ : Crank speed (rad/s)  
 $\theta$ : Temperature (K).

### Subscripts

*a*: Atmosphere  
*d*: Downstream side  
*i*: Entering  
*e*: Leaving  
 IVO: Redundant use of opening  
 IVD: Duration of intake valve opening  
*o*: Valve  
*s*: Supply of CAE  
*t*: Tank  
*u*: Upstream side  
*v*: Valve.

### Conflict of Interests

The authors declare that there is no conflict of interests regarding the publication of this paper.

### References

- [1] H. Chen, Y. Ding, Y. Li, X. Zhang, and C. Tan, "Air fuelled zero emission road transportation: a comparative study," *Applied Energy*, vol. 88, no. 1, pp. 337–342, 2011.
- [2] B. R. Singh and O. Singh, "A study of performance output of a multivane air engine applying optimal injection and vane angles," *International Journal of Rotating Machinery*, vol. 2012, Article ID 578745, 10 pages, 2012.
- [3] T. N. Veziroglu and S. Sahin, "21st Century's energy: hydrogen energy system," *Energy Conversion and Management*, vol. 49, no. 7, pp. 1820–1831, 2008.
- [4] K. Morita, "Automotive power source in 21st century," *JSAE Review*, vol. 24, no. 1, pp. 3–7, 2003.
- [5] K. T. Chau and Y. S. Wong, "Overview of power management in hybrid electric vehicles," *Energy Conversion and Management*, vol. 43, no. 15, pp. 1953–1968, 2002.
- [6] C. A. Ordóñez, "Liquid nitrogen fueled, closed Brayton cycle cryogenic heat engine," *Energy Conversion and Management*, vol. 41, no. 4, pp. 331–341, 2000.
- [7] C.-Y. Huang, C.-K. Hu, C.-J. Yu, and C.-K. Sung, "Experimental investigation on the performance of a compressed-air driven piston engine," *Energies*, vol. 6, no. 3, pp. 1731–1745, 2013.
- [8] A. N. Da, T. Jian, and C.-J. Zuo, "Designing and experiment of a compressed-air engine," *Journal of Heifei University of Technology*, vol. 28, no. 6, pp. 612–615, 2005.
- [9] S. Trajkovic, P. Tunestal, and B. Johansson, "Investigation of different valve geometries and valve timing strategies and their effect on regenerative efficiency for a pneumatic hybrid with variable valve actuation," *SAE International*, 2008.
- [10] S. A. G. M. Saied, S. A. Jazayeri, and A. H. Shamekhi, "Modeling of variable intake valve timing in SI engine," in *Proceedings of the Spring Technical Conference of the ASME Internal Combustion Engine Division (ICES '06)*, pp. 789–803, May 2006.
- [11] M. H. Christopher and D. Lee, "Block: compressed air engine," U.S. Patent 8667787, 2014.
- [12] R. Kumar and A. K. Dixit, "Combustion and emission characteristics of variable compression ignition engine fueled with *Jatropha curcas* ethyl ester blends at different compression ratio," *Journal of Renewable Energy*, vol. 2014, Article ID 872923, 12 pages, 2014.
- [13] M. Izadi Najafabadi and N. Abdul Aziz, "Homogeneous charge compression ignition combustion: challenges and proposed solutions," *Journal of Combustion*, vol. 2013, Article ID 783789, 14 pages, 2013.
- [14] E. Sher and T. Bar-Kohany, "Optimization of variable valve timing for maximizing performance of an unthrottled SI engine—a theoretical study," *Energy*, vol. 27, no. 8, pp. 757–775, 2002.
- [15] M. Gölcü, Y. Sekmen, P. Erduranli, and M. S. Salman, "Artificial neural-network based modeling of variable valve-timing in a spark-ignition engine," *Applied Energy*, vol. 81, no. 2, pp. 187–197, 2005.
- [16] G. Fontana and E. Galloni, "Variable valve timing for fuel economy improvement in a small spark-ignition engine," *Applied Energy*, vol. 86, no. 1, pp. 96–105, 2009.
- [17] A.-F. M. Mahrous, A. Potrzebowski, M. L. Wyszynski, H. M. Xu, A. Tsolakis, and P. Luszcz, "A modelling study into the effects of variable valve timing on the gas exchange process and performance of a 4-valve DI homogeneous charge compression ignition (HCCI) engine," *Energy Conversion and Management*, vol. 50, no. 2, pp. 393–398, 2009.
- [18] Y. Shi and M. Cai, "Working characteristics of two kinds of air-driven boosters," *Energy Conversion and Management*, vol. 52, no. 12, pp. 3399–3407, 2011.
- [19] X. Wang, T.-C. Tsao, C. Tai, H. Kang, and P. N. Blumberg, "Modeling of compressed air hybrid operation for a heavy duty diesel engine," in *Proceedings of the Spring Technical Conference of the ASME Internal Combustion Engine Division*, pp. 173–186, April 2008.
- [20] U. Bossel, "Thermodynamic analysis of compressed air vehicle propulsion," *Journal of KONES, Internal Combustion Engines*, vol. 12, pp. 3–4, 2005.
- [21] M. Cai, K. Kawashima, and T. Kagawa, "Power assessment of flowing compressed air," *Journal of Fluids Engineering, Transactions of the ASME*, vol. 128, no. 2, pp. 402–405, 2006.

## Research Article

# Investigation of Micro- and Nanosized Particle Erosion in a 90° Pipe Bend Using a Two-Phase Discrete Phase Model

M. R. Safaei,<sup>1</sup> O. Mahian,<sup>2</sup> F. Garoosi,<sup>3</sup> K. Hooman,<sup>4</sup> A. Karimipour,<sup>5</sup>  
S. N. Kazi,<sup>1</sup> and S. Gharekhani<sup>1</sup>

<sup>1</sup> Department of Mechanical Engineering, Faculty of Engineering, University of Malaya, 50603 Kuala Lumpur, Malaysia

<sup>2</sup> Department of Mechanical Engineering, Faculty of Engineering, Ferdowsi University of Mashhad, Mashhad, Iran

<sup>3</sup> Department of Mechanical Engineering, University of Semnan, Semnan, Iran

<sup>4</sup> School of Mechanical and Mining Engineering, The University of Queensland, St Lucia, Brisbane, QLD 4072, Australia

<sup>5</sup> Department of Mechanical Engineering, Najafabad Branch, Islamic Azad University, Isfahan, Iran

Correspondence should be addressed to S. N. Kazi; [salimnewaz@um.edu.my](mailto:salimnewaz@um.edu.my)

Received 14 July 2014; Accepted 22 July 2014; Published 14 October 2014

Academic Editor: Marjan Goodarzi

Copyright © 2014 M. R. Safaei et al. This is an open access article distributed under the Creative Commons Attribution License, which permits unrestricted use, distribution, and reproduction in any medium, provided the original work is properly cited.

This paper addresses erosion prediction in 3-D, 90° elbow for two-phase (solid and liquid) turbulent flow with low volume fraction of copper. For a range of particle sizes from 10 nm to 100 microns and particle volume fractions from 0.00 to 0.04, the simulations were performed for the velocity range of 5–20 m/s. The 3-D governing differential equations were discretized using finite volume method. The influences of size and concentration of micro- and nanoparticles, shear forces, and turbulence on erosion behavior of fluid flow were studied. The model predictions are compared with the earlier studies and a good agreement is found. The results indicate that the erosion rate is directly dependent on particles' size and volume fraction as well as flow velocity. It has been observed that the maximum pressure has direct relationship with the particle volume fraction and velocity but has a reverse relationship with the particle diameter. It also has been noted that there is a threshold velocity as well as a threshold particle size, beyond which significant erosion effects kick in. The average friction factor is independent of the particle size and volume fraction at a given fluid velocity but increases with the increase of inlet velocities.

## 1. Introduction

Erosion-corrosion, defined as the accelerated corrosion following the damage of surface films, is a common cause of failure in a large amount of power plant equipment like pipes, pumps, compressors, vessels, and turbines. It can often be assumed that corrosion is controlled by adjusting the mass transfer while erosion is under the flow of a particulate second phase. This is a credible assumption as corrosion films are brittle-like materials and therefore are eroded easily by impacting particles [1, 2]. This phenomenon has been investigated experimentally in a number of pioneering studies; see [3–7], for instance. Despite recent advances in computational techniques, erosion-corrosion process is yet to be fully resolved with reasonable accuracy. A multitude of reasons for this rather slow development of simulation

techniques applied to this problem can be mentioned. For modeling mass transfer near the solid boundaries, it is necessary to solve the governing equations across the mass transfer boundary layer. In aqueous flows this layer may be an order of magnitude shorter than the viscous sublayer. This requires fine meshes in the near-wall region. Utilizing fine near-wall grids with the support of appropriate near-wall turbulence models, the required mass transfer data for corrosive species can be evaluated [8].

Chen et al. [9] studied erosion prediction approach and its usage in oilfield fittings, especially 3-D elbows and plugged tees, using CFX which is a commercially available CFD package. They used RNG  $k$ - $\epsilon$  turbulence model along with DPM to track the particles. The results demonstrated that particle rebound and erosion profile have the most significant roles in particles motion inside oilfield geometries. The

comparisons also indicated that CFD predictions for erosion are in good agreement with experimental data.

An erosion prediction approach for specifying wear profiles for a 2-D jet impingement test has been developed by Gnanavelu et al. [10]. This prediction model was according to material wear data achieved from laboratory experiments and CFD modeling. They found an appropriate relationship between predicted and experimental data. Although they found that due to some assumptions about particle size and shape, material hardening, numerical errors, and so forth, some essential errors always exist in the calculation.

Mohyaladin et al. [11] have used three methods (empirical, semiempirical, and computational fluid dynamics, i.e., CFD) to model 2-D sand erosion in a pipe, a problem with significant practical application in oil and gas industry. The results of this study have shown that the direct impingement model (semiempirical model) agrees with the results achieved from the discrete phase model (DPM) implemented in CFD whereas the CFD results dramatically underpredict the empirical ones.

Particles, in an erosion problem, can be external to fluid flow; that is, they may be removals from the walls or upstream flow processes. There are, on the other hand, cases where particles are internal to flow like nanofluids. Nanofluids are synthesized by adding highly conductive solid materials to the base fluid, such as water, ethylene glycol, and oil, all with relatively lower thermal conductivity, usually to improve the heat transfer performance of the mixture (compared to that of the base fluid) [12–14]. The idea of adding microparticles to base fluids was presented decades ago; however, microsized particles have the tendency to settle in the suspension, thereby potentially leading to adverse effects. Use of nanofluids, with nanosized particles suspended in the base fluids, would mitigate the issues of fouling and pipe blockings. In addition, the presence of microsized abrasive solid materials will cause erosion and corrosion of pipes and damage pumps and other devices [15].

Routbort et al. [16] have investigated the effect of nanoparticles on erosion in a car radiator. The nanofluids in their study were 1–4% (volume) silicon carbide (SiC) in water as well as 0.1–0.8% (volume) cupric oxide (CuO) in ethylene glycol. Experiments were conducted in the range of 4 m/s–10 m/s (for velocities) and at 90°–30° impact angles. The radiator was made of Al3003 typical radiator material. In their tests, they did not observe any erosion using nanofluids. Just in one case (Cu/water nanofluid, velocity of 9.6 m/s and impact angle of 90°) the galvanic pitting (and not erosion) was observed. In this case, the material loss rate due to galvanic pitting was around  $4 \times 10^{-2} \mu\text{m/hr}$  which indicated that the erosion had the least effect.

In a subsequent study, Routbort et al. [17] have studied the erosion of nanofluids on impeller of a cast aluminum car cooling system. They used 0.1–0.8% (volume) CuO in ethylene glycol and 0.5–4.0% (volume) SiC in water and in ethylene glycol/water (50%-50%) mixture as nanofluids. The experiments were conducted in the range of 2 m/s–10 m/s (for velocities) and at 90°–30° impact angles. The impeller was made of Al3003 material. Their study has shown no weight

loss measured after testing 2% (volume), 170 nm SiC/water for more than 700 hours at 8 m/s velocity, that is, no damage to the impeller of a commercial automobile water pump.

However, in their latest report, Routbort et al. [18] have found 0.65% erosion of impeller after hundreds of hours of pumping SiC/water and SiC/ethylene glycol-water (50/50 vol.%) nanofluids at high mass flow rates (20–28 L/min).

In view of the above, comprehensive analysis of nanofluids as erosive materials is yet missing in the literature [19, 20]. In particular, erosion of nanofluids in turbulent flow regime inside industrial fittings is not fully understood. Hence, the present study aims at investigating turbulent flow of dilute water/Cu and nanofluids in a 3-D 90° elbow using finite volume method with standard  $k$ - $\varepsilon$  turbulence and DPM. The simulation results for microsized particle flow regime are compared with those in the literature for validation purpose. Special attention was paid to micro- and nanosized copper particles of different solid volume fractions and Reynolds numbers in a commercial elbow.

## 2. Governing Equations of Turbulent Micro- and Nanofluids Erosion

The underlying physical assumption in this study is that the particles are carried by the flowing fluid. Therefore, continuity, momentum, DPM, and turbulent equations are used to analyze the flow. The spherical particles' velocity is assumed to be the same as those of flowing fluid. Assuming constant thermophysical properties for fluid and particles, the governing equations are as follows [21–23].

Continuity equation:

$$\frac{\partial}{\partial t} (\rho) + \nabla \cdot (\rho \vec{V}) = 0. \quad (1)$$

Momentum equation:

$$\frac{\partial}{\partial t} (\rho \vec{V}) + \nabla \cdot (\rho \vec{V} \vec{V}) = -\nabla P + \nabla \cdot [\mu (\nabla \vec{V} + \nabla \vec{V}^T)] + \rho g. \quad (2)$$

Standard  $k$ - $\varepsilon$  turbulence model is as follows.

Turbulent kinetic energy transport equation:

$$\frac{\partial (\rho k)}{\partial t} + \nabla \cdot (\rho \vec{V} k) = \nabla \cdot \left[ \left( \mu + \frac{\mu_t}{\sigma_k} \right) \nabla k \right] + G_k - \rho \varepsilon. \quad (3)$$

Dissipation of turbulent kinetic energy transport equation:

$$\begin{aligned} \frac{\partial (\rho \varepsilon)}{\partial t} + \nabla \cdot (\rho \vec{V} \varepsilon) \\ = \nabla \cdot \left[ \left( \mu + \frac{\mu_t}{\sigma_\varepsilon} \right) \nabla \varepsilon \right] + \frac{\varepsilon}{k} (C_{\varepsilon 1} G_k - \rho \varepsilon C_{\varepsilon 2}). \end{aligned} \quad (4)$$

The turbulent eddy viscosity obtained from Prandtl-Kolmogorov relation:

$$\mu_t = C_\mu \rho \frac{k^2}{\varepsilon}. \quad (5)$$

TABLE 1: Coefficients for standard  $k-\varepsilon$  turbulent model.

$C_\mu$	$\sigma_k$	$\sigma_\varepsilon$	$C_{\varepsilon 1}$	$C_{\varepsilon 2}$
0.09	1	1.3	1.44	1.92

The turbulence kinetic energy production of the mean velocity gradients,  $G_k$ , is given as:

$$G_k = \mu_t \nabla \vec{v} \cdot (\nabla \vec{v} + \nabla \vec{v}^T) - \frac{2}{3} \nabla \cdot \vec{v} (3\mu_t \nabla \cdot \vec{v} + \rho k). \quad (6)$$

The constants for the standard  $k-\varepsilon$  turbulence model in the above formula are represented in Table 1 [24, 25].

DPM is as follows:

$$m_p \frac{d\vec{v}_p}{dt} = \sum \vec{F}, \quad (7)$$

where  $\vec{F}$  is an external force acting on the particles which for fine particles with high density ratio (more than one) is drag and buoyancy forces [26].

Therefore, the equation of motion can be simplified to the following form:

$$\frac{d\vec{v}_p}{dt} = F_D (\vec{v} - \vec{v}_p) + \frac{g(\rho_p - \rho)}{\rho_g}, \quad (8)$$

where [27]

$$F_D = \left( \frac{18\mu}{\rho_p d_p^2} \right) \left( \frac{C_D \text{Re}_p}{24} \right), \quad (9)$$

wherein  $\text{Re}_p$  is the particle Reynolds number and is given as [28–30]

$$\text{Re}_p = \left( \frac{\rho d_p |\vec{v}_p - \vec{v}|}{\mu} \right). \quad (10)$$

The drag coefficient,  $C_D$ , as a function of the particle Reynolds number is defined by [31, 32]

$$C_D = \frac{24}{\text{Re}} \left( 1 + 11.2355 \text{Re}^{0.653} \right) + \frac{(-0.8271) \text{Re}}{8.8798 + \text{Re}}. \quad (11)$$

The solid particle erosion rates are defined as [33, 34]

$$R_{\text{erosion}} = \sum_{p=1}^N \left( \frac{\dot{m}_p C(d_p) f(\alpha) v^{b(v)}}{A_f} \right), \quad (12)$$

where  $C(d_p)$  is a function of particle diameter,  $f(\alpha)$  is a function of impact angle,  $\alpha$  is the angle between the particle trajectory and wall,  $v$  is the relative velocity among particles,  $b(v)$  is a function of relative velocity among particles, and  $A_f$  is the cell face area at the wall [33].

### 3. Boundary Conditions

Figure 1 illustrates the schematic of the problem which is analyzed in the present study. The boundary conditions are also indicated in this figure.

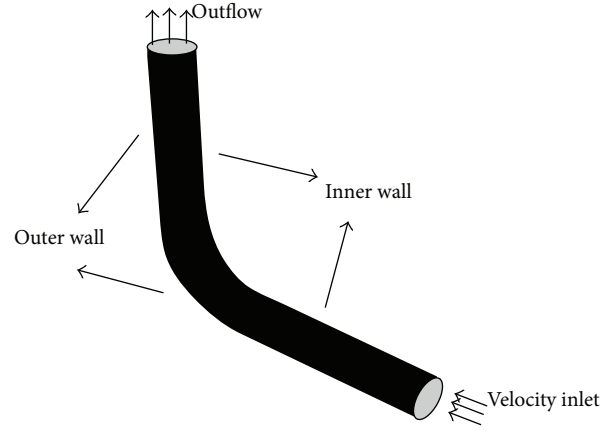


FIGURE 1: Schematic description of the pipe flow configuration with the elbow being considered for analysis.

TABLE 2: Point values for impact angle function [11].

Point	Angle	Value
1	0	0
2	20	0.8
3	30	1
4	45	0.5
5	90	0.4

### 4. Numerical Method

The FLUENT commercial code based on finite volume method which has been used in some previous works [21, 22, 35–37] was applied to solve the Reynolds averaged Navier-Stokes (RANS) equations. This method is based on a particular type of the residual weighting approach. In this approach, the computational zone is divided into finite control volumes as each node is covered by a control volume. Eventually, the differential equation is integrated on each finite volume [38–40].

Since in this study the particle volumetric loading ratio is below 10% (0%–4%), the DPM was applied for solving the diluted fluid-solid multiphase flow [41]. As such, the continuous phase, fluid, was simulated by utilizing the Eulerian approach whereas Lagrangian approach was used for modeling the particle phase. Standard wall functions were selected along with standard  $k-\varepsilon$  model described above.

The second-order upwind method [42–44] was chosen for the discretization of all terms, while the SIMPLEC algorithm (SIMPLE-Consistent) [15, 45, 46] was employed for pressure-velocity coupling. The impact angle function was specified utilizing a piecewise linear profile as per Table 2. The velocity exponent function and diameter function were fixed at 2.6 and  $1.8 \times 10^{-09}$ , respectively, following [11]. The solution was converged when the residuals for all the equations dropped below  $10^{-6}$  [38, 47].

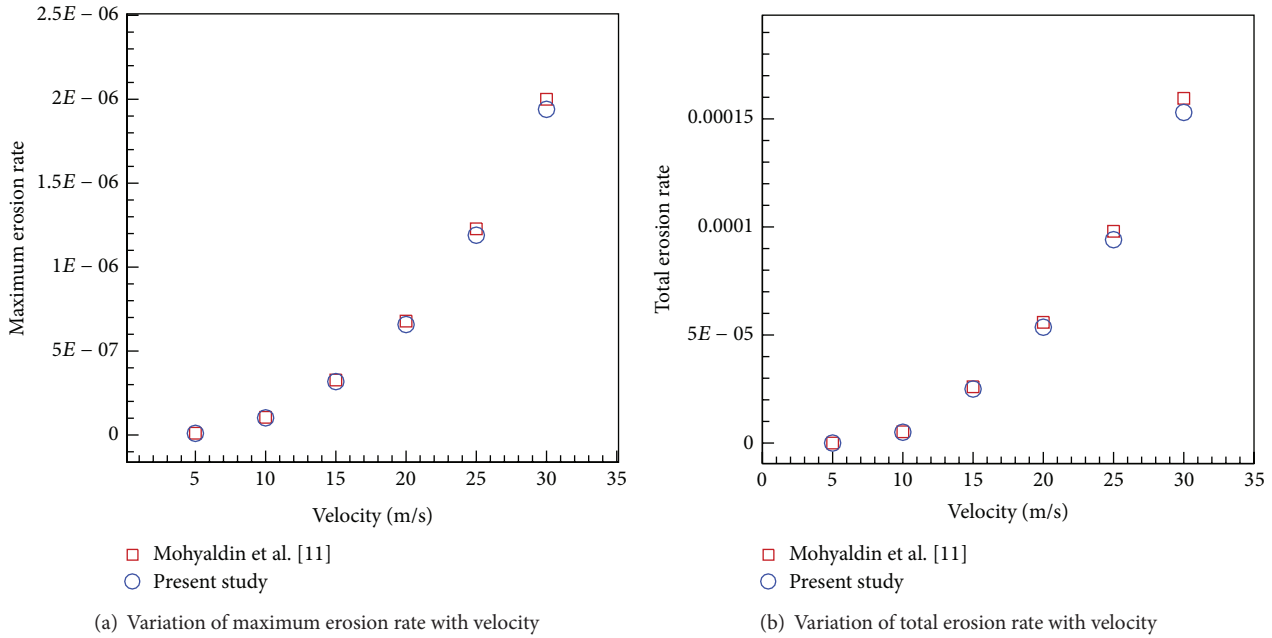


FIGURE 2: Comparison of total erosion rate and maximum erosion rate predicted here with those of [11].

### 5. Numerical Procedure Validation

5.1. *Validation with Numerical Study.* In order to verify the present simulation, the results from this work were compared with those of [11] where sand erosion in a 2-D elbow was simulated. The geometry was a 50 mm diameter elbow with two 100 mm straight pipes protruded from both sides. The two-phase (air/sand) dilute slurry flow with sand as the dispersed phase was injected at 0.000886 kg/s to the continuous phase, here air, with an inlet velocity of 20 m/s. The variations of total erosion rate and maximum erosion rate with velocity were compared with the results reported by Mohyaldin et al. [11], as shown in Figures 2(a) and 2(b), to observe an excellent agreement between the results.

5.2. *Validation with Experimental Study.* The numerical predictions based on our work were also compared with numerical and experimental results reported by Chen et al. [9] for erosion in elbows and plugged tees. Comparisons were performed for a 2.54 cm (diameter) elbow with a curvature ratio of 1.5 where sand particles of 150-micron diameter are injected at  $2.08 \times 10^{-4}$  kg/s over a range of air/sand velocities: 15.24, 30.48, and 45.72 m/s. The computed average mass loss for elbow was successfully compared with measurements reported in Chen et al. [9], as shown in Figure 3.

### 6. Grid Independence

The computational zone was discretized through structured, nonuniform hexahedral grid distributions. The refined grid was used at the vicinity of the walls where sharp gradients are expected. Several grid distributions were examined as Table 3 indicates. As seen, the effect of grid refinement beyond 61440

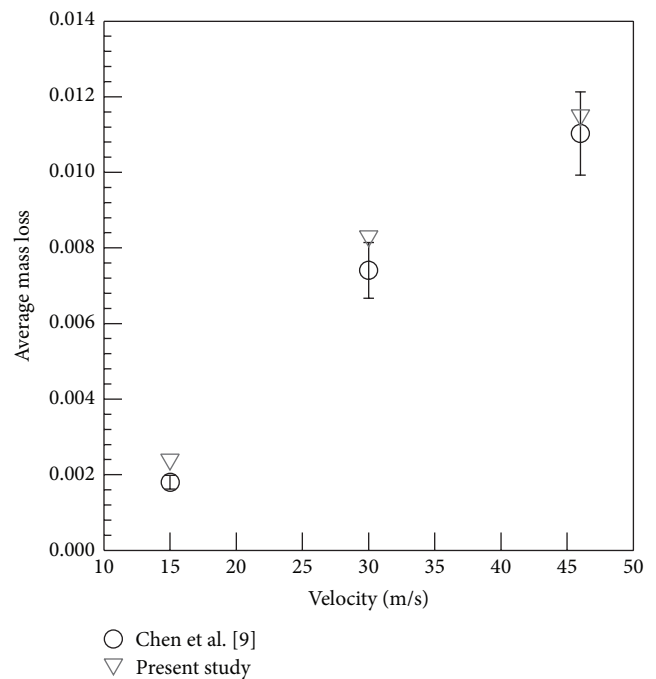


FIGURE 3: Comparison of average mass loss variations with previous work.

grids on the average erosion rate is insignificant implying grid independence of our results.

### 7. Results and Discussion

In this work, the turbulent fluid flow of water and copper micro- and nanoparticle suspensions through a 90° elbow has

TABLE 3: Grid independence tests.

Number of grids ( $V = 20 \text{ m/s}, \varphi = 2\%$ )	<b>30720</b>	<b>61440</b>	<b>122880</b>
Average erosion rate for $100 \mu\text{m}$ particles	$6.9523 \times 10^{-6}$	$6.7833 \times 10^{-6}$	$6.6965 \times 10^{-6}$
Number of grids ( $V = 20 \text{ m/s}, \varphi = 2\%$ )	<b>30720</b>	<b>61440</b>	<b>122880</b>
Average erosion rate for $10 \text{ nm}$ particles	$2.6789 \times 10^{-6}$	$2.5029 \times 10^{-6}$	$2.4351 \times 10^{-6}$
Number of grids ( $V = 20 \text{ m/s}, \varphi = 4\%$ )	<b>30720</b>	<b>61440</b>	<b>122880</b>
Average erosion rate for $100 \mu\text{m}$ particles	$1.5270 \times 10^{-5}$	$1.3857 \times 10^{-5}$	$1.2994 \times 10^{-5}$
Number of grids ( $V = 20 \text{ m/s}, \varphi = 4\%$ )	<b>30720</b>	<b>61440</b>	<b>122880</b>
Average erosion rate for $10 \text{ nm}$ particles	$4.3001 \times 10^{-6}$	$4.1646 \times 10^{-6}$	$4.0843 \times 10^{-6}$

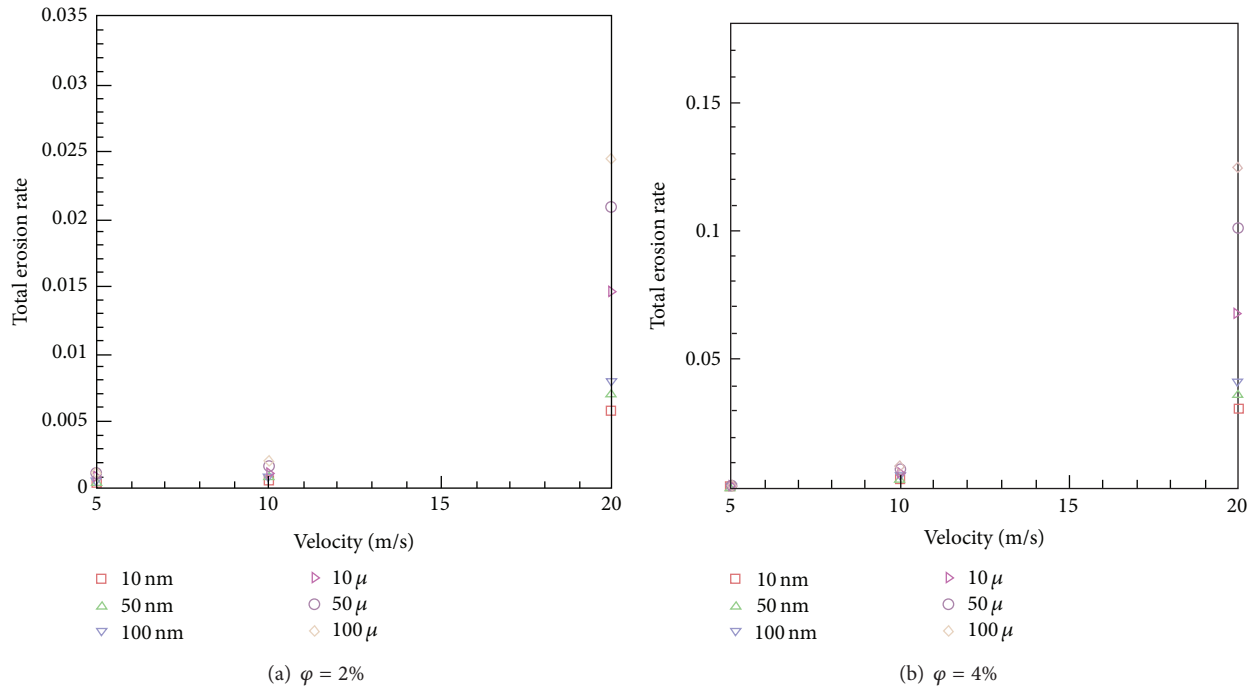


FIGURE 4: The variation of total erosion rate with velocity.

been investigated. The material of the 0.0032 m (1/8 inches) diameter elbow was aluminum (3003 Alloy). The length of the two attached pipe pieces at the beginning and the end of the elbow was 0.016 m (5/8 inches) long (5 times pipe diameter). The ratio of the bend radius to pipe inside diameter is equal to 1.5. Water was allowed to flow through the pipe at different velocities (5 m/s, 10 m/s, and 20 m/s). It was assumed that the solid particles are spherical and flow at the same velocity as that of water. Different particle diameters (10, 50, and 100 microns as well as 10, 50, and 100 nanometers) and particle volume fractions (2% and 4%) in the suspension were examined.

**7.1. The Influence of Velocity on Erosion Rate.** To investigate the impact of velocity on the maximum erosion rate and total erosion rate, several inlet velocities were simulated. The impact of inlet flow velocity on the total erosion rate is demonstrated in Figures 4(a) and 4(b) for different particle sizes. One notes that the total erosion rates are near zero for inlet velocity less than 5 m/s and particle volume fraction of

2%. For volume fraction of 4%, this quantity is still negligible for inlet velocity less than 5 m/s and particle diameters below 10 microns. This inlet velocity value of 5 m/s can be considered as a “threshold limit” for total erosion rate beyond which the total erosion rate rockets up with an increase in the inlet flow velocity for each particle diameter. These figures also indicate that, with the increase of particle volume fraction, the total erosion rate increases. The maximum of this erosion increase for  $\varphi = 4\%$  is around 4.9 times at  $V = 20 \text{ m/s}$  and  $d_p = 100 \text{ microns}$ , compared to that of  $\varphi = 2\%$ .

Similar trends are observed in Figures 5(a) and 5(b) for the maximum erosion rate at six various particle diameters. As seen, the maximum erosion rate is amplified with the particle diameter and velocity increment. This augmentation is negligible at velocities less than 5 m/s, but the difference between the values is more pronounced with an increase in the inlet velocity. Thus, when velocity is increased from 10 m/s to 20 m/s, the maximum erosion rate increases by about an order of magnitude, in fact, by around 7.5 times and 9 times at  $\varphi = 2\%$  and  $\varphi = 4\%$ , respectively.

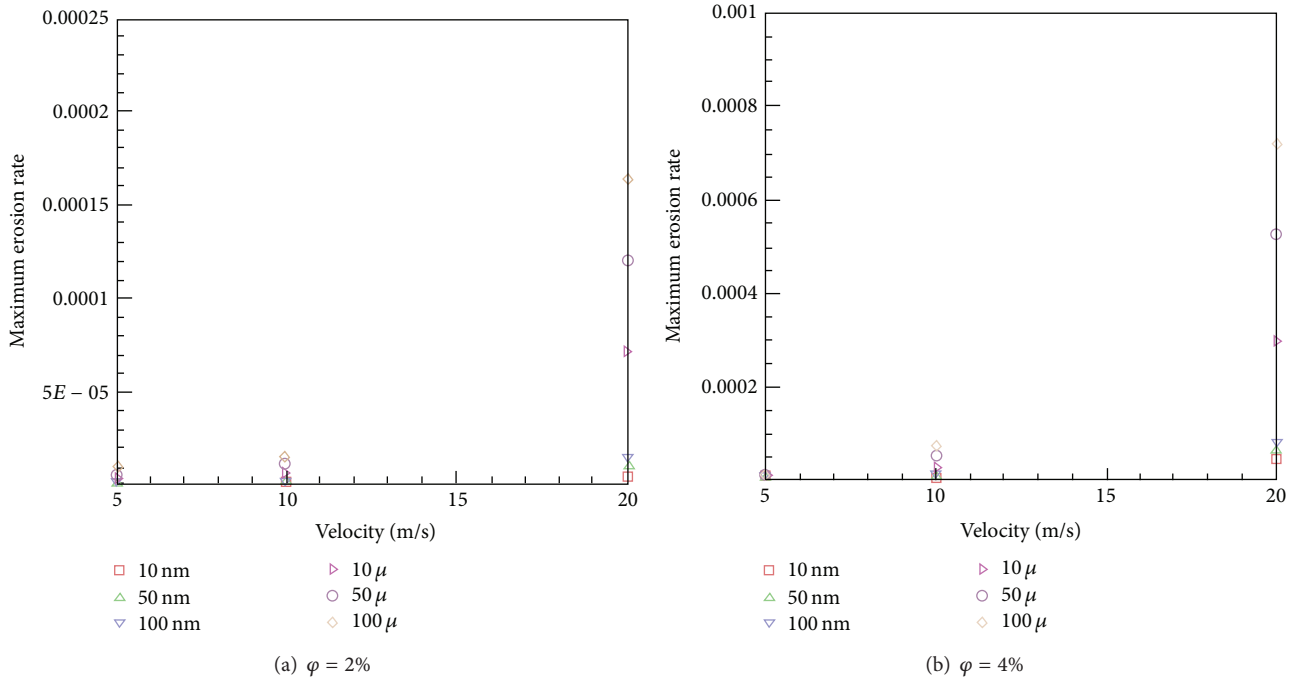


FIGURE 5: The variation of maximum erosion rate with velocity.

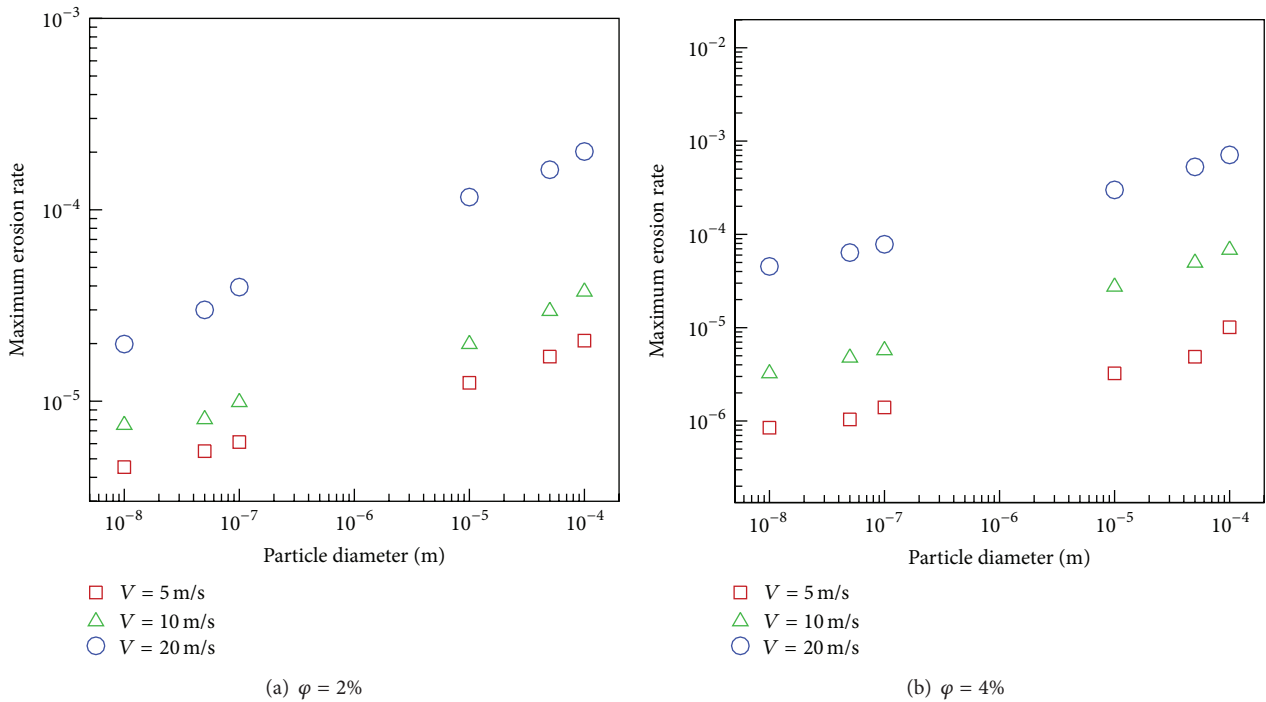


FIGURE 6: The variation of particle size with maximum erosion rate.

**7.2. The Effect of Particle Dimension on Erosion Rate.** It is significant to study the effect of particle diameter on fluid-solid interaction as particles' size in different systems varies to a large extent from nanometer to centimeter. The particle diameter has direct influence on the drag force and, therefore, affects the flow behavior. The influence of particle diameter

on maximum erosion rate, total erosion, pressure drop, and friction factor was studied by changing the particle diameter from 10 nm to 100  $\mu$ m.

The influence of particle size on the maximum erosion rate was represented in Figures 6(a) and 6(b). As seen, the maximum erosion rate is closely related to the fluid velocity

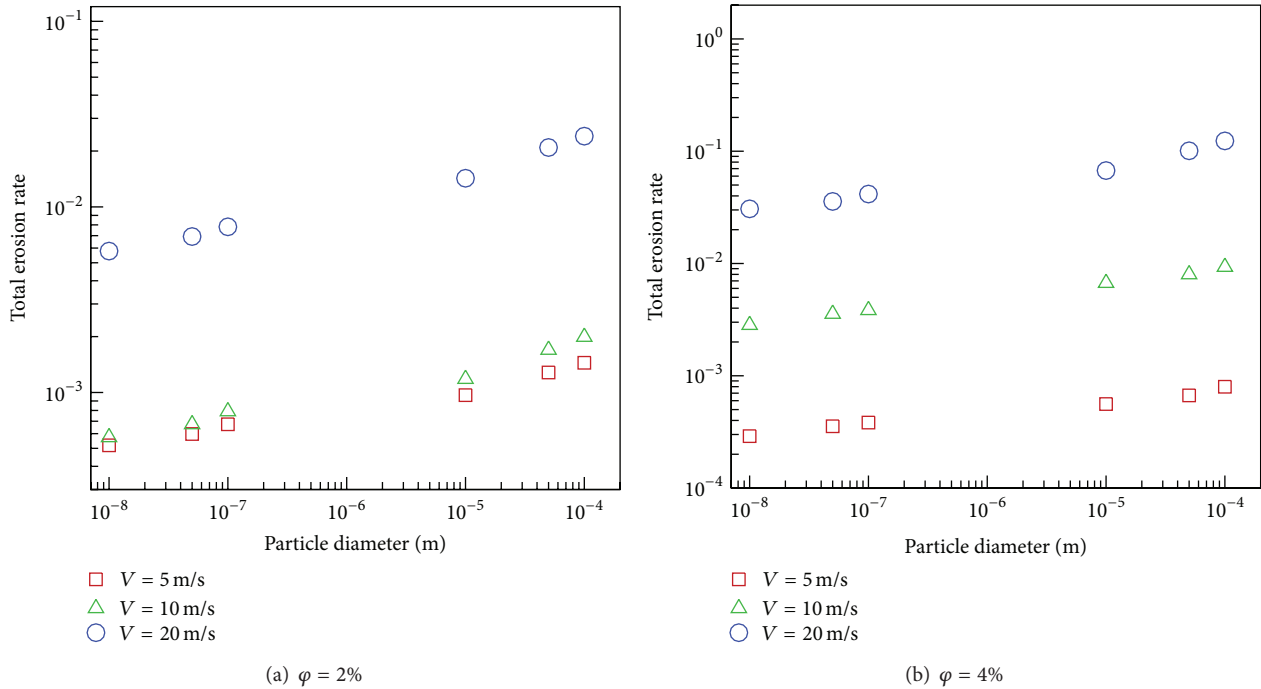


FIGURE 7: The variation of particle size with total erosion rate.

where a threshold velocity as well as a threshold particle size can be identified below which erosion is negligible. These figures also indicate that the rate of erosion augments linearly with particle diameter. One also notes that increasing the volume fraction of the particles, with other parameters fixed, will cause higher maximum erosion rate. The average of this increment is around 4.5 times.

Similar trends are observed in Figures 7(a) and 7(b) for total erosion rate where higher erosion rate is observed when the particle diameter and inlet fluid velocity are increased. This is expected as the particle impact velocity grows with the increase of the inlet flow velocity and particle size (see (12)). However, our numerical results can be used to quantify this increment. Note that the increase in the total erosion rate is around 8.5 times for the increase of velocity from 10 m/s to 20 m/s at  $\phi = 2\%$  and 9.5 times at  $\phi = 4\%$ . The influence of volume fraction enhancement on total erosion rate is also around 8 times when the volume fraction is increased from 2% to 4%.

The declining impact of particle size on the maximum pressure was shown in Figures 8(a) and 8(b). This can be attributed to the reduction in drag forces as a result of an increase in the particle size. Consequently, with the same particle volume fraction, particle numbers are lowered compared to the case with smaller particles. The figures also indicate that there is a direct relationship between the velocity and increase of maximum pressure. It is also clear from the figures that an increase in particle volume fraction leads to higher maximum pressure. As a result, the maximum pressure value is observed when 10 nm particles at 4% volume fraction flow with water at 20 m/s.

Interestingly, according to Figures 9(a) and 9(b), the average friction factor—which has been calculated based on Fanning equation—is insensitive to either the particle size or volume fraction. However, one observes that the average friction factor increases with inlet velocity unlike a single-phase flow.

Figure 10 illustrates the erosion contour inside the elbow for  $V = 20$  m/s, particle size = 100 microns, and the volume fractions of (Cu) 2%. As seen, the maximum erosion is observed near the midpoint, along the symmetry plane of the pipe bend, which is the location where velocity profiles begin an inverse behavior and the pressure is maximum.

Finally, for engineering applications and presentation of the physical influence of the parameters, the following single nonlinear correlation is derived from Figures 11(a) and 11(b) to estimate the average erosion rate as a function of particles' concentration, diameter, and inlet velocity, valid for the range of parameters in this work; that is,  $0.02 \leq \phi \leq 0.04$ ,  $5 \text{ m/s} \leq V \leq 20 \text{ m/s}$ , and  $10 \text{ nm} \leq d_p \leq 100 \text{ microns}$ . The average deviation of this correlation is 9.5%. Consider the following:

$$\begin{aligned} \text{Average erosion rate (AER)} \\ = 3.6667 \times 10^{-8} (\phi^{1.0024} V^{3.4953} d_p^{0.1399}). \end{aligned} \tag{13}$$

### 8. Conclusion

A numerical study of erosion in turbulent water-based/copper (Cu) micro- and nanosized fluid flow through a 90° elbow has been conducted. Different solid volume fractions, particle sizes, and velocities were considered along with

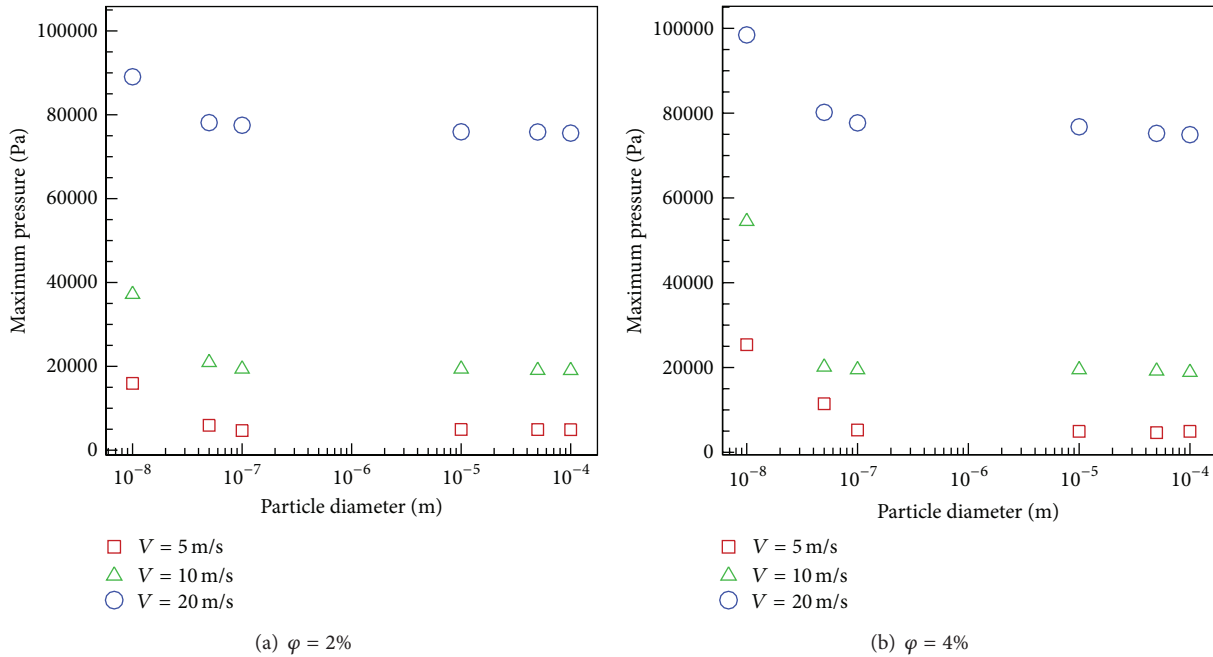


FIGURE 8: The variation of particle size with maximum pressure.

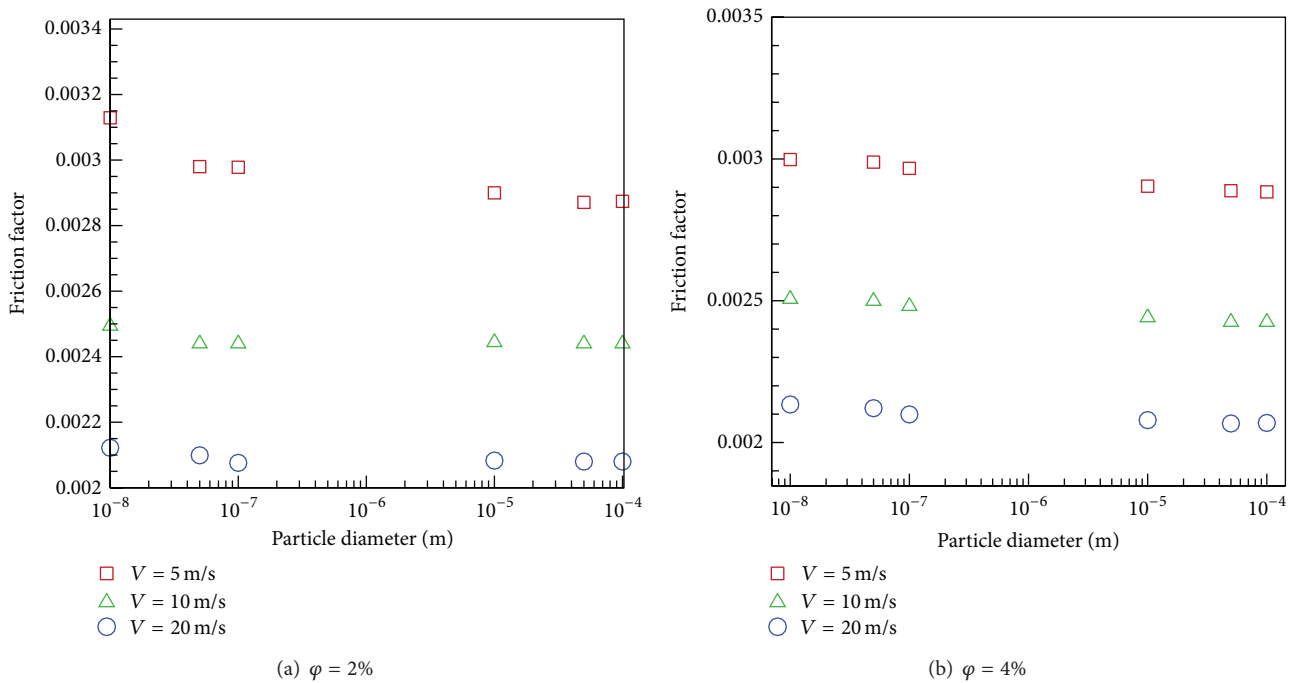


FIGURE 9: The variation of particle size with average friction factor.

the maximum erosion rate, total erosion rate, average erosion rate, friction factor, and maximum pressure.

The conclusions are summarized as follows.

(i) There is a threshold velocity as well as a threshold particle size, beyond which erosion is significant.

(ii) The maximum erosion rate, average erosion rate, and total erosion rate increase with particle diameter, volume fraction, and inlet fluid velocity.

(iii) Increase of the particle diameter decreases the maximum pressure.

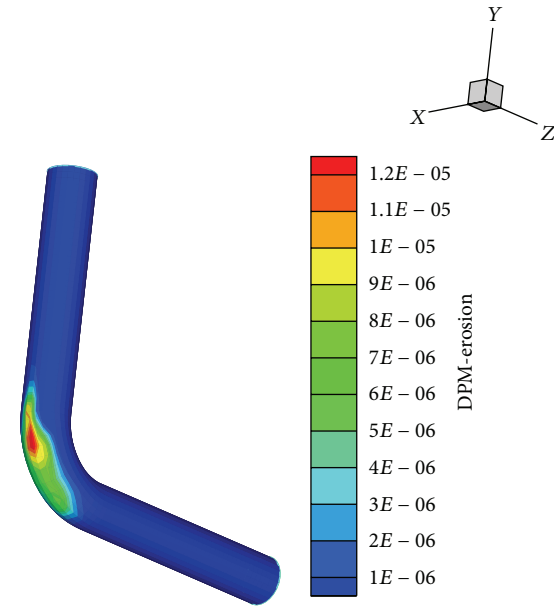


FIGURE 10: Erosion contour on the wall of the bend.

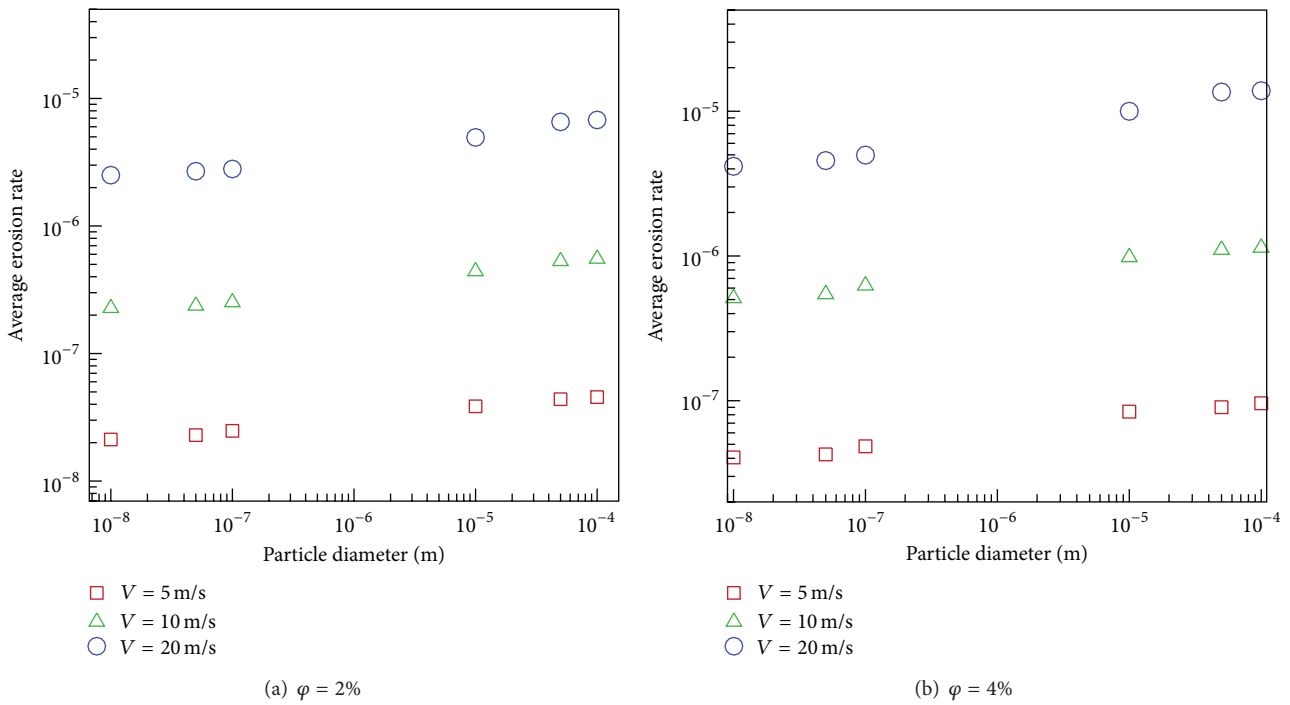


FIGURE 11: The variation of particle size with average erosion rate.

- (iv) An increase in particle volume fraction or velocity augments the maximum pressure.
- (v) The average friction factor does not depend on particle size and/or volume fraction for a given flow rate.

- (vi) With the increase of the inlet velocity, the average friction factor enhances.

The usage of nanofluids in heat transfer has an obvious benefit from the thermal efficiency point of view. Nonetheless, care

must be taken as depending on particle size, fluid velocity, particle shape, particle sedimentation, particle agglomeration, and surface erosion adverse effects can negate the benefits associated with heat transfer augmentation.

## Nomenclature

$x, y$ : Cartesian coordinates (m)  
 $d$ : Diameter (m)  
 $G_k$ : Generation of turbulent kinetic energy ( $\text{m}^2 \text{s}^{-2}$ )  
 $\vec{g}$ : Gravitational acceleration ( $\text{m s}^{-2}$ )  
 $m_p$ : Particle mass (kg)  
 $\vec{v}_p$ : Particle velocity ( $\text{m s}^{-1}$ )  
 $P$ : Pressure ( $\text{N m}^{-2}$ )  
 $Re$ : Reynolds number ( $V D \nu^{-1}$ )  
 $d_p$ : Solid particle diameter (m)  
 $t$ : Time (sec)  
 $k$ : Turbulence kinetic energy ( $\text{m}^2 \text{s}^{-2}$ )  
 $\vec{V}$ : Velocities vector ( $\text{m s}^{-1}$ ).

## Greek Symbols

$\rho$ : Density ( $\text{kg m}^{-3}$ )  
 $\varepsilon$ : Dissipation rate of turbulent kinetic energy ( $\text{m}^2 \text{s}^{-3}$ )  
 $\mu$ : Dynamic viscosity (Pa s)  
 $\sigma_k$ : Effective Prandtl number for  $k$   
 $\sigma_\varepsilon$ : Effective Prandtl number for  $\varepsilon$   
 $\nu$ : Kinematics viscosity ( $\text{m}^2 \text{s}^{-1}$ )  
 $\nu_t$ : Turbulence eddy viscosity ( $\text{m}^2 \text{s}^{-1}$ )  
 $\varphi$ : Volume fraction of particles.

## Subscripts

$D$ : Drag  
 $p$ : Particle  
 $t$ : Turbulent.

## Conflict of Interests

The corresponding author declares that there is no conflict of interests regarding the publication of this paper.

## Acknowledgments

The authors gratefully acknowledge the High Impact Research Grant UM.C/HIR/MOHE/ENG/45, UMRG Grant RP012D-13AET, and Faculty of Engineering, University of Malaya, Malaysia, for support in conducting this research work.

## References

- [1] A. Keating and S. Nesic, "Prediction of two-phase erosion-corrosion in bends," in *Proceedings of the 2nd International Conference on CFD in the Minerals and Process Industries (CSIRO '99)*, pp. 229–236, Melbourne, Australia, 1999.
- [2] S. Nešić, "Using computational fluid dynamics in combating erosion-corrosion," *Chemical Engineering Science*, vol. 61, no. 12, pp. 4086–4097, 2006.
- [3] J. Southard, R. A. Young, and C. D. Hollister, "Experimental erosion of calcareous ooze," *Journal of Geophysical Research*, vol. 76, no. 24, pp. 5903–5909, 1971.
- [4] P. Lonsdale and J. B. Southard, "Experimental erosion of North Pacific red clay," *Marine Geology*, vol. 17, no. 1, pp. M51–M60, 1974.
- [5] M. E. Gulden, "Correlation of experimental erosion data with elastic—plastic impact models," *Journal of the American Ceramic Society*, vol. 64, no. 3, pp. C59–C60, 1981.
- [6] R. A. Saravanan, M. K. Surappa, and B. N. Pramila Bai, "Erosion of A356 Al-SiCp composites due to multiple particle impact," *Wear*, vol. 202, no. 2, pp. 154–164, 1997.
- [7] G. T. Burstein and K. Sasaki, "Effect of impact angle on the slurry erosion-corrosion of 304L stainless steel," *Wear*, vol. 240, no. 1-2, pp. 80–94, 2000.
- [8] W. H. Ahmed, M. M. Bello, M. El Nakla, and A. Al Sarkhi, "Flow and mass transfer downstream of an orifice under flow accelerated corrosion conditions," *Nuclear Engineering and Design*, vol. 252, pp. 52–67, 2012.
- [9] X. Chen, B. S. McLaurry, and S. A. Shirazi, "Application and experimental validation of a computational fluid dynamics (CFD)-based erosion prediction model in elbows and plugged tees," *Computers and Fluids*, vol. 33, no. 10, pp. 1251–1272, 2004.
- [10] A. Gnanavelu, N. Kapur, A. Neville, J. F. Flores, and N. Ghorbani, "A numerical investigation of a geometry independent integrated method to predict erosion rates in slurry erosion," *Wear*, vol. 271, no. 5-6, pp. 712–719, 2011.
- [11] M. E. Mohyaldin, N. Elkhatib, and M. C. Ismail, "Evaluation of different modelling methods used for erosion prediction," in *Proceedings of the NACE Corrosion Changhai Conference & Expo*, pp. 1–19, Changhai, China, 2011.
- [12] M. H. Esfe, M. Akbari, D. Toghraie, A. Karimipour, and M. Afrand, "Effect of nanofluid variable properties on mixed convection flow and heat transfer in an inclined two-sided lid-driven cavity with sinusoidal heating on sidewalls," *Heat Transfer Research*, vol. 45, no. 5, pp. 409–432, 2014.
- [13] M. R. Safaei, H. Togun, K. Vafai, S. N. Kazi, and A. Badarudin, "Investigation of thermal conductivity and rheological properties of nanofluids containing graphene nanoplatelets," *Numerical Heat Transfer A*, vol. 66, no. 12, pp. 1321–1340, 2014.
- [14] H. Togun, M. R. Safaei, R. Sadri et al., "Numerical simulation of laminar to turbulent nanofluid flow and heat transfer over a backward-facing step," *Applied Mathematics and Computation*, vol. 239, pp. 153–170, 2014.
- [15] M. Goodarzi, M. R. Safaei, K. Vafai et al., "Investigation of nanofluid mixed convection in a shallow cavity using a two-phase mixture model," *International Journal of Thermal Sciences*, vol. 75, pp. 204–220, 2014.
- [16] J. Routbort, D. Singh, W. Yu et al., "Effects of nanofluids on heavy vehicle cooling systems," in *Proceedings of the VT Annual Merit Review Meeting*, pp. 1–16, Argonne National Laboratory, February 2008.
- [17] J. Routbort, D. Singh, E. Timofeeva, W. Yu, and R. Smith, *Erosion of Radiator Materials by Nanofluids*, Argonne National Laboratory, Vehicle Technologies—Annual Review, 2010.
- [18] J. Routbort, D. Singh, E. Timofeeva, W. Yu, and R. Smith, *Erosion of Radiator Materials by Nanofluids*, Vehicle Technologies—Annual Review, Argonne National Lab., 2011.

- [19] A. Karimipour, M. H. Esfe, M. R. Safaei, D. T. Semiromi, S. Jafari, and S. N. Kazi, "Mixed convection of copper-water nanofluid in a shallow inclined lid driven cavity using the lattice Boltzmann method," *Physica A: Statistical Mechanics and its Applications*, vol. 402, pp. 150–168, 2014.
- [20] M. H. Esfe, S. S. M. Esforjani, M. Akbari, and A. Karimipour, "Mixed-convection flow in a lid-driven square cavity filled with a nanofluid with variable properties: effect of the nanoparticle diameter and of the position of a hot obstacle," *Heat Transfer Research*, vol. 45, no. 6, pp. 563–578, 2014.
- [21] H. Badr, M. Habib, R. Ben-Mansour, and S. Said, "Effect of flow velocity and particle size on erosion in a pipe with sudden contraction," in *Proceedings of the 6th Saudi Engineering Conference*, vol. 5, pp. 79–88, KFUPM, Dhahran, Saudi Arabia, December 2002.
- [22] H. M. Badr, M. A. Habib, R. Ben-Mansour, and S. A. M. Said, "Numerical investigation of erosion threshold velocity in a pipe with sudden contraction," *Computers and Fluids*, vol. 34, no. 6, pp. 721–742, 2005.
- [23] Q. H. Mazumder, "Effect of liquid and gas velocities on magnitude and location of maximum erosion in U-bend," *Open Journal of Fluid Dynamics*, vol. 2, pp. 29–34, 2012.
- [24] M. R. Safaei, H. R. Goshayeshi, B. S. Razavi, and M. Goodarzi, "Numerical investigation of laminar and turbulent mixed convection in a shallow water-filled enclosure by various turbulence methods," *Scientific Research and Essays*, vol. 6, no. 22, pp. 4826–4838, 2011.
- [25] M. R. Safaei, Y. Maghmoumi, and A. Karimipour, "Numerical investigation of turbulence mixed convection heat transfer of water and drilling mud inside a square enclosure by finite volume method," in *Proceedings of the International Meeting on Advances in Thermofluids (IMAT '11)*, Melaka, Malaysia, October 2011.
- [26] E. Sistani, "PIV measurements around a rotating single gear partially submerged in oil within modelled SAAB gearbox," in *Diploma Work-Department of Applied Mechanics*, Chalmers University of Technology, Göteborg, Sweden, 2010.
- [27] M. A. Habib, R. Ben-Mansour, H. M. Badr, and M. E. Kabir, "Erosion and penetration rates of a pipe protruded in a sudden contraction," *Computers & Fluids*, vol. 37, no. 2, pp. 146–160, 2008.
- [28] V. Abdolkarimi and R. Mohammadikhah, "CFD modeling of particulates erosive effect on a commercial scale pipeline bend," *ISRN Chemical Engineering*, vol. 2013, Article ID 105912, 10 pages, 2013.
- [29] H. Zhu, H. Zhao, Q. Pan, and X. Li, "Coupling analysis of fluid-structure interaction and flow erosion of gas-solid flow in elbow pipe," *Advances in Mechanical Engineering*, vol. 2014, Article ID 815945, 10 pages, 2014.
- [30] M. G. Lipsett and V. Bhushan, "Modeling erosion wear rates in slurry flotation cells," *Journal of Failure Analysis and Prevention*, vol. 12, no. 1, pp. 51–65, 2012.
- [31] M. A. Habib, H. M. Badr, S. A. M. Said, R. Ben-Mansour, and S. S. Al-Anizi, "Solid-particle erosion in the tube end of the tube sheet of a shell-and-tube heat exchanger," *International Journal for Numerical Methods in Fluids*, vol. 50, no. 8, pp. 885–909, 2006.
- [32] H. Zhu, Y. Lin, G. Feng et al., "Numerical analysis of flow erosion on sand discharge pipe in nitrogen drilling," *Advances in Mechanical Engineering*, vol. 2013, Article ID 952652, 10 pages, 2013.
- [33] A. Campos-Amezcuca, A. Gallegos-Muñoz, C. Alejandro Romero, Z. Mazur-Czerwicz, and R. Campos-Amezcuca, "Numerical investigation of the solid particle erosion rate in a steam turbine nozzle," *Applied Thermal Engineering*, vol. 27, no. 14-15, pp. 2394–2403, 2007.
- [34] P. Frawley, J. Corish, A. Niven, and M. Geron, "Combination of CFD and DOE to analyse solid particle erosion in elbows," *International Journal of Computational Fluid Dynamics*, vol. 23, no. 5, pp. 411–426, 2009.
- [35] H. M. Badr, M. A. Habib, R. Ben-Mansour, S. A. M. Said, and S. S. Al-Anizi, "Erosion in the tube entrance region of an air-cooled heat exchanger," *International Journal of Impact Engineering*, vol. 32, no. 9, pp. 1440–1463, 2006.
- [36] M. A. Habib, H. M. Badr, R. Ben-Mansour, and M. E. Kabir, "Erosion rate correlations of a pipe protruded in an abrupt pipe contraction," *International Journal of Impact Engineering*, vol. 34, no. 8, pp. 1350–1369, 2007.
- [37] K. Sun, L. Lu, and H. Jin, "Modeling and numerical analysis of the solid particle erosion in curved ducts," *Abstract and Applied Analysis*, vol. 2013, Article ID 245074, 8 pages, 2013.
- [38] A. Karimipour, M. Afrand, M. Akbari, and M. Safaei, "Simulation of fluid flow and heat transfer in the inclined enclosure," *International Journal of Mechanical and Aerospace Engineering*, vol. 6, pp. 86–91, 2012.
- [39] S. V. Patankar, *Numerical Heat Transfer and Fluid Flow*, Taylor & Francis, 1980.
- [40] M. R. Safaei, B. Rahmanian, and M. Goodarzi, "Numerical study of laminar mixed convection heat transfer of power-law non-Newtonian fluids in square enclosures by finite volume method," *International Journal of Physical Sciences*, vol. 6, no. 33, pp. 7456–7470, 2011.
- [41] P. Xu, Z. Wu, A. S. Mujumdar, and B. Yu, "Innovative hydrocyclone inlet designs to reduce erosion-induced wear in mineral dewatering processes," *Drying Technology*, vol. 27, no. 2, pp. 201–211, 2009.
- [42] M. Goodarzi, M. R. Safaei, H. F. Oztop et al., "Numerical study of entropy generation due to coupled laminar and turbulent mixed convection and thermal radiation in an enclosure filled with a semitransparent medium," *The Scientific World Journal*, vol. 2014, Article ID 761745, 8 pages, 2014.
- [43] H. Goshayeshi, M. Safaei, and Y. Maghmoumi, "Numerical simulation of unsteady turbulent and laminar mixed convection in rectangular enclosure with hot upper moving wall by finite volume method," in *Proceedings of the 6th International Chemical Engineering Congress and Exhibition (ICheC '09)*, Kish Island, Iran, 2009.
- [44] M. R. Safaei, S. R. Saleh, and M. Goodarzi, "Numerical studies of laminar natural convection in a square cavity with orthogonal grid mesh by finite volume method," *International Journal of Advanced Design and Manufacturing Technology*, vol. 1, no. 2, pp. 13–21, 2011.
- [45] M. Goodarzi, M. R. Safaei, A. Karimipour et al., "Comparison of the finite volume and lattice Boltzmann methods for solving natural convection heat transfer problems inside cavities and enclosures," *Abstract and Applied Analysis*, vol. 2014, Article ID 762184, 15 pages, 2014.
- [46] M. R. Safaei and H. R. Goshayeshi, "Numerical simulation of laminar and turbulent mixed convection in rectangular enclosure with hot upper moving wall," *International Journal of Advanced Design and Manufacturing Technology*, vol. 3, no. 2, pp. 49–57, 2011.

- [47] M. R. Safaei, M. Goodarzi, and M. Mohammadi, "Numerical modeling of turbulence mixed convection heat transfer in air filled enclosures by finite volume method," *The International Journal of Multiphysics*, vol. 5, no. 4, pp. 307-324, 2011.

## Research Article

# Modeling Validation and Control Analysis for Controlled Temperature and Humidity of Air Conditioning System

Jing-Nang Lee,<sup>1</sup> Tsung-Min Lin,<sup>1</sup> and Chien-Chih Chen<sup>2</sup>

<sup>1</sup> Department of Refrigeration, Air-Conditioning and Energy Engineering, National Chin-Yi University of Technology, Taichung 411, Taiwan

<sup>2</sup> Graduate Institute of Mechanical and Electrical Engineering, National Taipei University of Technology, Taipei 106, Taiwan

Correspondence should be addressed to Chien-Chih Chen; [t8669030@ntut.edu.tw](mailto:t8669030@ntut.edu.tw)

Received 6 July 2014; Revised 4 August 2014; Accepted 7 August 2014; Published 26 August 2014

Academic Editor: Marjan Goodarzi

Copyright © 2014 Jing-Nang Lee et al. This is an open access article distributed under the Creative Commons Attribution License, which permits unrestricted use, distribution, and reproduction in any medium, provided the original work is properly cited.

This study constructs an energy based model of thermal system for controlled temperature and humidity air conditioning system, and introduces the influence of the mass flow rate, heater and humidifier for proposed control criteria to achieve the controlled temperature and humidity of air conditioning system. Then, the reliability of proposed thermal system model is established by both MATLAB dynamic simulation and the literature validation. Finally, the PID control strategy is applied for controlling the air mass flow rate, humidifying capacity, and heating, capacity. The simulation results show that the temperature and humidity are stable at 541 sec, the disturbance of temperature is only 0.14°C, 0006 kg<sub>w</sub>/kg<sub>da</sub> in steady-state error of humidity ratio, and the error rate is only 7.5%. The results prove that the proposed system is an effective controlled temperature and humidity of an air conditioning system.

## 1. Introduction

The air conditioning system can regulate indoor air quality to provide a more comfortable and safer environment. It is also important in the high-tech industry and medical industry. Liu et al. [1] use computational fluid dynamics (CFD) to create a thermally comfortable and healthy environment by air distributed information from numerical simulation. Safaei and Goshayshi [2] finite volume method, which is based on the difference of temperature and momentum, has effect on mechanical ventilation or pressure different and finally results in indoor and outdoor flow. Safaei et al. [3] investigate the energy transferring through two different heated side walls, especially transferring in rooms and buildings. However, as the controller of air-conditioning system has long time constant, multivariable, and high control complexity by interaction between parameters, it is thus difficult to obtain accurate mathematical model. Due to the high energy consuming, the research on high efficiency energy-saving air conditioning system has become a topical subject. An effective control law is very important for developing high energy efficiency air-conditioning system. The discussion

on the influence of air-conditioned zone energy input and output on indoor temperature and humidity, as well as the analysis of the dynamic characteristics of air conditioning system, is important in analyzing air conditioning system and designing control law. Therefore, it is necessary to develop an approximate thermodynamic model and validate the feasibility of model at the design stage of air conditioning system. Many recent studies have used the theoretical or experimental method to explore the dynamic model of air conditioning system as the basis of air conditioning system control. Tsao et al. [4] developed high efficiency make-up air units (MAUs) for technology factories in subtropical zone by modeling thermodynamic system and proposed eight schemes for analysis, among which was the dry coil cooling-(DCC-) based energy-saving scheme. However, the thermal model was built for air-conditioning equipment only, and the effect of energy on the state of air-conditioning space was not discussed. Soyguder et al. [5] built a thermal model of air conditioning system and used PID expert fuzzy control to adjust the air-conditioned zone temperature change. However, that system lacked humidity control for air-conditioned

zone. Tashtoush et al. [6] developed a thermal model of air conditioning system and air-conditioned zone and used PID to control the outflow air temperature and humidity for constant temperature and humidity control. However, only the outflow air temperature and humidity were controlled, while the operation of the equipment was not discussed. The outflow air temperature and humidity matching problem of the chilled water was not considered. Rehrh and Horn [7] proposed a simple thermodynamic model of air-conditioning equipment and combined it with feedback method for predictive control of air conditioning system. However, in terms of humidifier, the control mode was designed according to the characteristic curve of valve and humidifying capacity, and the test room was built instead of thermal model of air-conditioned zone for control. Platt et al. [8] built a model of air conditioning system and used genetic algorithm to optimize air conditioning control. However, only the temperature change of air-conditioned zone was controlled and the thermal model of air-conditioning equipment was not built, and the genetic algorithm was used as control base. Yao et al. [9] predicted the variance in chilled water by building the thermal model of chilled water coil and validated it by simulation. However, they did not apply the control law to the air-conditioned zone. Soyguder and Alli [10] used the air conditioning system thermal model and applied input-output data to PID ANFIS to control the fan speed. Barbosa and Mendes [11] built the thermal model of various equipment types of central air conditioning system and used weather data to simulate the on-off control of chiller. Kasahara et al. [12] modeled the air-conditioned zone and controlled temperature and humidity air conditioning system and used the thermal model and PI control to change the air output for constant temperature and humidity. Riederer et al. [13] built the thermal model of room system but did not regard the room as uniformly mixed constant volume. The air temperature change was deduced from the positions of sensors, and it was validated by experimental simulation. Kang et al. [14] proposed the HVAC model which introduces  $\text{CO}_2$  concentration to consider the comfort of room, and linear-quadratic regulator (LQR) is applied for optimizing and stabilizing the system. Amos-Abanyie et al. [15] investigated the thermal mass effect, window size, and night ventilation on peak indoor air temperature (PIAT) via E plus (E+) simulation. Homod [16] analyzed the advantage and disadvantage from types of HVAC model.

Therefore, in order to implement constant temperature and humidity control, the controlled temperature and humidity air conditioning system was used in this study. The air feeder, cooling coil heater, and humidifier constituted the air-conditioned zone at constant temperature and humidity. The thermal model of controlled temperature and humidity air conditioning system and air-conditioning equipment was built to discuss the influence of various types of equipment in the air conditioning cabinet on the temperature and humidity of air-conditioned zone. Finally, considering the matched cases, the PID control law was used to control the air mass flow rate ( $\dot{m}_a$ ), heater input percentage ( $\alpha$ ), and humidifier input percentage ( $\gamma$ ). This study investigates the controlling based on thermal and humidity conditions only

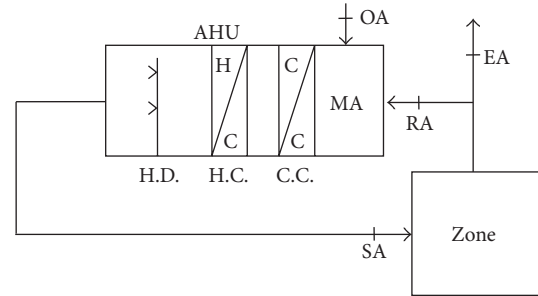


FIGURE 1: Controlled temperature and humidity of air conditioning system thermal model diagram.

without considering the energy transferring such as CFD, thus to discuss the stabilization time, overshoot and stability of controlled temperature, and humidity air conditioning system under PID control.

## 2. Modelling

**2.1. Description.** The main function of controlled temperature and humidity air conditioning system is to make the air-conditioned zone at constant temperature and humidity by applying different control strategies, so as to meet different industrial requirements, such as chemical laboratory, measuring and testing laboratory, process of high-tech industry, and electronic machine room. Figure 1 shows a typical controlled temperature and humidity air conditioning system.

First the difference between the practical status and target value is obtained by detection of indoor air state. Then the flow of return air (RA) is controlled by exhaust air (EA) and the outdoor air (OA) is introduced to generate mixing air (MA) in air-handling unit. The mixing air is processed by cooling and dehumidifying by cooling coil (C.C.), heating by heating coil (H.C.), and humidifying by humidifier (H.D.) to mix the desired state for air-conditioned zone gradually.

As shown in Figure 2, the algorithm first compares the difference between given  $T_s, \omega_s$  and room  $T_r, \omega_r$ , respectively, and delivery to PID controller. The control parameters  $m_a, \alpha$ , and  $\gamma$  of C.C., H.C., and H.D. are changed and begin to affect the room temperature and humidity. The controlled  $T_s, \omega_s$  are compared again with room  $T_r, \omega_r$  and begin the next loop.

**2.2. Mathematical Model of Controlled Temperature and Humidity of Air Conditioning System.** Figure 1 shows that, under the control of chilled water coil, heater, and humidifier of the controlled temperature and humidity air conditioning system, the air-conditioned zone is provided with appropriate energy to keep its temperature and humidity corresponding to the set conditions. The modeling of the system of the exhaust air, mixing air, chilled water coil, heater, and humidifier components is discussed. The design of comprehensive mathematical model of a controlled temperature and humidity air conditioning system is unpractical and unreasonable due to the complexity from its multivariable. Therefore the mathematical model will be simplified by the following assumptions.

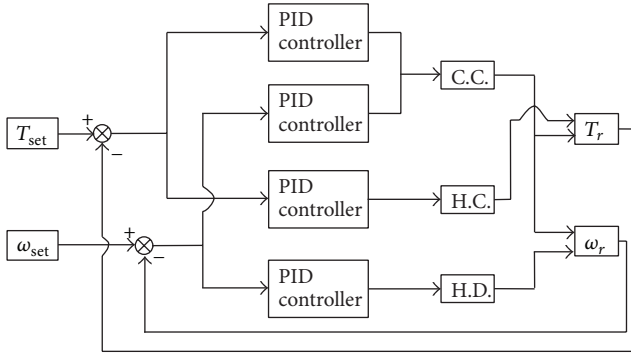


FIGURE 2: Overall block diagram for controlling the proposed air conditioning system.

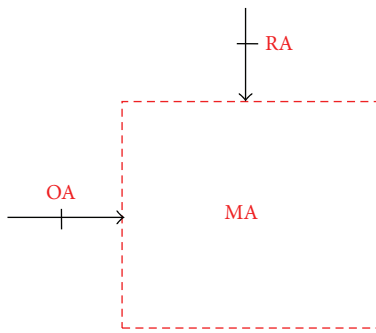


FIGURE 3: Schematic controlled volume of mixing process.

- (1) The specific heat and density of air are constants.
- (2) There is no air leakage in the process.
- (3) The boundary is insulated.
- (4) The air is regarded as the ideal gas.

**2.2.1. Exhaust Air and Mixing Air Model.** Generally, introduction of the outside air conditioning will raise cooling load on the air-conditioning zone. However, an appropriate amount of outside air can dilute the hazardous material in the air-conditioned zone, thus providing necessary fresh air for breathing, removing pollutant and controlling the temperature and humidity of work site, and upgrading the indoor air quality. The exhaust air damper is linked to outside air damper and controls the air discharge and outside air volume. Figure 3 shows the mixing process of indoor return air and outside air in the air mixing zone of the air conditioning cabinet, the outside air and return air volumes are adjusted by controlling the outside air damper opening, and the air is mixed in the mixing zone of air conditioning cabinet.

If the mixing process is a steady flow process, the energy conservation for the mixing process is expressed as

$$(1 - \beta) \times \dot{m}_a c_{pa} T_{RA} + \beta \times \dot{m}_a c_{pa} T_{OA} = \dot{m}_a c_{pa} T_{MA} \quad (1)$$

$$\beta \times \dot{m}_a c_{pa} (T_{OA} - T_{RA}) = \dot{m}_a c_{pa} (T_{MA} - T_{RA})$$

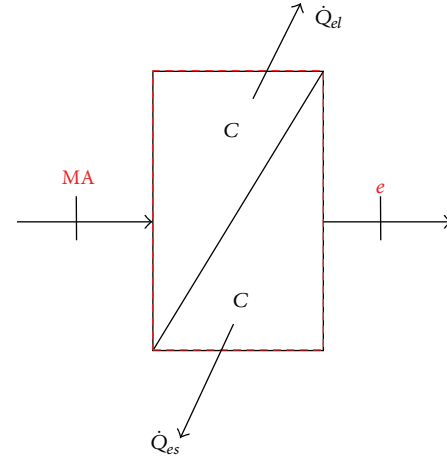


FIGURE 4: Schematic controlled volume of cooling coil model.

and the balance of the mass of water is expressed as

$$(1 - \beta) \times \dot{m}_a \omega_{RA} + \beta \times \dot{m}_a \omega_{OA} = \dot{m}_a \omega_{MA} \quad (2)$$

$$\beta \times \dot{m}_a (\omega_{OA} - \omega_{RA}) = \dot{m}_a (\omega_{MA} - \omega_{RA})$$

**2.2.2. Cooling Coil Model.** The energy in the air is transferred into the chilled water cycle, and the chilled water cycle delivers the energy to the evaporator. The evaporation of refrigerant in the evaporator takes the energy away, reducing the zone temperature and humidity. According to the air conditioning system, the chilled water temperature is generally 7~12°C. When the return air passes through the chilled water coil, if the chilled water temperature is lower than the return air dew-point temperature, the vapor in humid air is condensed for dehumidification. The mixed air enters the chilled water coil, taking the sensible heat ( $\dot{Q}_{es}$ ) and latent heat ( $\dot{Q}_{ls}$ ) of air away. The cooled and dehumidified air is fed to the heater. If the heat exchange rate is 100% when the air passes through the chilled water coil, it is steady flow process, and the moisture condensed on the coil is removed completely and immediately by gravity as shown in Figure 4.

Disregarding the variance in kinetic energy and potential energy, the energy conservation of chilled water is expressed as

$$-(\dot{Q}_{es} + \dot{Q}_{el}) = \dot{m}_a (h_e - h_{MA}) \quad (3)$$

The humid air energy variation of (3) is divided into the energy of dry air and water vapor, expressed as

$$-(\dot{Q}_{es} + \dot{Q}_{el}) = \dot{m}_a c_{pa} (T_e - T_m) + \dot{m}_a h_{fg} (\omega_e - \omega_m) \quad (4)$$

The sensible heat of air ( $\dot{Q}_{es}$ ) only influences the air temperature and the latent heat of air ( $\dot{Q}_{ls}$ ) only influences the air vapor, so (4) can be expressed as (5) and (6), respectively, as follows:

$$-\dot{Q}_{es} = \dot{m}_a c_{pa} (T_e - T_{MA}) \quad (5)$$

$$-\dot{Q}_{el} = \dot{m}_a h_{fg} (\omega_e - \omega_{MA}) \quad (6)$$

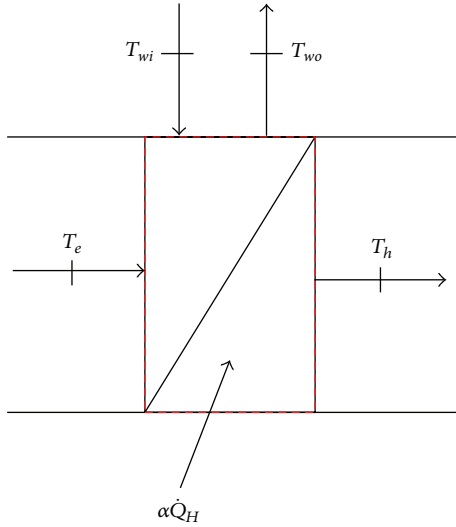


FIGURE 5: Schematic controlled volume of heating coil model.

Equation (6) can be reduced to vapor mass conservation equation, expressed as

$$\frac{Q_{el}}{h_{fg}} = \dot{m}_a (\omega_e - \omega_{MA}). \quad (7)$$

**2.2.3. Heating Coil Model.** It is switched on when the room temperature is lower than the set point. By heating the temperature of supplied air with heater, the heat energy is transferred to the air-conditioned zone, and let the temperature reach the set point. The heater is divided into hot-water heating, electric heater, and steam heating. In this study, the hot water coil is used as the heater of controlled temperature and humidity air conditioning system. The air through chilled water passes through the heating coil to take the heat into the air, and the heated air is fed to the humidifier as shown in Figure 5. The heating capacity of heater is pure sensible heat change, the heater output power ( $\alpha\dot{Q}_H$ ) heats the air, and the humidity ratio of air-conditioned zone will not be influenced.

If the heating process is steady flow process, the energy conservation relationship of heater as shown in Figure 5 is expressed as

$$\alpha\dot{Q}_H = \dot{m}_a c_{pa} (T_h - T_e) = \dot{m}_w c_{pw} (T_{wi} - T_{wo}). \quad (8)$$

**2.2.4. Humidifier Model.** The humidifier output power ( $\gamma\dot{Q}_L$ ) converts electric energy into latent heat, the moisture is added in the system by steam humidification so that the humidity of the air supply changes, and the system processed air is fed into the air-conditioned zone. The humidifier humidification is pure latent heat modification; therefore, only humidity changes, and the temperature of air-conditioned zone is not

influenced. If the humidifier is steady flow process, it can be described by a simple vapor mass conservation equation as

$$\frac{\gamma\dot{Q}_L}{h_{fg}} = \dot{m}_a (\omega_s - \omega_h). \quad (9)$$

**2.2.5. Integration to a Zone Hygrothermal Model.** In order to make the air-conditioned zone reach the set temperature and humidity, the controlled temperature and humidity air conditioning system must be used. The controlled temperature and humidity air conditioning system consists of chilled water coil, heater, and humidifier. The mathematical model of air-conditioned zone is simplified by the following assumptions.

- (1) The air-conditioned zone is an open and unsteady flow system in constant volume.
- (2) The air temperature and humidity in the air-conditioned zone are distributed uniformly.
- (3) The specific heat and density of air are constants.
- (4) There is no air leakage in the process.
- (5) The wall surface of air-conditioned zone is insulated.
- (6) The air is regarded as ideal gas.

According to thermodynamic energy conservation equation, the thermal model [17] can be expressed as

$$\begin{aligned} \dot{Q}_{C.V.} = & \dot{W}_{C.V.} + \sum_{out} \left[ \dot{m} \left( h + \frac{V^2}{2} + gz \right) \right] \\ & - \sum_{in} \left[ \dot{m} \left( h + \frac{V^2}{2} + gz \right) \right] + \frac{dE_{C.V.}}{dt}. \end{aligned} \quad (10)$$

If the kinetic energy and potential energy variations in the process are ignored and the system has not applied work, (10) is reduced to

$$\dot{Q}_{C.V.} = \sum_{out} \dot{m}h - \sum_{in} \dot{m}h + \frac{dE_{C.V.}}{dt}. \quad (11)$$

Figure 6 shows that the air-conditioned zone state is significantly influenced by the persons, office equipment in operation, and various machine tools in the space and the heat transfer to the space is shown in Figure 2 so that the air state in the space changes. The temperature and humidity increase continuously, and the state keeps deviating from comfort zone. Different air conditioning loads influencing indoor state can be reduced to sensible heat load ( $\dot{Q}_{rs}$ ) and latent heat load ( $\dot{Q}_{rl}$ ). The energy conservation equation (12) for air-conditioned zone can be deduced from (11):

$$m_{C.V.} c_v \frac{dT_{C.V.}}{dt} = \dot{m}_a c_p (T_{OA} - T_{RA}) + \dot{Q}_{rs}. \quad (12)$$

According to the law of conservation of mass of vapor, the air-conditioned zone humidity change can be expressed as

$$m_{C.V.} \times \frac{d\omega_{C.V.}}{dt} = \dot{m}_a (\omega_{SA} - \omega_{RA}) \times \frac{\dot{Q}_{rl}}{h_{fg}}, \quad (13)$$

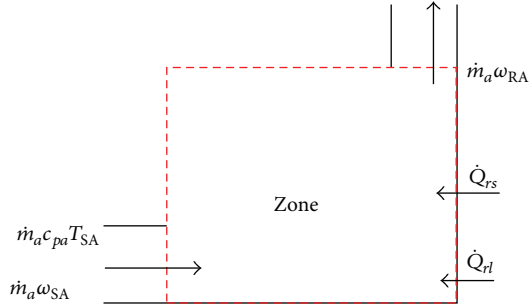


FIGURE 6: Schematic diagram of thermal model for air-conditioned zone.

where  $\dot{m}_a c_p (T_{SA} - T_{RA})$  and  $\dot{m}_a (\omega_{SA} - \omega_{RA})$  are the energy and vapor mass, respectively, taken in or out of the system by various equipment types in the air conditioning cabinet, so (2) are combined with the thermal model of various equipment types of the air conditioning system in Section 2.2. The energy conservation and vapor mass conservation equations represent the indoor temperature and humidity variations, respectively, expressed as

$$m c_v \frac{dT_{C.V.}}{dt} = \dot{m}_a c_{pa} (T_h - T_e) + \beta \times \dot{m}_a c_p (T_o - T_r) - \dot{m}_a c_p (T_m - T_e) + \dot{Q}_{rs} \quad (14)$$

$$m \frac{d\omega_{C.V.}}{dt} = \dot{m}_a (\omega_s - \omega_h) + \beta \dot{m}_a (\omega_o - \omega_r) - \dot{m}_a (\omega_m - \omega_e) + \frac{\dot{Q}_{rl}}{h_{fg}} \quad (15)$$

### 3. Results and Discussion

In order to validate the controlled temperature and humidity air conditioning system model deduced in Section 2, MATLAB is used to create the dynamic simulation program of the system, and set the simulation condition working procedure of [6]. The changes in the temperature and humidity ratios of air-conditioned zone are compared with the literature, so as to validate the accuracy of the thermal model and the dynamic simulation program. When the dynamic simulation program is determined, a well-known control law is still required to direct the action of controlled temperature and humidity air conditioning system, so that the system function can be perfected. Therefore, the PID control is used and the cooling and dehumidification capability matching of chilled water is considered. Ziegler-Nichols rule is applied to obtain PID control parameters, so as to analyze the effectiveness of PID control of controlled temperature and humidity air conditioning system.

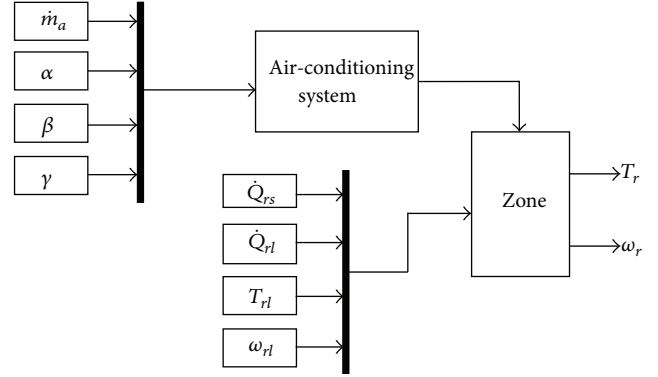


FIGURE 7: Block diagram of controlled temperature and humidity of an air conditioning system.

TABLE 1: Parameters of air-conditioned zone in [6].

Initial state of the zone	32° C DB	0.025 kg <sub>w</sub> /kg <sub>da</sub>
Zone volume (m <sup>3</sup> )	36	
Zone cooling load (kW)	Sensible heat 1.3	Latent heat 0
Supply air temperature (°C)	13	

**3.1. Modeling Validation.** The dynamic simulation of the proposed model, based on the hypothesis in chapter 2, is built and processed by Matrix Laboratory (MATLAB) and is shown in Figure 7. The program simulates eight input parameters, which are zone sensible heat ( $\dot{Q}_{rs}$ ), zone latent heat ( $\dot{Q}_{rl}$ ), initial temperature of air-conditioned zone ( $T_{rl}$ ), zone initial humidity ratio ( $\omega_{rl}$ ), air mass flow rate ( $\dot{m}_a$ ), heater capacity ( $\alpha$ ), outside air ( $\beta$ ), and humidifier capacity ( $\gamma$ ), respectively. When the above parameters are imported into the simulation, the program calculates the energy variation in the space resulting from various equipment types.

This study developed an open loop control test and set different air mass flow rates. The effectiveness of dynamic model of the system is validated by comparing the results of this study with the simulation results of the literature. This test neglected the external wall and heat transfer. The set conditions are shown in Table 1.

The simulation results are shown in Figures 8 and 9. If there is only zone sensible heat, the stable temperature decreases as the air mass flow rate increases, and the humidity ratio converges to 0.00763 kg<sub>w</sub>/kg<sub>da</sub>. According to (14), when there is sensible heat load, the difference between zone temperature and chilled water temperature decreases with the indoor temperature. The temperature is stabilized until the heat taken away by the chilled water equals the sensible heat load. Therefore, with a larger air mass flow rate, the stable temperature is lower. When the system lacks air mass flow rate, the sensible heat load cannot be taken away adequately, so that the cooling is failed, and the return air temperature difference increases continuously. However, as the temperature difference changes, the heat load taken away by the chilled water increases and it reaches balance with sensible heat load at last. In terms of humidity ratio

TABLE 2: Steady state of zone versus air mass flow rate.

Airflow (kg/s)	Temperature ( $^{\circ}\text{C}$ )			Humidity ratio ( $\text{kg}_w/\text{kg}_{da}$ )		
	Reference [3]	Simulation	Error	Reference [3]	Simulation	Error
0.05				0.00781	0.00763	2.3%
0.1	24.95	25.95	-4%	0.00782	0.00763	2.4%
0.2	20.28	19.47	3.9%	0.00782	0.00763	2.4%
0.4	17.01	16.23	4.5%	0.00775	0.00763	1.5%
0.8	15.16	14.62	3.5%			

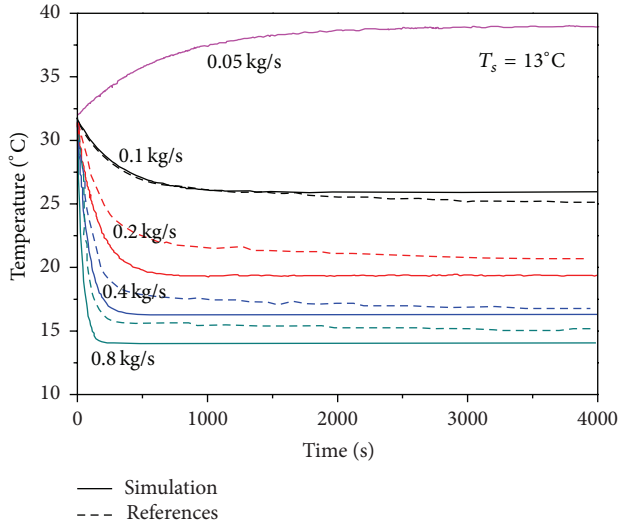


FIGURE 8: Zone temperature versus time for air mass flow rate compared with [6].

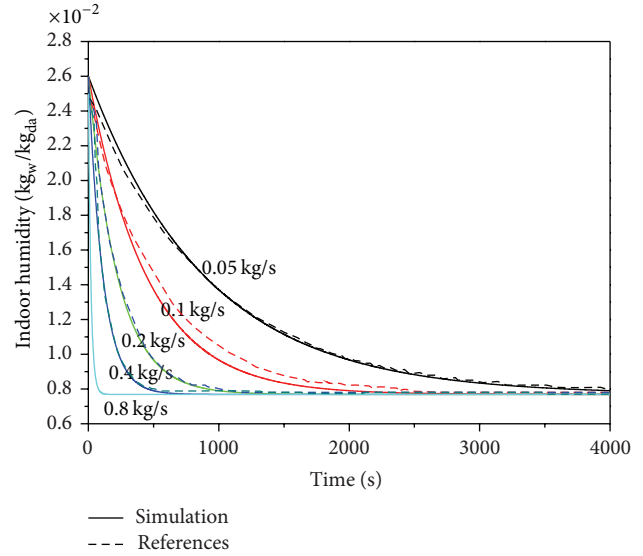


FIGURE 9: Zone humidity ratio versus time for air mass flow rate compared with [6].

without latent heat, according to (5), regardless of  $\dot{m}_a$ , the outflow air humidity ratio is eventually converged. Relevant parameters are shown in Table 2. As seen, when  $\dot{m}_a$  is large, the stabilization time is short. The simulation results are consistent with the trend in the literature. This study did not consider the wall heat transfer, and the simulation results were compared with the literature. At 4000 sec when stabilization was most approximately reached, the maximum error was  $1^{\circ}\text{C}$ , and the error rate was 4%. The humidity ratio converged to  $0.763 \text{ kg}_w/\text{kg}_{da}$  with maximum error was 2.4%.

**3.2. Simulation Results.** PID control is a closed loop control system, commonly used in industry. The PID algorithm can provide a considerable control effect with good adjustment. Sensors are applied for detecting the present state of air-conditioned zone and returning them back to comparator. The state of air-conditioned zone reaches the set state through proportional control, integral control, and differential control. As it is simple and understandable and its adjustment does not need precise system model, it is widely used in various domains. The PID control input-output relationship is expressed as the following equation:

$$G_o(s) = \frac{U(s)}{E(s)} = K_p + \frac{S}{T_i} + T_d S, \quad (16)$$

where  $K_p$ ,  $T_i$ , and  $T_d$  are the proportionality, integral, and differential coefficients of PID controller. The proportional control regulates and controls the system according to the difference between input and output signals. However, the steady-state error cannot be removed by only proportional control. In order to eliminate steady-state error, the integral control is adopted. The integral term takes the integral of time and the integral term increases with time, so that the control output increases until the steady-state error is eliminated. In the process of regulation, the system may have oscillation even run out of control due to inertial or lag component, and the integral term magnifies the oscillation on the contrary. Therefore, the differential term is used to predict the variation trend to improve the interference effect. However, the three control parameters influence each other. Hence, how to obtain control parameters becomes an important but difficult problem in PID control.

The PID controller set-up parameters in this paper are designed according to Ziegler-Nichols empirical rule, which is regarded as a good parameter optimization in PID control [6]. The parameters are adjusted continuously to make system oscillation, so as to know the system response. The control parameter settings are derived from empirical equation, as shown in Table 3. In this paper, considering the matching of

TABLE 3: Parameters of PID controllers.

Control parameters	Cooling coil		Heater	Humidifier
	Airflow ( $m_a$ )		Percentage of output power ( $\alpha$ )	Percentage of output power ( $\gamma$ )
Feedback parameters	Zone temperature	Zone humidity ratio	Zone temperature	Zone humidity ratio
$K_p$	14.7	52.1	34.7	28.2
$K_i$	1	1	1	1
$K_d$	0.25	0.25	0.25	0.25

cooling and dehumidification effects of chilled water coil, the air mass flow rate ( $m_a$ ) is used as control parameter, and the heater and humidifier control is added. With the assistance of heater output power percentage ( $\alpha$ ) and humidifier output power percentage ( $\gamma$ ), the loss of chilled water due to excessive cooling or dehumidification is compensated.

According to the system parameters of desired controlled temperature and humidity of air conditioning system, a PID controlled real time of the proposed air conditioning system can be built by Simulink as shown in Figure 10. Simulation begins with given initial conditions, and the controller adjusts P, I, and D, respectively, to control room temperature and humidity.

As shown in Table 3, the chilled water is equipped with two PID controllers, which feedback indoor temperature and humidity ratio data. Two air mass flow rate data are exported under control. As the dehumidification and cooling only depend on the chilled water coil, considering the system matching problem, this paper uses large value as the actual output. Therefore, if sensible heat or latent heat is removed excessively, the heater and humidifier are used for compensation.

This paper observes the convergence and stability of PID control based on constant temperature and humidity system thermal model in simulated summer environment. Moreover, it validates the feasibility of PID control in controlled temperature and humidity air conditioning system. The set conditions are described below.

- (1)  $T_{set} = 22^\circ\text{C}$ ;  $\omega_{set} = 0.008 \text{ kg}_w/\text{kg}_{da}$ .
- (2)  $T_{rl} = 32^\circ\text{C}$ ;  $\omega_{rl} = 0.025 \text{ kg}_w/\text{kg}_{da}$ .
- (3) Zone volume is  $36 \text{ m}^3$ .
- (4) Sensible heat load is  $1.3 \text{ kW}$ .
- (5) Air mass flow rate is  $0\sim 0.3 \text{ kg/s}$ .
- (6) Heater is  $0\sim 0.6 \text{ kW}$ .
- (7) Humidifier is  $0\sim 1 \text{ kW}$ .

At the beginning, the overheat room temperature is detected by PID controller of chilled water coil, triggering the increase of mass flow rate to cool down the room temperature till reaching  $17.81^\circ\text{C}$ . The overcool temperature stimulates the PID controller of heater and the heater is working till setting temperature. The crossfunction of these two PID controllers results in a sharp control curve as shown in Figure 11.

In humidifier, due to the fact the humidity ratio controlling needs only adjusting the chilled water coil, only one PID

controller, which belong to chilled water coil, is working and results in a smooth curve as shown in Figure 12.

According to the indoor temperature and humidity ratio variations in Figures 6 and 7, under the PID control, the humidity ratio can be controlled well. However, in terms of temperature stability, the maximum disturbance is  $0.14^\circ\text{C}$ . Because there are two PID controllers, when the temperature and humidity approach the set values, and the output air between the two controllers, resulting in oscillation. In addition, as the air-conditioned zone cooling response speed is higher than dehumidification, when the temperature is reached, the chilled water still needs to continue dehumidification, so that the indoor temperature decreases to  $17.81^\circ\text{C}$  before it rises to the set value. The maximum overshoot of temperature is  $4.19^\circ\text{C}$ . The temperature and humidity are stable at 541 sec, but the steady state of humidity ratio is  $0.0074 \text{ kg}_w/\text{kg}_{da}$ , the steady-state error is  $0.0006 \text{ kg}_w/\text{kg}_{da}$ , and the error rate is 7.5%.

The simulation data are displayed in the psychrometric chart, as shown in Figure 13. The air state changes in the air-conditioned zone in the PID control mode. First, it is high temperature and high humidity state and only the chilled water is used for cooling and dehumidification. Therefore, the air state almost develops towards the outflow air temperature and humidity point straightly. Soon after the temperature is lower than the set point, the heater is started up to lower the temperature to the set point. The matching of various equipment types stabilizes the air state inside the air-conditioned zone at the set point.

#### 4. Conclusion

This study developed a thermal model for controlled temperature and humidity air conditioning system, including air-conditioned zone, air mixing stage, chilled water coil, heater, and humidifier. Based on the thermal model, MATLAB was used to simulate open loop control system, and it is compared with references to validate the feasibility of the system. As the wall heat transfer was disregarded, the maximum error between room temperature simulation and literature was  $1^\circ\text{C}$ , and the maximum error rate between humidity ratio simulation and the literature was only 2.4%. Finally, the PID controller was used for control. When the system matching was considered, the Ziegler-Nichols empirical rule was applied to control the air mass flow rate, humidifier output power, and heater output power. The results showed that the PID control could reach stabilization at 541 sec at high temperature and high humidity. The maximum overshoot

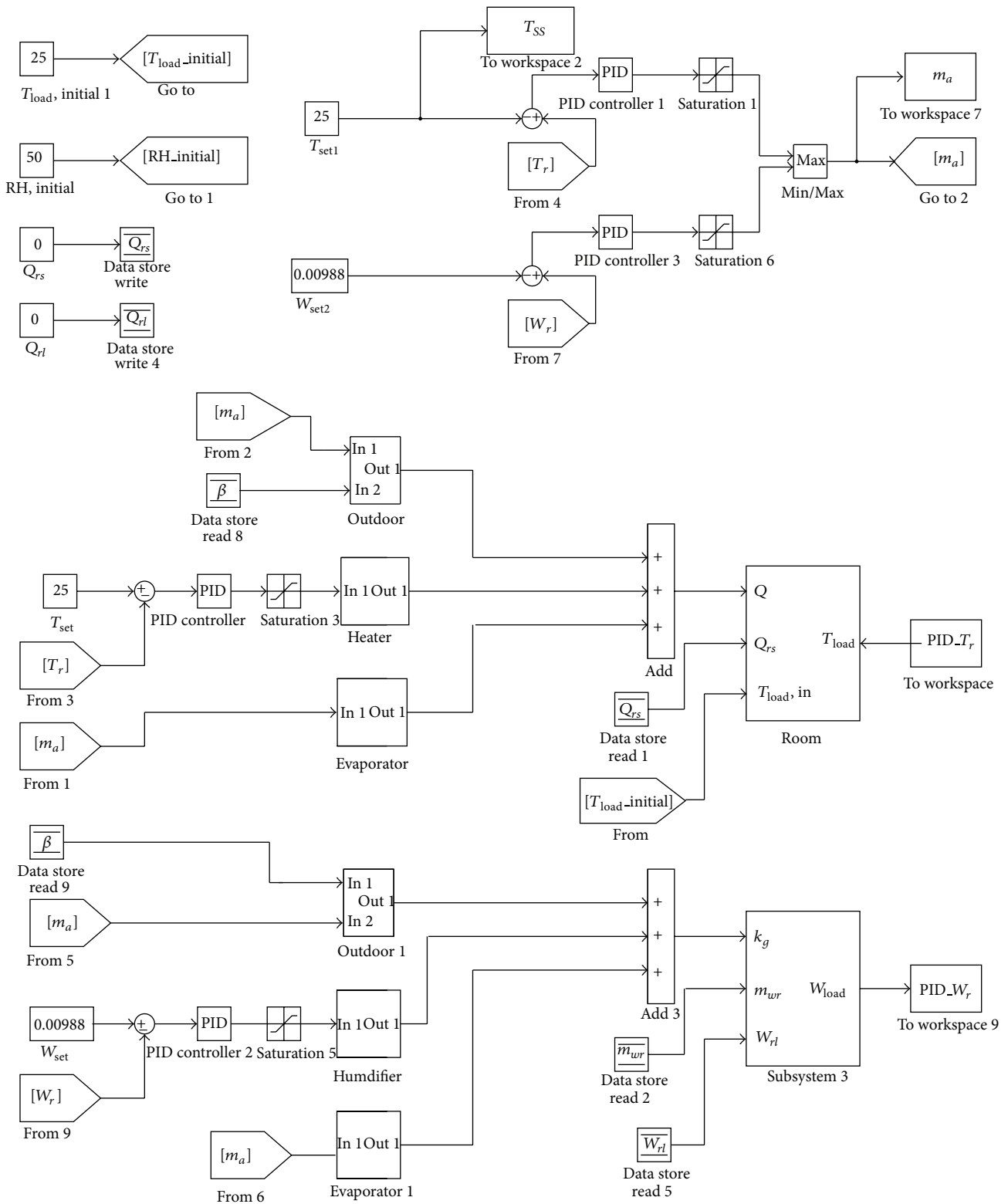


FIGURE 10: Schematic block diagram of PID control for the proposed system.

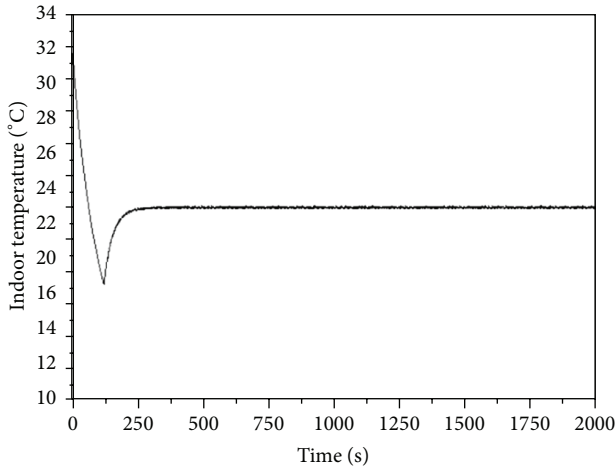


FIGURE 11: Zone temperature versus time for PID controller.

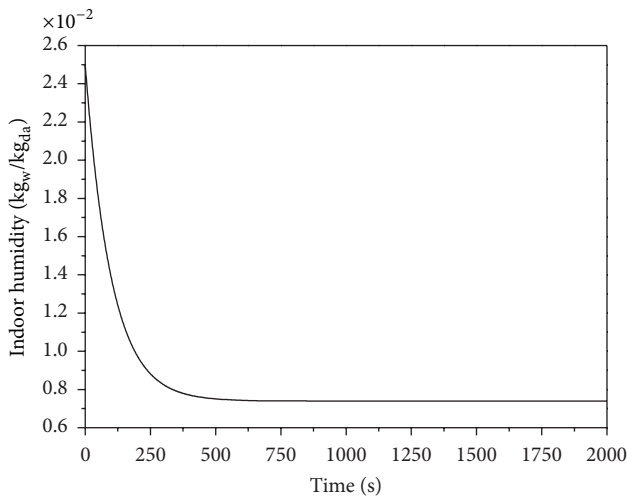


FIGURE 12: Zone humidity versus time for PID controller.

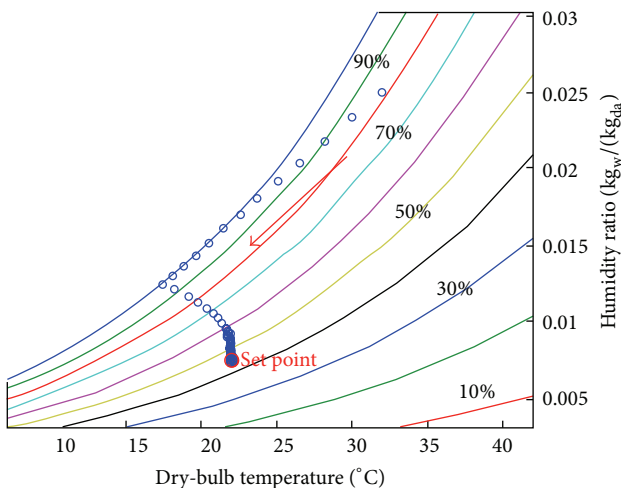


FIGURE 13: Zone air state change psychrometric chart.

was 4.19°C, the humidity ratio error rate was only 7.5%, and the maximum temperature disturbance was 0.14°C. The goal for constant temperature and humidity could be attained effectively.

**Nomenclature**

- $\dot{m}_a$ : Mass flow rate of the air stream (kg/s)
- $c_p$ : Specific heat (kJ/kg-°C)
- $T$ : Temperature (°C)
- $\omega$ : Humidity ratio (kg<sub>w</sub>/kg<sub>da</sub>)
- $h$ : Enthalpy (kJ/kg)
- $h_e$ : Enthalpy of air through chilled water (kJ/kg)
- $h_{fg}$ : Latent heat of vaporization of vapor (kJ/kg)
- $\dot{Q}_H$ : Maximum input power of heater (kJ)
- $\dot{Q}_L$ : Maximum output power of humidifier (kJ).

*Subscripts*

- $a$ : Air
- $da$ : Dry air
- $e$ : Air through chilled water
- $h$ : Heater
- $l$ : Latent heat
- $s$ : Sensible heat
- $w$ : Water
- MA: Mixing air
- OA: Outside air
- RA: Return air
- WO: Return water
- Wi: Supply water.

*Greek Letters*

- $\alpha$ : Heater input power percentage
- $\beta$ : Outside air damper opening
- $\gamma$ : Humidifier output power percentage.

**Conflict of Interests**

The authors declare that there is no conflict of interests regarding the publication of this paper.

**Acknowledgments**

This research is supported by the Department of Refrigeration, Air Conditioning and Energy Engineering, National Chin-Ti University of Technology, as well as National Science Foundation of Taiwan and under Grant no. NSC100-2622-E-167-016-CC3.

**References**

- [1] W. Liu, S. Mazumdar, Z. Zhang et al., "State-of-the-art methods for studying air distributions in commercial airliner cabins," *Building and Environment*, vol. 47, no. 1, pp. 5-12, 2012.
- [2] M. R. Safaei and H. R. Goshayshi, "Investigation of turbulence mixed convection in air filled enclosures," *Journal of Chemical Engineering and Materials Science*, vol. 2, no. 6, pp. 87-95, 2011.

- [3] M. R. Safaei, M. Goodarzi, and M. Mohammadi, "Numerical modeling of turbulence mixed convection heat transfer in air filled enclosures by finite volume method," *International Journal of Multiphysics*, vol. 5, no. 4, pp. 307–324, 2011.
- [4] J. Tsao, S. Hu, T. Xu, and D. Y. L. Chan, "Capturing energy-saving opportunities in make-up air systems for cleanrooms of high-technology fabrication plant in subtropical climate," *Energy and Buildings*, vol. 42, no. 11, pp. 2005–2013, 2010.
- [5] S. Soyguder, M. Karakose, and H. Alli, "Design and simulation of self-tuning PID-type fuzzy adaptive control for an expert HVAC system," *Expert Systems with Applications*, vol. 36, no. 3, pp. 4566–4573, 2009.
- [6] B. Tashtoush, M. Molhim, and M. Al-Rousan, "Dynamic model of an HVAC system for control analysis," *Energy*, vol. 30, no. 10, pp. 1729–1745, 2005.
- [7] J. Rehrl and M. Horn, "Temperature control for HVAC systems based on exact linearization and model predictive control," in *Proceedings of the 20th IEEE International Conference on Control Applications (CCA '11)*, pp. 1119–1124, September 2011.
- [8] G. Platt, J. Li, R. Li, G. Poulton, G. James, and J. Wall, "Adaptive HVAC zone modeling for sustainable buildings," *Energy and Buildings*, vol. 42, no. 4, pp. 412–421, 2010.
- [9] Y. Yao, Z. Lian, and Z. Hou, "Thermal analysis of cooling coils based on a dynamic model," *Applied Thermal Engineering*, vol. 24, no. 7, pp. 1037–1050, 2004.
- [10] S. Soyguder and H. Alli, "Predicting of fan speed for energy saving in HVAC system based on adaptive network based fuzzy inference system," *Expert Systems with Applications*, vol. 36, no. 4, pp. 8631–8638, 2009.
- [11] R. M. Barbosa and N. Mendes, "Combined simulation of central HVAC systems with a whole-building hygrothermal model," *Energy and Buildings*, vol. 40, no. 3, pp. 276–288, 2008.
- [12] M. Kasahara, Y. Kuzuu, T. Matsuba, Y. Hashimoto, and K. S. Kamimura, "Physical model of an air conditioned space for control analysis," *ASHRAE Transactions*, vol. 106, part 2, pp. 307–317, 2000.
- [13] P. Riederer, D. Marchio, J. C. Visier, A. Husaunndee, and R. Lahrech, "Room thermal modelling adapted to the test of HVAC control systems," *Building and Environment*, vol. 37, no. 8-9, pp. 777–790, 2002.
- [14] C. S. Kang, J. I. Park, M. Park, and J. Baek, "Novel modeling and control strategies for a HVAC system including carbon dioxide control," *Energies*, vol. 7, pp. 3599–3617, 2014.
- [15] S. Amos-Abanyie, F. O. Akuffo, and V. Kutin-Sanwu, "Effects of thermal mass, window size, and night-time ventilation on peak indoor air temperature in the warm-humid climate of ghana," *The Scientific World Journal*, vol. 2013, Article ID 621095, 9 pages, 2013.
- [16] R. Z. Homod, "Review on the HVAC system modeling types and the shortcomings of their application," *Journal of Energy*, vol. 2013, Article ID 768632, 10 pages, 2013.
- [17] Y. A. Cengel and M. A. Boles, *Thermodynamics an Engineering Approach*, McGraw Hill, New York, NY, USA, 6th edition, 2006.